LIBRARY
Michigan State
University

This is to certify that the
dissertation entitled

A NOVEL POLE-CHANGING INDUCTION MOTOR DRIVE

presented by

JOHN WILLIAM KELLY

has been accepted towards fulfillment
of the requirements for the

__Doctoral__ degree in __Electrical Engineering__

_____
Major Professor's Signature

__17 Dec 07__

Date

MSU is an affirmative-action, equal-opportunity employer

PLACE IN RETURN BOX to remove this checkout from your record.
TO AVOID FINES return on or before date due.
MAY BE RECALLED with earlier due date if requested.

DATE DUE	DATE DUE	DATE DUE

A NOVEL CONTROL SCHEME FOR A POLE-CHANGING INDUCTION MOTOR DRIVE

By

John William Kelly

A DISSERTATION

Submitted to
Michigan State University
In partial fulfillment of the requirements
for the degree of

DOCTOR OF PHILOSOPHY

Department of Electrical Engineering

2007

ABSTRACT

A NOVEL CONTROL SCHEME FOR A POLE-CHANGING INDUCTION MOTOR DRIVE

By

John William Kelly

For applications, such as the propulsion of a hybrid vehicle, a novel pole-changing induction motor drive is proposed. A pole-changing control scheme which allows continuously operation and torque production over the drive's entire speed/torque range was developed. The scheme is based on the concept of the pole-changing machine being simultaneously operated as two independent motors. From the nine stator winding machine, the two possible configurations are, the 9-phase/4-pole and 3-phase/12-pole motors.

For 9-phase operation, a generalized scheme for n-phase Space Vector PWM was developed. For field oriented control, a unique coordinate transformation from a 9-phase symmetrical system to an orthogonal system was developed. The inverse transformation also was developed based on the constraints which minimized core and winding losses

To my parents, William and Patricia Kelly

ACKNOWLEDGMENTS

TABLE OF CONTENTS

LIST OF TABLES

LIST OF FIGURES

xi

CHAPTER 1

Introduction

1.1 Motivation and Objectives

This work is an extension of work conducted on the development of a toroidally wound, pole reconfigurable induction machine. Ford Motor Company designed this machine to be the starter/alternator for 42Volt passenger vehicles. The unique machine has nine separately wound, equally distributed stator windings each attached to a terminal of a 9-leg inverter. This system allows for grouping coils into two different arrangements resulting in a motor with two possible pole numbers. In addition, to being used for the starter/alternator application, this system can be utilized as an induction motor drive with extended capability.

For applications such as propulsion, extended speed/torque capabilities of the drive system are desirable. Increased starting torque allows for faster acceleration, while increase speed allows for higher cruising velocity. Typically, these enhanced capabilities are achieved with conventional electric motors with the addition of a mechanical transmission and or motor field weakening control. This is at the cost of overall efficiency due to increased weight and gear inefficiency. Likewise, field weakening decreases efficiency with an increase in winding losses.

The starter/alternator was designed for high starting torque and high speeds; however, it was not designed for continuous operation over its extended speed/torque range. Pole-changing was to occur once the windings had been de-energized. The objective of the work

1

presented here is to develop a pole-changing control scheme for the existing starter/alternator, resulting in a drive system that can operate continuously and supply torque over its entire speed/torque range.

1.2   Previous Work: Starter-Alternator Machine

A toroidally wound, pole-phase modulated induction machine was designed by Miller and Ostovic [16],[15] for vehicle alternator/starter applications. The integrated starter-generator design was in response to the proposed 42V ISO standard for passenger automobiles [5]. Mounted directly to the internal combustion motor, the toroidal design was intended to meet the strict space constraints of the engine compartment. The volume of a toroidally wound machine is smaller than an equivalently rated lap wound motor, due to the elimination of end turns.

However, there are two significant drawbacks to using the toroidal design: 1) poor stator winding thermal dissipation and, 2) flux leakage to the housing. Since the stator windings are wrapped around the stator, there is no direct, metal to metal, thermal path from the stator to the housing. Therefore, the stator was designed to have wide mounting tabs that not only secured the stator to the housing, but created equally spaced, low resistance thermal paths around the motor. In addition, the space between the stator windings and housing was filled with a special thermal conductive resin from Dow Corning. Finally, the housing contained a water jacket. At first, the housing was made of steel. However, the steel was replaced by aluminium, significantly reducing the flux leakage to the housing, figure 1.1. The machine was designed to operate as a 3-phase/4-pole alternator and a 3-phase/12-pole starter. Depending on the application, the stator coils were grouped accordingly by a 9-leg inverter. Changing the number of poles of a machine by changing the number of applied phases is called pole-phase modulation (PPM) [16]. In chapter 3, the machine design is presented in detail.

Extensive work was conducted by Stefanovic [23]: 1) implementation of PPM 2) the study of transient effects occurring during motor-generator transition, 3) evaluation of stability of a PPM system in regards to sub-harmonics resulting from phase imbalances, and 4) analysis of
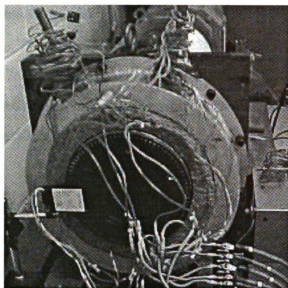
Figure 1.1: Toroidally wound Induction Machine.

offset and sensor error.

1.3 Pole-changing Machines

There are two predominant techniques for changing the number of poles for an induction machine. The first technique requires a specially-designed reconfigurable stator winding. The number of poles is changed by rearranging the coils of the winding. The second technique also requires an unconventional machine, one with two stator windings. One winding is used for low speed operation, while the other winding is used for high speed operation.

1.3.1 Multi-Stator Windings

For multi-stator induction machines, the simplest mode of operation is energizing one winding set at a time. The windings are spaced to achieve the desired pole number. However, Osama and Lipo showed that increased efficiency and copper utilization can be achieved by energizing both winding sets simultaneously, [18]. This dual stator winding induction machine can operate either as a 2-pole or 4-pole machine. The coils of the windings are stacked in the stator slots, forming a double layer winding distribution. Each of the two 3-phase windings is

3

controlled by two separate three-phase inverters. For 4-pole operation, the phase sequence for both inverters is i_a, i_b, i_c. The number of poles is decreased by half, by phase shifting the currents in one inverter. While the outputs of one inverter remain the same, i_a, i_b, i_c, the second inverter output is changed to $-i_a, -i_c, -i_b$. For starting and low speed operation the machine is configured for 4-poles. Once the break-down torque is reached, the machine is reconfigured for 2-pole operation.

1.3.2 Reconfigurable Stator Winding

Early pole-changing machines used mechanical contactors to reconfigure the coil arrangement to obtain the desired pole number [22]. For example, a 2:1 pole ratio is possible with phase coils that can be rearranged either in parallel or series-parallel connection. Figure 1.2 shows a winding with its coils connected in series. This arrangement sets up 8 poles around the stator.
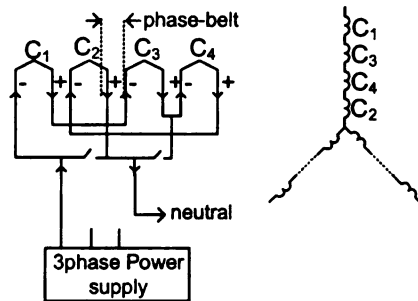
Figure 1.2: Series connected phase coils resulting in 8-poles.

Changing the state of the switches rearranges the windings into a 4-pole configuration as shown in figure 1.3.

The switching changes the number of adjacent coils, effectively changing the length of the phase-belt. In figure 1.3 there are two adjacent coils within the same phase in the 4-pole configuration; as a result the phase-belt width is doubled. By doubling the phase-belt width, the number of poles is reduced by half.

A second technique for reconfiguring the stator windings, by Rawcliffe and Jayawant [21], adjusts the phase-belt by a factor of three. This specially designed 3:1 pole induction machine

4
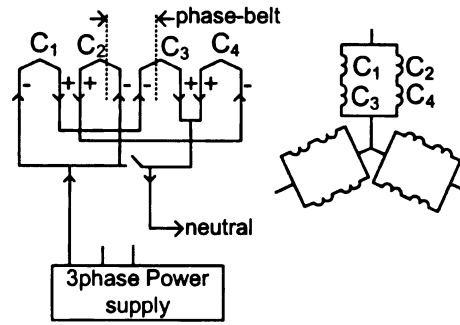
Figure 1.3: Series-parallel connected phase coils resulting in 4-poles.

has 18 leads, with 9 equally spaced phase windings. Arranging the 9 windings in a series-delta configuration results in a 2-pole machine. The phase-belt span for this arrangement is 60 electrical degrees. The number of poles for this machine can be switched from two to six by adjusting the phase-belt from 60 to 20 electrical degrees, which is accomplished by arranging the windings in a series-wye pattern.

1.4 Objectives and Thesis Outline

The overall objective of this work is the development of a drive control scheme which results in continuous operation and smooth torque production during pole-changing, utilizing the starter/alternator motor and inverter. This is accomplished by controlling the induction machine as two motors, a 3-phase/12-pole and a 9-phase/4pole motor. Energized by the same stator windings, both motors operate independently and simultaneously during the pole-changing transition. To realize this novel pole-changing control scheme several obstacles have to be overcome. In chapters 2 through 6 these obstacles are detailed, and novel solutions are presented.

One of the first challenges is developing a Pulse Width Modulation (PWM) inverter switching scheme for 9-phase operation of the motor. Very little research has been conducted on systems with more than three phases. In chapter 2, the conventional 3-phase Space Vector Pulse Width Modulation (SVPWM) switching scheme is extended for 9-phase systems. A gener-

alized SVPWM algorithm is also developed for n-phase systems. In addition, an analysis is conducted on the operation of the 9-leg inverter of the starter/alternator system, resulting in all 512 switching states. By choosing switching states that result in lower switching losses, several modified 9-phase Space Vector Pulse Width Modulation (SVPWM) switching schemes are developed.

Knowledge of the air-gap flux is pertinent in the pole-changing scheme developed in chapter 7. As a result, the magnetomotive force (MMF) of both the 12-pole/3-phase and 4-pole/9-phase motors is studied in chapter 3. The MMF harmonic content of both configurations is presented.

Since the starter/alternator was originally intended a 3-phase system, 9-phase motor parameters did not exist. In the second part of chapter 3, the motor parameters of both configurations are analytically and experimentally determined. These values are used in the control of the machine in chapter 7.

Rotor Flux Field Orientated Control (R-FOC) is the basis of the novel, drive control scheme of chapter 7. For conventional R-FOC, machine variables, i.e. current and voltages, are mapped between the symmetrical 3-phase coordinate system and the imaginary-real coordinate system using Parks Transformation [13]. For electrically balanced systems, the transformation between the symmetrical 3-phase and 2-phase system is unique. For field orientation control of the 9-phase/4-pole motor, a method for choosing a transformation between the 9-phase symmetrical and imaginary-real coordinate systems is developed in chapter 4. With the objective of equalizing the current density around the stator and decreasing winding loses, a coordinate transformation for the 9-phase/4-pole motor is developed. However, the real benefit of this transformation is the decoupling of the controls of both motors when operated simultaneously.

In order to evaluate the drive control scheme and to study torque and current transients during pole-changing, an unconventional induction motor plant model is developed. Transients resulting from pole-changing can not be simulated using classical induction motor modeling. Instead, in chapter 5, a model is developed using fundamental electromagnetics. The machine

inductances are developed from the Fourier series of the actual, non-sinusoidal, stator winding distribution.

For validation, a complete drive system, including a field programable gate array (FPGA) IO/SVPWM processor, was designed and built for this work. Chapter 6 describes the software architecture, which was also developed for this work.

Finally, chapter 7 details the operation of the newly developed drive. First, current and speed control are demonstrated for both the 4-pole/9-phase and 12-pole/3-phase motor configurations. The novel drive control scheme presented here is based on controlling the machine as two independent motors using the same stator windings and producing torque simultaneously. The flux and electromagnetic torque produced by both motors are controlled independently. During the pole transition, the orthogonal current sets of both the 9-phase/4-pole and 3-phase/12-pole motors are controlled to produce the necessary flux to create a smooth, constant torque and avoid saturation. Both simulated and experimental data are presented. Finally, an overall torque management strategy is presented. This strategy is used to determine when and if pole-changing is necessary.

CHAPTER 2

Nine Leg Inverter

2.1 Introduction

The 3-leg inverter is the most commonly used inverter to power AC machines; however, there are applications where an n-leg, n-phase ($n > 3$) inverter is needed. One such application is pole-phase modulation control of an induction motor. Pole-phase modulation can extend the speed-torque range of an induction motor by adjusting the pole-phase ratio. For example, a nine-phase, symmetrically wound induction machine can operate as either a four- or twelve-pole machine. This is accomplished by reconfiguring the nine-leg inverter as either a nine-phase or a three-phase voltage source [9]. Extended speed-torque range is desired for several automotive induction motor applications. This chapter will provide a comprehensive analysis of a multi-leg, multi-phase inverter and propose techniques for its implementation.

First, the n-leg inverter will be examined in terms of the load equivalent circuit during a $2\pi/n$ switching period. Unlike the three-phase inverter, which has only one load equivalent circuit, an n-leg inverter has $(n - 1)/2$ load equivalent circuits. Each one of these equivalent circuits can be operated in a n-step mode to produce a unique discrete AC or 'stair-step' voltage waveform. These waveforms differ in terms of harmonic content and magnitude of the fundamental component. As shown by Holtz [6], the fundamental component of the three-phase 6-step voltage waveform is $2V_{dc}/\pi$. On the other hand, a nine-phase inverter has four different such voltage waveforms, with fundamental components of $0.64V_{dc}$, $0.56V_{dc}$, $0.41V_{dc}$,

$0.22V_{dc}$.

For most electrical machines, the windings are assumed to be sinusoidally distributed in the stator. Voltage space-vectors are defined based on the voltages applied to the windings. For the conventional three-phase inverter, connected to an electrical machine, there are eight space-vectors possible. For a n-leg, inverter connected to a n-phase machine, there are 2^n possible space-vectors.

The implementation of PWM in a multi-leg, multi-phase inverter is examined. In particular, a generalized implementation method for Space-Vector PWM (SVPWM) is presented [12],[7]. The theory of Space-Vector PWM and its implementation through the Unified theory [2] are extended to many phases. Additional novel algorithms, particular to multi-phase machines, are presented and compared.

Throughout this chapter, a nine-leg, nine-phase inverter will be used as a practical example. In the final section, experimental data from a nine-phase SVPWM system will be presented.

2.2 Analysis of a Nine-Leg Inverter

The nine-leg inverter in figure 2.1 requires eighteen gating signals, g1-g18. The gating combination determines the phase voltage across each of the nine separate loads, which are connected at a point to form a star.
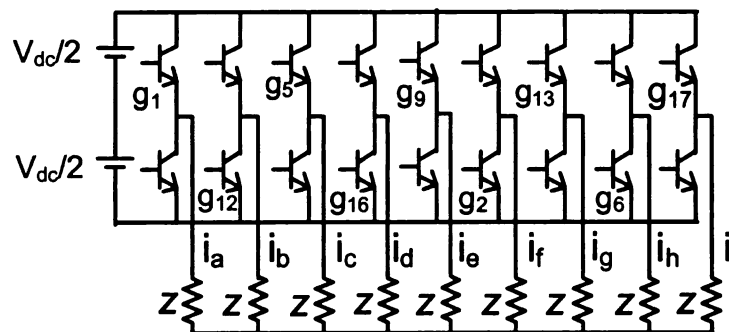
Figure 2.1: Nine-leg inverter

Depending on the gating pattern, the nine phase loads can form four different equivalent

circuits. For example, when the gating pattern is $[g1, g3, g5, g7, g18, g2, g4, g6, g8]$ the load equivalent circuit consists of a group of four parallel impedances in series with a group of five parallel impedances as shown in Figure 2.2-a.

a) 4-5 Configuration   b) 3-6 Configuration

c) 2-7 Configuration   d) 1-8 Configuration
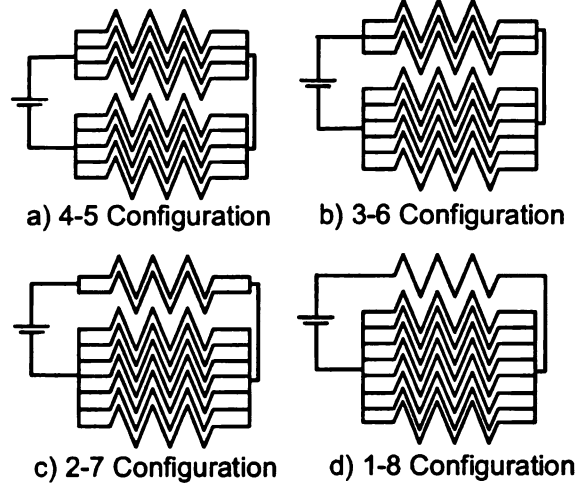
Figure 2.2: The four equivalent load configurations of a nine-leg inverter

Likewise, the 3-6 equivalent circuit configuration shown in figure 2.2-b, is formed by three parallel impedances in series with a group of six parallel impedances. One of the possible inverter gating patterns for this case is $[g1, g3, g5, g16, g18, g2, g4, g8]$ or, in terms of energized inverter legs, [11100000],where '1' represents the upper switch of the inverter leg closed and the lower switch open. The other two possibilities are the 2-7 and the 1-8 configuration, figures 2.2-c,d.

2.2.1   Load Circuit Analysis

Table 2.1 shows the equivalent impedance, source current and the maximum phase current for the four different load circuits. The corresponding quantities for a three-phase inverter were included for comparison. Of the four possible load circuit configurations, the 4-5 configuration results in maximum phase current and the smallest ratio of phase current to source current. For the 1-8 configuration, one inverter leg carries the entire source current, while the other eight legs carry only 1/8th of the total current.

Configuration 9 phase inverter	Equivalent Impedance	Equivalent Current	Maximum Phase Current	Ratio : $I_{phase\ max.}$ / I_{total}
4-5	$9Z/20 = 0.45Z$	$20Vdc/9Z$	$5Vdc/9Z$	0.25
3-6	$10Z/20 = 0.5Z$	$18Vdc/9Z$	$6Vdc/9Z$	0.33
2-7	$9Z/14 = 0.64Z$	$14Vdc/9Z$	$7Vdc/9Z$	0.5
1-8	$9Z/8 = 1.125Z$	$8Vdc/9Z$	$8Vdc/9Z$	1.0
3 phase inverter	$3Z/2 = 1.5Z$	$6Vdc/9Z$	$6Vdc/9Z$	1.0

Table 2.1: Equivalent Circuit Comparison

2.2.2 n-Step Inverter Operation

In a three-phase inverter operating in six-step mode, switching states are changed every sixth of a cycle. The four potential phase voltage levels are $\pm V_{dc}/3$ and $\pm 2V_{dc}/3$. The sequence of the six switching states is such that only one switch changes state. This sequence produces three phase voltages that are displaced 120°and that appear in 'stair-step' shape, as shown in figure 2.3. For eighteen-step mode, the nine-leg inverter changes switching states every eigh-
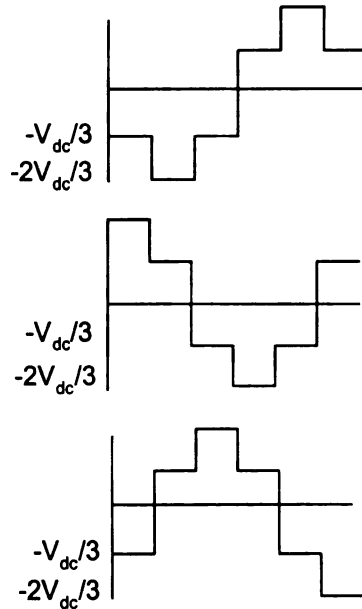
Figure 2.3: Phase voltages of a three-phase inverter

11

teenth of a cycle. In order to produce nine symmetrical phase voltages, the nine-leg inverter is restricted to operate in one of the four configurations during the complete cycle. This is because a single-level inverter can only produce four different voltage levels during a switching interval. Each of the four possible load circuit configurations produce only four distinct voltage levels. For example, the 4-5 configuration results in phase voltage levels of $\pm 4/9 V_{dc}$ and $\pm 5/9 V_{dc}$. Figure 2.4 shows the upper gating signals for eighteen-step operation in the 4-5 configuration, along with the resulting nine phase voltages, $(V_a ... V_i)$.
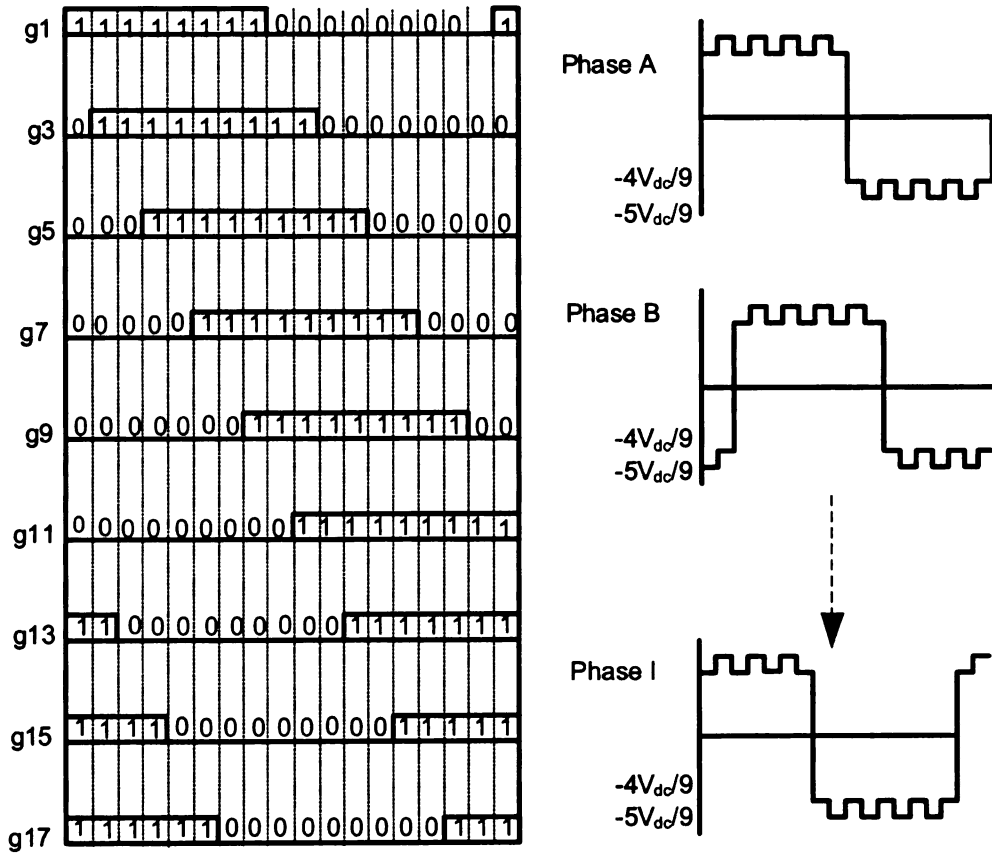
Figure 2.4: 4-5 eighteen-step operation: gating signals(upper switches) and the resulting phase voltages

Note in figure 2.4, that only one switch changes states between consecutive conduction intervals. Similarly, the gating signals and resulting phase voltages for 2-7 eighteen-step operation are shown in figure 2.5.
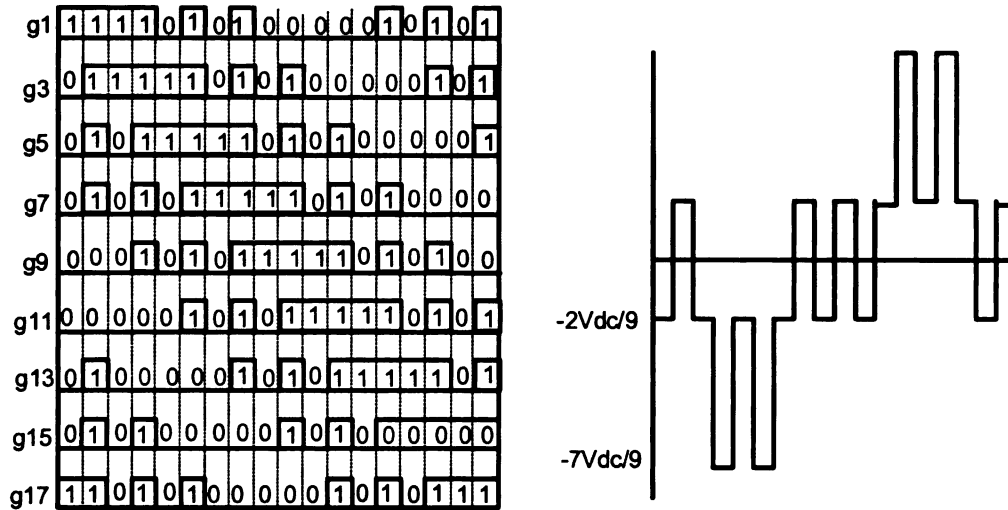
Figure 2.5: 2-7 eighteen-step operation: gating signals (upper switches) and one of the resulting phase voltages

2.2.3 Inverter Switching Efficiency

In the 2-7 mode of operation of figure 2.5, five switches change state between conduction intervals. For modes 1-8, 3-6 and 4-5, seven, three and one switches, respectively, change state. An inverter operating continuously in the 4-5 switching set would have greater switching efficiency than one operating in the 1-8 switching mode. More switches have to change states to change voltage levels from $1/9V_{dc}$ to $8/9V_{dc}$ than from $4/9V_{dc}$ to $5/9V_{dc}$.

2.2.4 Harmonic Content

For a three-phase inverter, switching every sixth of a cycle, the phase voltage has a fundamental of $2/\pi V_{dc}$. Table 2.2 shows the result of a fundamental magnitude of the waveforms of figures 2.4 and 2.5.

For a nine-leg inverter operating in eighteen-step mode, the 4-5 switching set waveform has the highest fundamental content. The 1-8 switching set has the lowest fundamental content.

Configuration	Fundamental n=1	3rd order n=3	5th Order n=5	7th Order n=7
3 phase inverter	0.6366=2/pi	0	0.1273	0.0909
Four-Five	0.6366=2/pi	0.2122	0.1273	0.0909
Three-Six	0.5598	0	0.1715	0.2303
Two-Seven	0.4155	0.2122	0.0677	0.2619
One-eight	0.2211	0.2122	0.1951	0.1709

Table 2.2: Harmonic Content of 18-step mode Voltage Waveforms

2.3 Extension of Space Vector Theory to n Phases

Symmetric time-varying electrical quantities operating on spatially distributed functions (e.g. windings) give rise to the concept of space-vectors. In an AC machine stator, voltages are assigned a direction (that of the winding spatial distribution) and their vectorial sum defines the corresponding voltage space-vector.

2.3.1 Three Phase Space-Vectors

For symmetric three-phase voltages, the resulting space-vector, v_s, sweeps a continuous circular path in the imaginary-real reference frame. It rotates at the frequency of the terminal
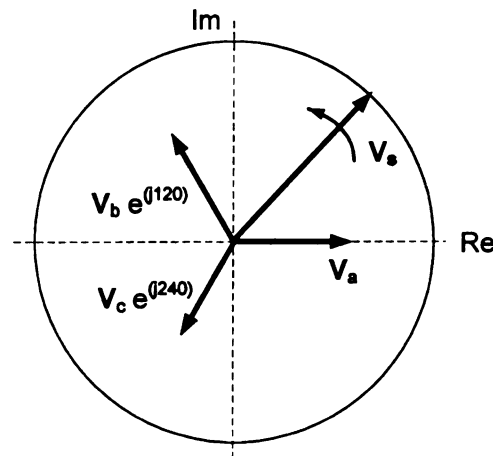
Figure 2.6: Phase voltages of a 3-phase inverter and resultant voltage space-vector

voltages. If, however, a three-leg inverter supplies the voltage, there are only six angular positions the voltage space-vector can take at any instance. The three-leg inverter results in 2^3

14

possible space-vector positions. The six non-zero vectors form a hexagon.

2.3.2 Nine Phase Space-Vector

For a nine-phase machine fed by a nine-leg inverter, there are 2^9 possible voltage space-vectors. Figure 2.7 shows all the possible positions of the resultant vectors.
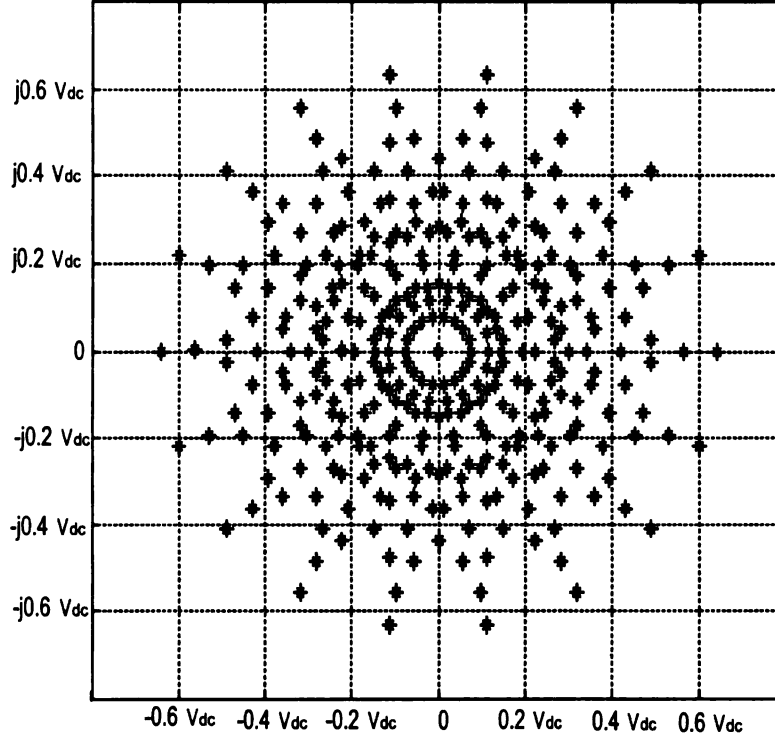
Figure 2.7: Nine-phase voltage space-vectors

The 512 resultant space-vectors of figure 2.7 can be divided into four sets,[4-5],[3-6],[2-7],[1-8], based on the load circuit configuration as discussed the previous section. These four sets can further be divided based on the number of adjacent 'on' inverter switches. For example, the eighteen outermost space-vectors of figure 2.7 are the result of switching combinations of either four or five adjacent 'on' switches. Specifically, these space-vectors correspond to the 18 switching states which form the $\{4, 5\ max\}$ subset. The magnitudes of these vectors are a result of adjacent phase vectors contributing positively to the resultant voltage space-vector (see figure 2.8).

15

a) [0 0 0 0 1 1 1 1 1]   b) [0 0 0 1 0 1 1 1 1]
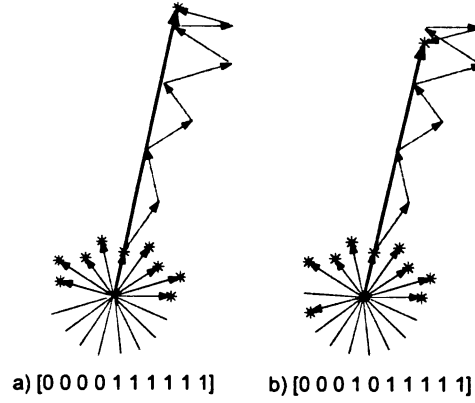
Figure 2.8: Vector addition of voltage phase space-vectors

Space-vectors corresponding to the four maximum magnitude subsets,$\{4, 5 \ max\}$, $\{3, 6 \ max\}$, $\{2, 7 \ max\}$ and $\{1, 8 \ max\}$ form four 18-sided polygons, shown in figure 2.9. The polygons enclose all the subsets of the four switching sets.
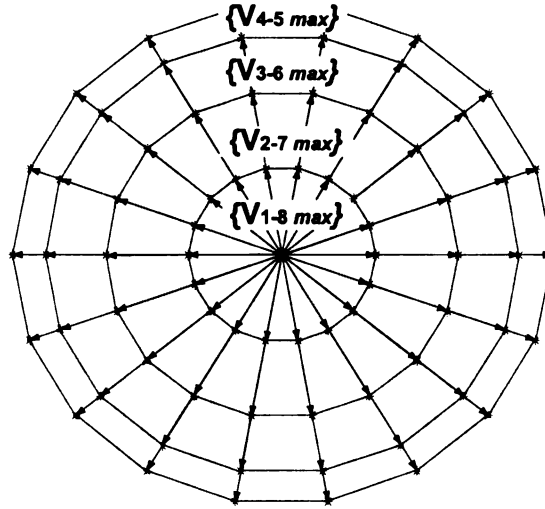
Figure 2.9: The four bounding voltage space-vector subsets of a nine-phase system

In general, the number of polygons is equal to the number of equivalent load circuits. The next section will show how vectors that form these concentric polygons are used in a multi-phase Space Vector Pulse Width Modulation algorithm.

16

2.4 Space-Vector PWM implementation

Pulse Width Modulation is a general technique for realizing a voltage reference via an inverter. The duration of the gating pulses controls the frequency and magnitude of the inverter output voltage. Space Vector Pulse Width Modulation (SVPWM) is a PWM technique which uses space-vectors to generate these gating durations.

First, a review of a three-phase SVPWM will be presented, followed by a proposed general SVPWM algorithm, which extends the present three-phase SVPWM to an n-phase SVPWM. Finally, several multi-phase SVPWM techniques are presented.

2.4.1 Three-Phase Space-Vector PWM

Three-phase SVPWM [6] increases the DC bus utilization compared to PWM based on Sine-Triangle comparison [20]. By injecting the third harmonic into the reference voltage signal, the fundamental of the phase voltage can be increased. SVPWM is implemented by averaging the time spent in adjacent switching states.
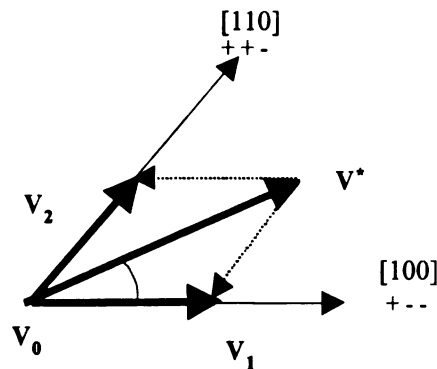
Figure 2.10: Three phase Space Vector PWM

In figure 2.10, the desired voltage v^* is realized by spending t_1 time in switching state [100], t_2 time in switching state [110] and t_0 in the zero switching state.

The drawback of this algorithm is the need for trigonometric calculations. This method can be simplified by adding a voltage offset to the phase voltages [2]. The addition of this offset centers the three voltage reference signals about the dc axis, implicitly adding the third

harmonic and allowing the three signals to be increased. The operation requires only addition and multiplication operations. This algorithm is extended for n-phase systems in the next section.

2.4.2 Extension of three-phase SVPWM to n-Phase SVPWM

For an n-phase system, the nth harmonic signal can be injected by adding $V_{n\,offset}$ to the voltage reference. The offset signal is

$$V_{n,\,offset} = max \left[\frac{V_1}{V_{dc}} ... \frac{V_n}{V_{dc}} \right] - min \left[\frac{V_1}{V_{dc}} ... \frac{V_n}{V_{dc}} \right] \tag{2.1}$$

Realizing a voltage space-vector by applying this algorithm to a nine-phase inverter results in the switching states shown in figure 2.11.

Figure 2.11: The Space Vector PWM Realization of the vector $1.0e^{j30°}$

Also shown in figure 2.11 are the nine upper gating pulses. The switching states generated by this algorithm are exclusively from the four subsets described in the previous section. Also apparent in figure 2.11 is that only one switch changes state at a time. Figure 2.12 shows the switching state sequence, for half a sampling period, in terms of corresponding space-vectors.

18

Figure 2.12: Vector sequence for the realization of the voltage space vector $1.0e^{j30°}$

The switching times, $[t_0\ t_1\ t_2\ t_3\ t_4\ t_5\ t_6\ t_7]$, of figure 2.11 can be determined by solving

$$V^* \frac{|V_{1,8\ max}|}{V_{Total}} = \kappa[(t_8 + t_1 e^{j\frac{\pi}{9}})] \tag{2.2}$$

$$V^* \frac{|V_{2,7\ max}|}{V_{Total}} = \kappa[(t_2 + t_7 e^{j\frac{\pi}{9}})] \tag{2.3}$$

$$V^* \frac{|V_{3,6\ max}|}{V_{Total}} = \kappa[(t_6 + t_3 e^{j\frac{\pi}{9}})] \tag{2.4}$$

$$V^* \frac{|V_{4,5\ max}|}{V_{Total}} = \kappa[(t_4 + t_5 e^{j\frac{\pi}{9}})] \tag{2.5}$$

$$\tag{2.6}$$

$$t_o + t_1 + t_8 + t_2 + t_7 + t_3 + t_6 + t_4 + t_5 = \frac{1}{2f_s} \tag{2.7}$$

$$V_{Total} = (|V_{1,8\ max}| + |V_{2,7\ max}| + |V_{3,6\ max}| + |V_{4,5\ max}|) \tag{2.8}$$

$$\kappa = \frac{1}{3} 2 f_s \frac{2}{9} (2\cos(20°) + 1) V_{dc} \tag{2.9}$$

The reference voltage vector of figure 2.12 can be constructed from vectors which are proportional to the vectors of $\{V_{4,5\ max}\}$, $\{V_{3,6\ max}\}$, $\{V_{2,7\ max}\}$ and $\{V_{1,8\ max}\}$.

$$\mathbf{v}^* = 2f_s \left[|V_{1,8\ max}|(t_1 e^{j\frac{\pi}{9}} + t_8 e^{j0}) + |V_{2,7\ max}|(t_3 e^{j\frac{\pi}{9}} + t_6 e^{j0}) \right.$$
$$\left. + |V_{3,6\ max}|(t_7 e^{j\frac{\pi}{9}} + t_2 e^{j0}) + |V_{4,5\ max}|(t_5 e^{j\frac{\pi}{9}} + t_4 e^{j0}) \right] \tag{2.10}$$

In (2.9), f_s is the sampling frequency and V_{dc} is the dc bus voltage. The term $1/3$ adjusts for the number of turns per phase. A winding of a nine-phase system has one third the number of turns per phase than a winding in an equivalent three-phase system. Equivalent systems are defined as those systems that produce equal air-gap flux for the same voltage. Figures 2.13.a and b illustrate the placement of windings for a machine designed to operate as either a nine-phase or three-phase system. This machine will produce the same flux in either configuration.

19
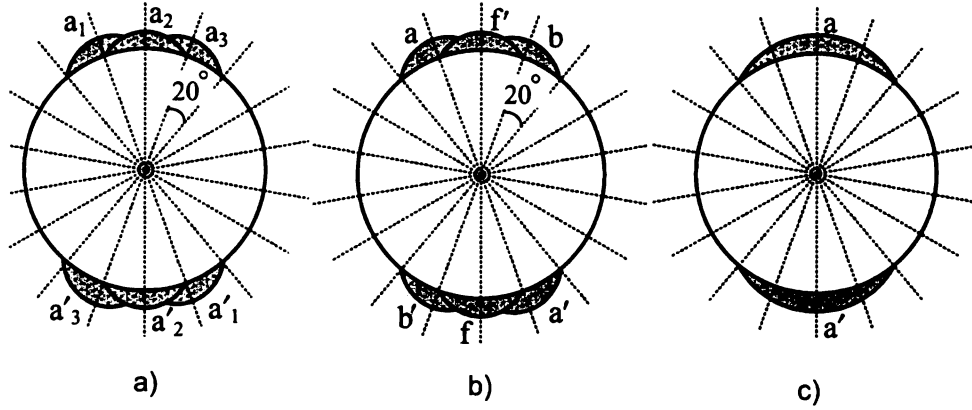
Figure 2.13: a) Windings of a 3/9 phase machine in 3-phase operation b) 9-phase operation c) Windings of a conventional 3-phase machine

Figure 2.13.c shows the winding configuration of a conventional three-phase machine with the same number of turns. The resultant winding distribution factor for one phase in figure 2.13.a will be less than that of figure 2.13.c. Therefore, the resulting voltage space-vectors will have lower magnitude. For a conventional three-phase machine, the six possible non-zero voltage space-vectors have a magnitude of $\frac{2}{3}V_{dc}$, while for the three-phase machine of figure 2.13.a the voltage vectors have a magnitude of $2/9(2\cos(20°) + 1)V_{dc} \approx 2/\pi$.

We define the modulation index as the ratio of the fundamental of the output voltage, V_1, to the dc input voltage.

$$m = \frac{V_1}{V_{dc}} \tag{2.11}$$

When SVPWM is applied to the conventional three-phase machine of figure 2.13.c, the maximum possible modulation index is:

$$m_{3\phi\ max} = \frac{\sqrt{3}}{3} \tag{2.12}$$

For the equivalent system of figure 2.13.a, the maximum possible modulation is:

$$m_{3\phi\ max} = \frac{\sqrt{3}}{\pi} \tag{2.13}$$

When the same machine is operated in a nine-phase mode, using extended three-phase SVPWM, the maximum index is

$$m_{9\phi\ max} \approx 0.507 \tag{2.14}$$

20
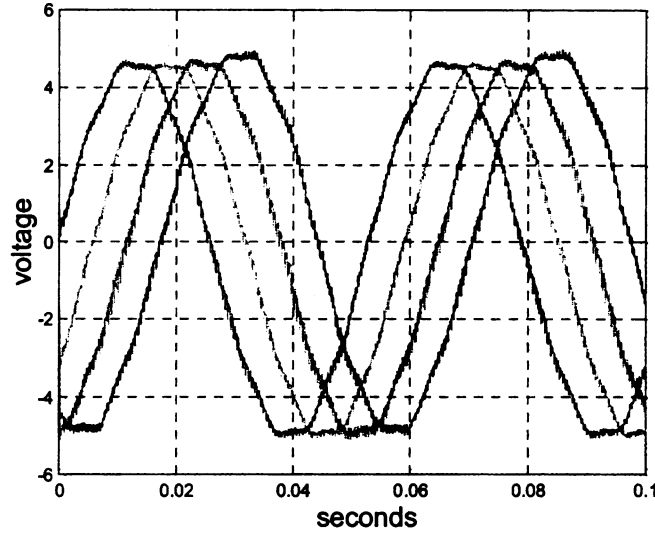
Figure 2.14: Four phase voltages of a 9-phase load generated by a 9-phase SVPWM scheme

As shown in figure 2.14, the ninth order harmonic is present in the phase voltages. This harmonic injection increases the fundamental content of the waveform and is filtered in a nine-phase load. However, the increase in fundamental content is not as great as that created by third order harmonic injection in the three-phase system, 0.507 vs. 0.577.

As the number of phases increases, the magnitude of the voltage offset decreases to zero and SVPWM converges to Sine-Triangle PWM.

2.4.3 Proposed n-phase SVPWM Techniques

In order to increase the fundamental phase voltage in an n-phase SVPWM system, several SVPWM techniques are proposed. The first technique allows for lower order harmonic injection into a system with many phases. The second proposed SVPWM technique uses only those vectors that form the concentric n-sided polygons described in section 2.4. The third technique is related to the second one, as it uses the same vectors; however, the zero space-vectors are not always used.

2.4.4 Low Order Harmonic Injection

The proposed technique allows for the $\sqrt{n}$ order harmonic to be injected into an n-phase system. The advantage of this technique is the increased fundamental content of the output voltage due to the lower order harmonic injection. However, $\sqrt{n}$ separate neutrals have to be used.

In the case of a nine-phase system, the nine-phase symmetrical load is treated as three, three-phase systems displaced $40°$, each producing one third of the total voltage space-vector. Conventional three-phase SVPWM is applied to each of the three systems to realize the voltage command.

2.4.5 SVPWM Using Maximum Subsets

Equation 2.10 is based on the use of space-vectors from the $\{V_{4,5\ max}\}...\{V_{1,8\ max}\}$ sub-sets. However, the reference voltage space-vector can be realized by using two vectors from $\{V_{4,5\ max}\}$ and two zero vectors. Figure 2.15 shows how the reference voltage space-vector of figure 2.12 is realized using four such vectors.

```
000000000
100000111
100001111
111111111
111111111
100001111
100000111
000000000
```
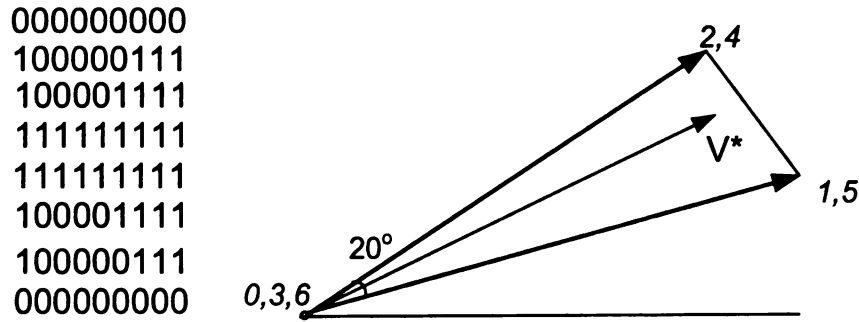

Figure 2.15: Voltage space-vector realization using vectors from $\{V_{4,5\ max}\}$ subset and zero vectors

The maximum modulation index in this case is

$$m_{9\phi\ max} = (\frac{2}{\pi})(\cos(10°)) = 0.63 \tag{2.15}$$

During one sampling period, 18 switches change state. This is the same number of

switches that change state for the extended three-phase SVPWM technique discussed in section 2.4.2.

The switching times for this scheme can be determined by reducing (2.10) to (2.5) with $V_{Total} = V_{4,5\ max}$.

The advantage of using only vectors of the subset $\{V_{4,5\ max}\}$ is that the inverter operates in the 4-5 equivalent load configuration, which results in a greater modulation index, at the cost of increased harmonic content (see Table 2.2). The harmonic content can be reduced by including vectors of subset $\{V_{3,6\ max}\}$. However, the maximum modulation index is also reduced. The switching times are determined by solving (2.4) and (2.5), with $V_{Total} = V_{4,5\ max} + V_{3,6\ max}$.

2.4.6 Modified SVPWM With Adjusted V_{zero}

In previously discussed n-phase SVPWM schemes, the zero space-vectors are used. This is a necessity for three-phase SVPWM, because at least three switching states are needed to realize a desired space-vector. The use of zero voltages in the SVPWM scheme of section 2.4.5 result in four switches being simultaneously changed. In order to avoid this and improve switching efficiency, a non-zero vector is used instead. In general, the closer in proximity the space-vectors are, the greater the switching efficiency.

The previous SVPWM techniques use eighteen switching sectors, bounded by the vectors of $\{V_{4,5\ max}\}...\{V_{1,8\ max}\}$. This technique subdivides each sector into four regions as shown in figure 2.16. The angle of the desired voltage space-vector determines the sector, while its magnitude determines the region within that sector. Within each region the voltage space-vector is realized by the space-vectors of the indices of that region.

For the hatched region of figure 2.16, a desired voltage space-vector can be realized using the four vectors [100001111], [100000111], [000000111], [110001111]. Figure 2.17 depicts the corresponding space-vector sequence.

To generate the vector $\mathbf{v}^*$ six switches change state, compared to eighteen switches for the SVPWM schemes of sections 2.4.2 and 2.4.5. The proposed switching algorithm results in a maximum of two switches changing between adjacent regions. For example, one switch

23
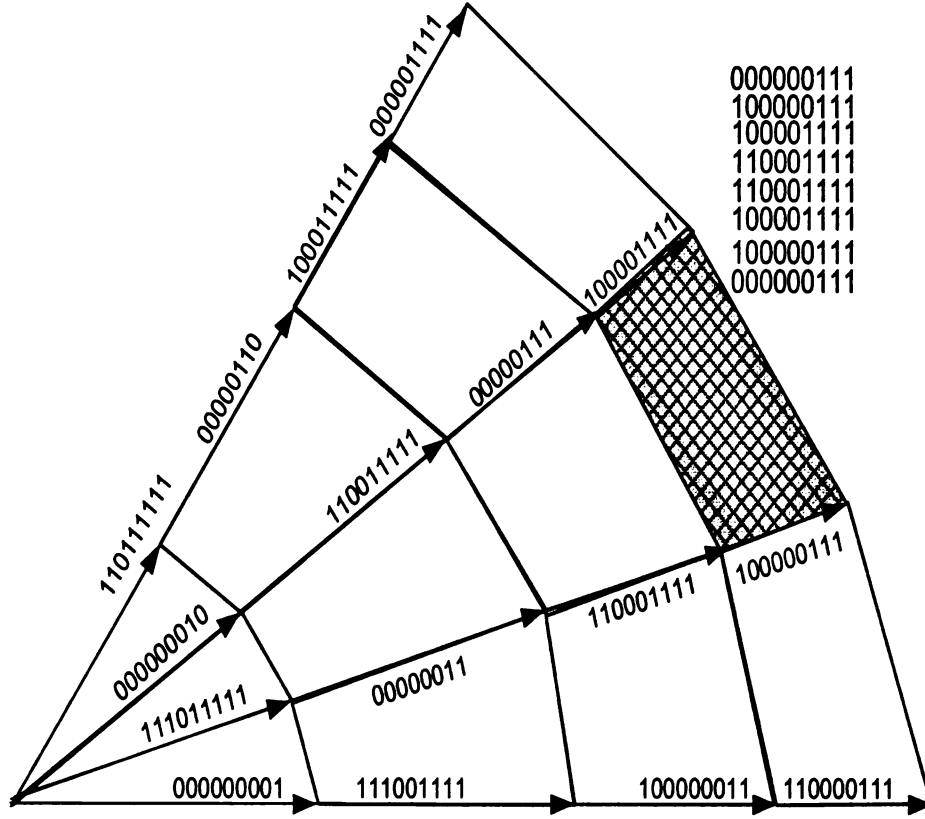
Figure 2.16: Switching schemes for adjacent sector regions

changes states when the desired voltage vector changes from the region bounded by $\{V_{4,5\ max}\}$ and$\{V_{3,6\ max}\}$ to a neighboring region bounded by $\{V_{3,6\ max}\}$ and$\{V_{2,7\ max}\}$.

2.4.7   Conclusions

Pole-phase modulation requires the use of a multi-phase system since the phase order is adjusted, as well as the number of poles. The necessity of implementing $(n > 3)$phases via a n-leg inverter resulted in the proposal of several novel n-phase SVPWM techniques.

The first technique was the extension of conventional three-phase SVPWM to higher order phase systems. However, this resulted in lower utilization of the dc bus voltage. The second technique treated the multi-phase system as a sum of lower order phase systems. This technique resulted in higher dc bus utilization through the injection of the lower order harmonics. However, it is no longer possible to have one neutral.

```
000000111
100000111
100001111
110001111
110001111
100001111
100000111
000000111
```
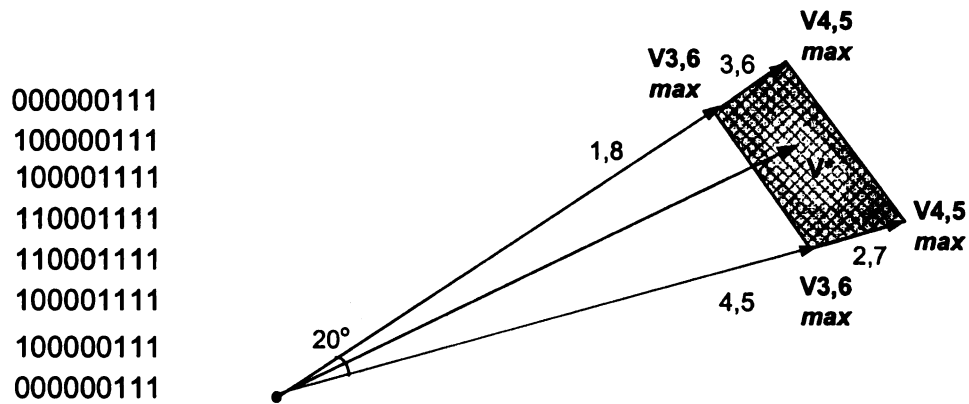
Figure 2.17: The vector sequence for realizing V^*

The third proposed technique utilizes the fact that a multi-phase system has more than one equivalent load configuration. Along with the zero space-vectors, this technique uses only space-vectors from a maximum subset (or a combination of maximum subsets) to realized a desired voltage.

Similar to the third technique, the fourth technique uses only a limited number of switching states; however, it does not necessarily use the zero space-vectors, improving switching efficiency.

CHAPTER 3

Analysis of the Experimental Pole-Changing Induction Machine

3.1 Introduction

With the 9-leg inverter supplying the pole-changing induction machine, three possible motor configurations are possible, the 3-phase/4-pole, the 3-phase/12-pole and the 9-phase/4-pole motor configurations. Therefore, the two possible combinations for extending speed/torque capabilities are: 1) 3-phase/4-pole and 3-phase/12-pole or 2) 9-phase/4-pole and 3-phase/12-pole.

It was shown in [24] that in the 3-phase/4-pole motor configuration the bemfs are unbalanced and result in circulating winding currents. Therefore, pole-changing will be between the 3-phase/12-pole and the 9-phase/4-pole motor configurations. However, all three configurations are discussed in detail in terms of coil arrangements, Fourier Series winding distribution, and MMF. Comparisons are made between the harmonic content of the resulting MMF waves of the three configurations. The understanding of the winding density and MMF facilitates the fundamental modeling of the induction motor in chapter 5.

The motor parameters for 9-phase/4-pole configuration were not provided. Therefore, in the second part of the chapter the machine parameters are analytically and experimentally

determined.

3.2 Three Possible Stator Winding Configurations

The experimental machine has seventy two stator slots and eighty seven rotor slots. The machine has nine windings with eighteen accessible leads. Each of the windings has four coil groups in series, each consisting of two coils in series occupying adjacent stator slots.

The four coil groups that make up a winding are spatially offset by 90° in the stator. Figure 3.1 shows the nine stator windings and their respective coil groups.

i_{A1}	i_{B2}	i_{C3}	i_{A4}	i_{B5}	i_{C6}	i_{A7}	i_{B8}	i_{C9}	12p 3phase
i_{A1}	$-i_{A2}$	i_{A3}	i_{B4}	$-i_{B5}$	i_{B6}	i_{C7}	$-i_{C8}$	i_{C9}	4p 3phase
i_{A1}	i_{B2}	i_{C3}	i_{D4}	i_{E5}	i_{F6}	i_{G7}	i_{H8}	i_{I9}	4p 9phase

Figure 3.1: The coil arrangements and applied voltages for the 3 motor configurations

The machine was originally designed to operate as either a 3-phase/12-pole motor or a 3-phase/4-pole generator. For both configurations, a wye connection is used. The fact that every other coil in a group is wound in an opposite direction allows for the same neutral in both configurations. However, it was discovered that for the 3-phase/4-pole configuration

the reverse wound coil had a back emf voltage that is 200° out of phase with respect to the adjacent same phase coils. This large phase difference results in large circulating currents in the windings. The issue was solved by changing the phase order of the machine from 3-phase to 9-phase.

3.2.1 3-phase 12-pole Configuration

The 3-phase/12-pole configuration was designed to produce high torque at relatively low speeds. For this configuration, the nine windings of the machine are arranged in three parallel sets. Each set consists of three same-phase windings. This arrangement results in a phase belt of 10°, as shown in figure 3.2.
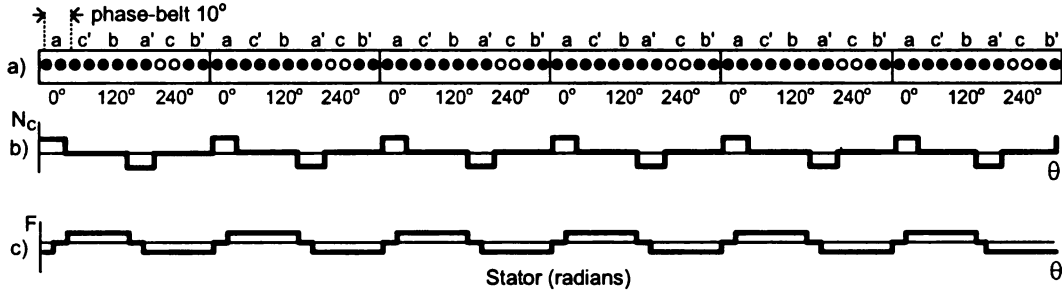
Figure 3.2: a) Coil arrangement, b) winding density $n(\theta)$ and c) resulting mmf $F(\theta)$

As shown in figure 3.2.b the winding density distribution is discontinuous over the stator with the maximum number of conductor per slots of N_c. A Fourier Series approximation of the winding density and the stator mmf was taken to better understand the stator air-gap flux distribution.

The Fourier series expansion of density distribution of one of the stator's winding is:

$$n(\theta) = a_o + \sum_{k=1}^{k=i}(a_k \cos(k\theta) + b_k \sin(k\theta)$$

$$a_o = \frac{1}{2\pi}\int_{-\pi}^{\pi} n(x)dx$$

$$a_k = \frac{1}{\pi}\int_{-\pi}^{\pi} n(x)\cos(kx)dx$$

$$b_k = \frac{1}{\pi}\int_{-\pi}^{\pi} n(x)\sin(kx)dx$$

28

The Fourier series for the density of one winding of the 3-phase/12-pole configuration is:

$$a_o = \frac{N_c}{\pi}\left[\int_0^y (-1)d\theta + \int_y^{2y}(0)d\theta + \int_{2y}^{3y}(1)d\theta \cdots \int_{71y}^{72y}(-1)d\theta\right]$$

$$a_n = \frac{N_c}{\pi}\left[\int_0^y (-1)\cos(nx)dx + \int_y^{2y}(0)\cos(nx)dx \cdots \int_{71y}^{72y}(-1)\cos(nx)dx\right]$$

$$b_n = \frac{N_c}{\pi}\left[\int_0^y (-1)\sin(nx)dx + \int_y^{2y}(0)\sin(nx)dx \cdots \int_{71y}^{72y}(-1)\sin(nx)dx\right]$$

$$y = \frac{\pi}{36}$$

where the integrands of the Fourier series are the position of the slots on the stator in radians.

The Fourier series for the other two windings densities are the same as equations (3.1), but with the integrands shifted by a multiple of the phase belt. For the adjacent winding the integration terms are shifted 10°. For the third winding the integration terms are shifted by 20°. The Fourier series approximation of $k = 100$, shown in figure 3.3, is one of the three winding distributions for the 3-phase/12-pole configuration.
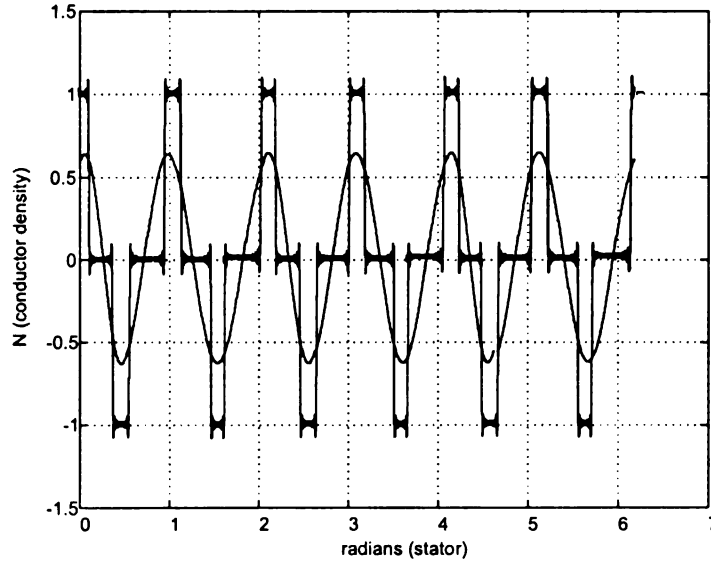
Figure 3.3: The Fourier Series Approx $(k = 100, 1)$ of Winding Density

The magnetomotive force, $F(\theta)$ in the air-gap, resulting from one stator winding is shown

in figure 3.2.c. The Fourier series expansion of $F(\theta)$ is:

$$a_o = \frac{N_c I_x(t)}{\pi} \left[\int_0^y (-1)d\theta + \int_y^{2y} (0)d\theta + \int_{2y}^{3y} (1)d\theta \cdots \int_{71y}^{72y} (-1)d\theta \right]$$

$$a_n = \frac{N_c I_x(t)}{\pi} \left[\int_0^y (-1)\cos(nx)dx + \int_y^{2y} (0)\cos(nx)dx \cdots \int_{71y}^{72y} (-1)\cos(nx)dx \right]$$

$$b_n = \frac{N_c I_x(t)}{\pi} \left[\int_0^y (-1)\sin(nx)dx + \int_y^{2y} (0)\sin(nx)dx \cdots \int_{71y}^{72y} (-1)\sin(nx)dx \right]$$

where $I_x(t)$ is the current function.

Figure 3.4 shows the single phase stator mmf with $I_x(t) = 1$. The figure show two plots; one is the fundamental of the mmf $(k = 1)$, and the other is the Fourier series approximation if the mmf taken out to the 100 term, $(k = 100)$.
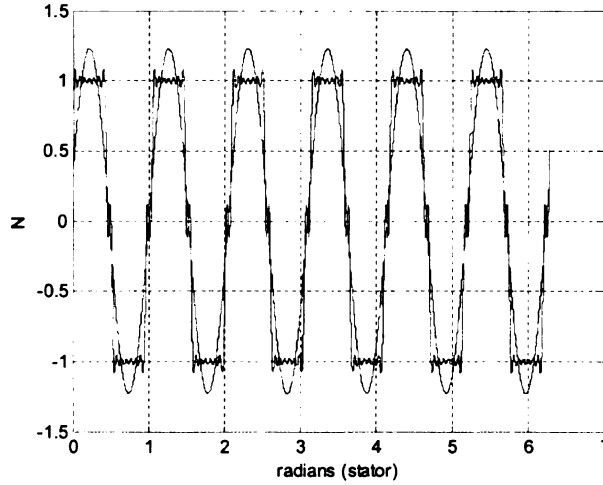
Figure 3.4: The Fourier series Approx $(k = 100, 1)$ of the air-gap mmf

However, for steady state analysis the applied currents will be sinusoidal and 120° apart:

$$I_a(t) = \sin(2\pi f(t))$$
$$I_b(t) = \sin(2\pi f(t) + \frac{2\pi}{3})$$
$$I_c(t) = \sin(2\pi f(t) + \frac{4\pi}{3})$$

When these currents are applied to the 3-phase windings of the 3-phase/12-pole configuration, a sinusoidal stator air-gap mmf is developed. For purposes of analysis, the frequency of the applied current is $10Hz$. Figure 3.5 shows the Fourier series approximation $(k = 100)$ of the
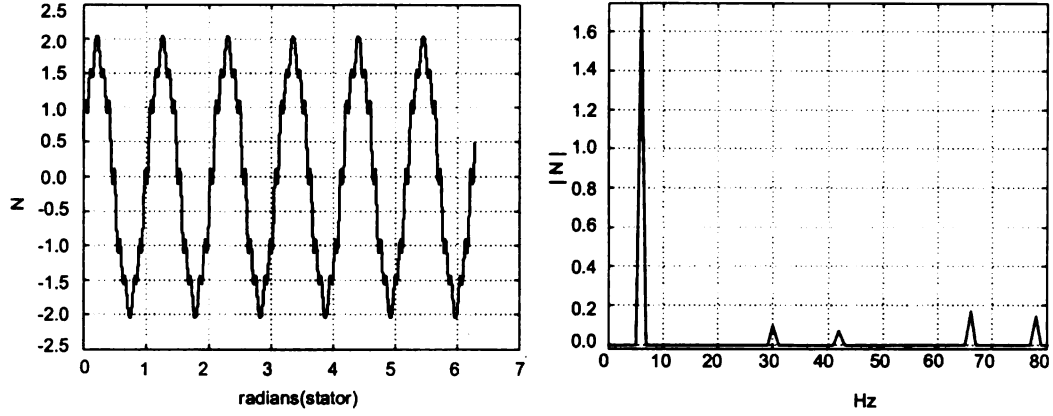
Figure 3.5: a)Instantaneous air-gap mmf and b) resulting Fourier Transform

air-gap mmf at one instance of time. In addition, the a Fourier transform is applied to the wave form. From the Fourier transform plot the fundamental is at 6 hz. However, hertz is not in terms of seconds but stator position. In this case, 6 hz means 6 cycles per one diameter of the stator. Also notice there are four other frequency components at 30, 42, 66, and 78 hz which correspond to the 5th, 7th, 11th and 13th harmonic. In order to measure the amount of harmonic content in the instantaneous stator air-gap mmf, the total harmonic distortion was calculated using equation (3.1). For this instant of time the THD for the air-gap mmf is approximately 21%.

$$THD = \frac{F^2_{RMS} - F^2_{fundametal}}{F^2_{fundametal}} \tag{3.1}$$

The previous frequency analysis was performed on the stator air-gap mmf at an instant of time. Next, an analysis of how the stator air-gap mmf changes with time is conducted. Figure 3.6 shows the resulting amplitude of the Fourier transform of the air-gap mmf over a period of 0.3 seconds. At each time step, $(0.005 seconds)$, a fft was taken.

From the figure 3.6 the magnitude of the 5th and 7th harmonics and the fundamental appear to change over time while the 11th and 13th harmonics do not change over time.
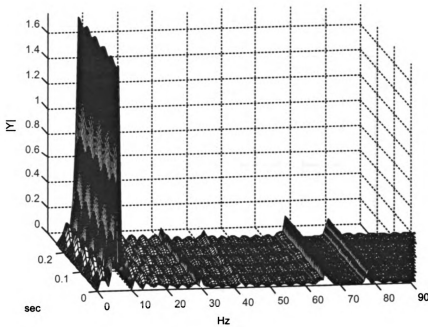
Figure 3.6: 3-D Fourier transform with respect to time and stator position

3.2.2 3phase-4pole Configuration

As mentioned previously, the 3-phase/4-pole configuration is not practical due to current im-
balances. However, a winding analysis is performed in order to compare the results to the
9-phase/4-pole configuration. The winding configuration is shown in figure 3.7.
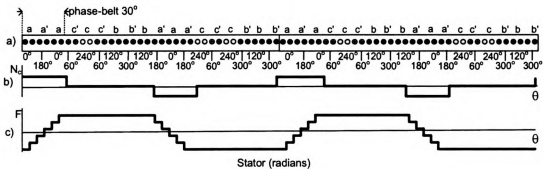
Figure 3.7: a) Coils arrangement, b) winding density $n(\theta)$ and c) resulting mmf $F(\theta)$

As shown, the phase belt for this coil arrangement is 30°.

Fourier Series analysis of the winding density and the stator air-gap mmf for the 3-phase/4-

pole configuration were conducted.

The results of the winding distribution is shown in figure 3.8.
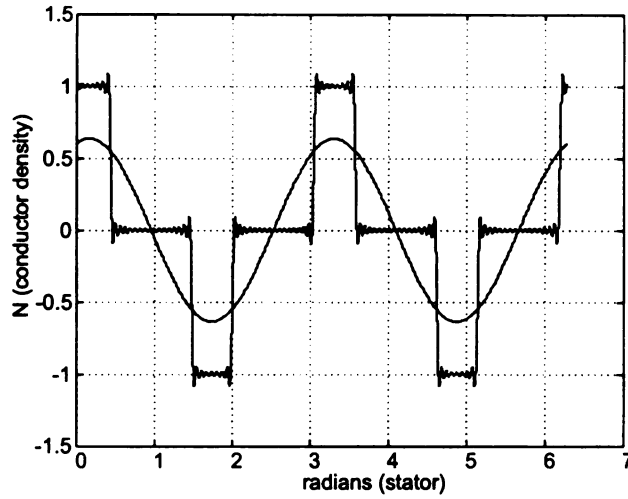
Figure 3.8: The Fourier Series Approx ($k = 1, 100$) of the winding density

The Fourier series for the air-gap mmf is shown in figure 3.9
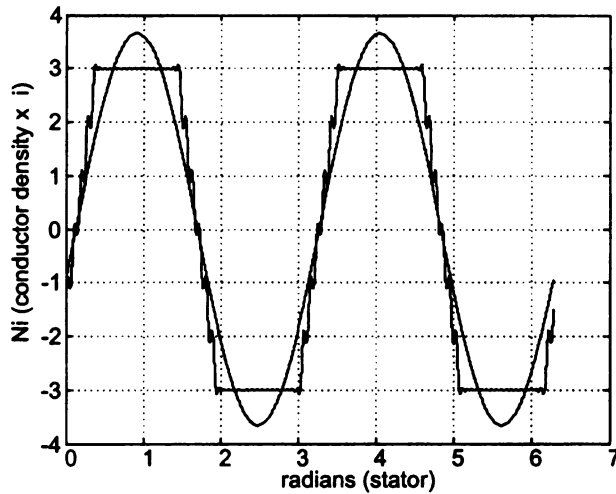
Figure 3.9: The Fourier Series Approx ($k = 1, 100$) of the air-gap mmf

The same sinusoidal currents applied to the 3-phase/12-pole configuration are applied to the three phase windings of the 3-phase/4-pole configuration. Likewise, the result is a sinusoidal stator air-gap mmf. Figure 3.10 shows the Fourier series approximation ($k = 100$) of

33

the air-gap mmf at one instance of time. In addition the a Fourier transform is applied to the wave form.
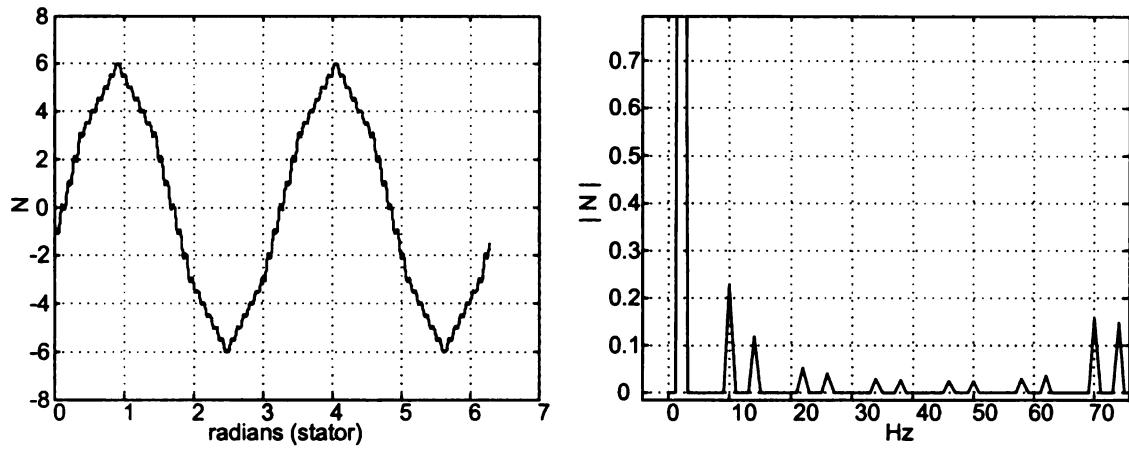
Figure 3.10: a)Instantaneous air-gap mmf and b) resulting Fourier Transform

From the fourier transform plot, figure 3.10, the fundamental is at 2 hz or 2 cycles per one diameter of the stator. There are twelve other frequency components at $[10, 14, 22, 26, 34, 38, 46, 50, 58, 62, 66, 70, 74Hz]$. The predominant harmonics are 10, 14, 70 and 74 which correspond to the $5^{th}, 7^{th}, 35^{th}$ and 37th harmonic. For this instant of time, the THD for the air-gap mmf is approximately 15%.

Figure 3.11 is the Fourier transform of the stator air-gap mmf period with respect to stator position and time. At each time step $(0.005 seconds)$ a transform was taken. The applied current was again $f = 10Hz$.

As with the 3-phase/12-pole configuration of the previous section, the magnitude of the 5th and 7th harmonics and the fundamental appear to change over time. In this case ,the 35th and 37th harmonics do not change over time.

34
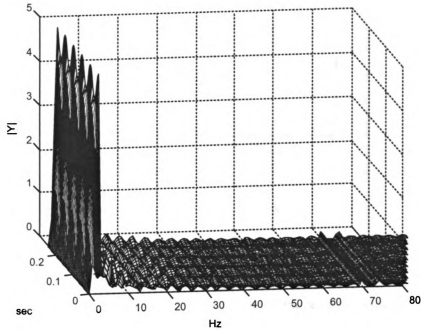
Figure 3.11: 3-D Fourier Transform with respect to time and stator position

3.2.3 9-phase 4-pole Configuration

The 9-phase/4-pole configuration was intended to produce relatively high speeds for power generation. For this configuration, the nine windings of the machine form a star connection. This arrangement results in a phase belt of 10°, as shown in figure 3.12.
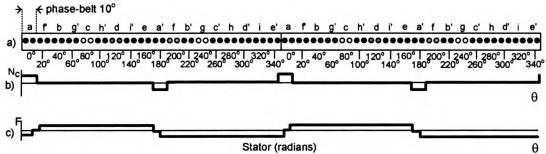
Figure 3.12: a) Coils arrangement, b) winding density $n(\theta)$ and c) resulting mmf $F(\theta)$

Again, Fourier series analysis of the winding density and the stator air-gap mmf for the 9-phase/4-pole configuration were conducted.

The Fourier series approximation, figure 3.13, shows one of nine winding distributions for

35

the 9-phase/4-pole configuration for $k = 1, 100$.
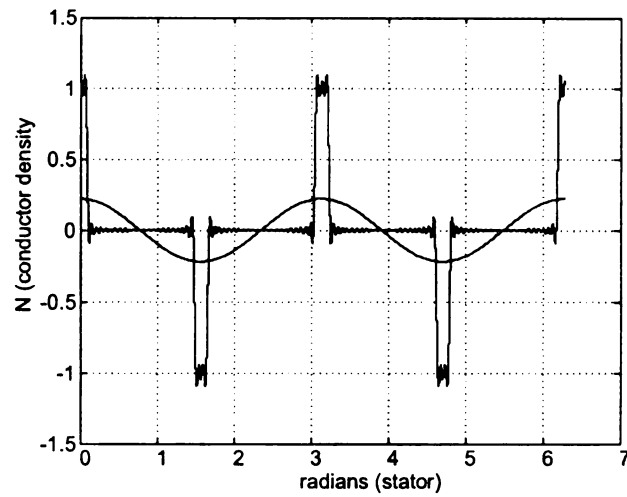
Figure 3.13: Fourier Series $(k = 1, 100)$ of the winding density

Next, the Fourier series for the stator air-gap mmf is determined.

Figure 3.14 shows the single phase stator mmf if $I_x(t) = 1$. The figure show two plots, one is the fundamental, $k = 1$, and the other is the Fourier series approximation with $k = 100$.
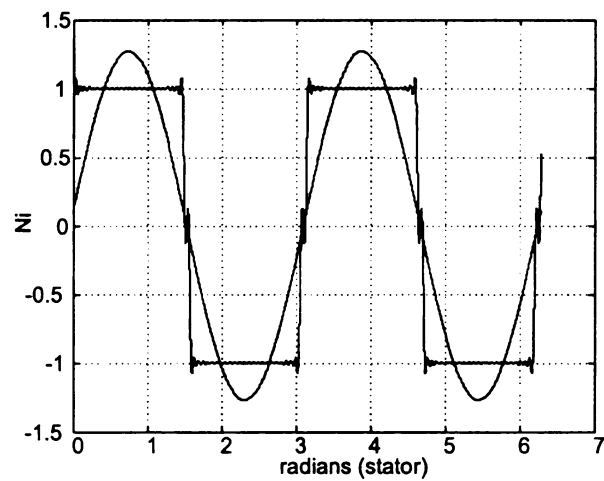
Figure 3.14: Fourier Series $(k = 100)$ of the air-gap mmf 9phase-4pole

In the case of the 9-phase/4-pole configuration, nine sinusoidal currents, $40°$ apart are

36

applied for steady state analysis.

$$I_a(t) = \sin(2\pi ft) \quad I_b(t) = \sin(2\pi ft + \tfrac{2\pi}{9}) \quad I_c(t) = \sin(2\pi ft + \tfrac{4\pi}{9})$$
$$I_d(t) = \sin(2\pi ft) + \tfrac{6\pi}{9} \quad I_e(t) = \sin(2\pi ft) + \tfrac{8\pi}{9} \quad I_f(t) = \sin(2\pi ft) + \tfrac{10\pi}{9})$$
$$I_g(t) = \sin(2\pi ft) + \tfrac{12\pi}{9}) \quad I_h(t) = \sin(2\pi ft) + \tfrac{14\pi}{9}) \quad I_i(t) = \sin(2\pi ft) + \tfrac{16\pi}{9})$$

For analysis purposes, the frequency of the applied current is $10Hz$. Figure 3.15 shows the Fourier series approximation ($k = 100$) of the stator air-gap mmf at one instance of time. In addition, a Fourier transform is applied to the wave form.
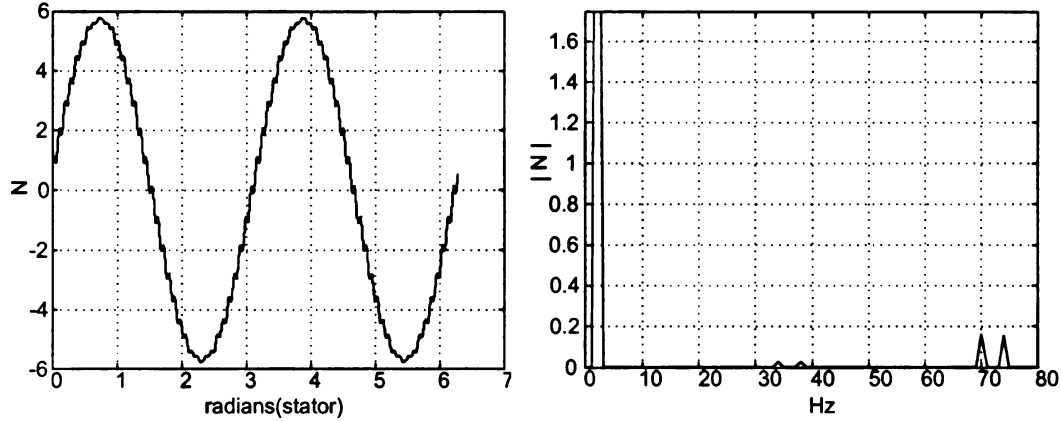
Figure 3.15: a)Instantaneous Stator Air-Gap MMF and b) Fourier Transform

From the Fourier transform, figure 3.15, the fundamental is 2 cycles per one diameter of the stator, a 4-pole motor. There are four other frequency components at 34,38,70,74 Hz, corresponding to the $17^{th}, 19^{th}, 35^{th}$ and 37th harmonics. For this instant of time, the THD for the air-gap mmf is approximately 6.2%.

Figure 3.16 is the Fourier transform of the air-gap mmf period with respect to stator position and time. Again, at each time step ($0.005 seconds$) a transform was taken. The applied current was again $f = 10Hz$.

In the case of the 9-phase/4-pole configuration there are no 5th and 7th harmonics, instead the 17th and 19th. Again the 35th and 37th harmonics do not change over time.

37
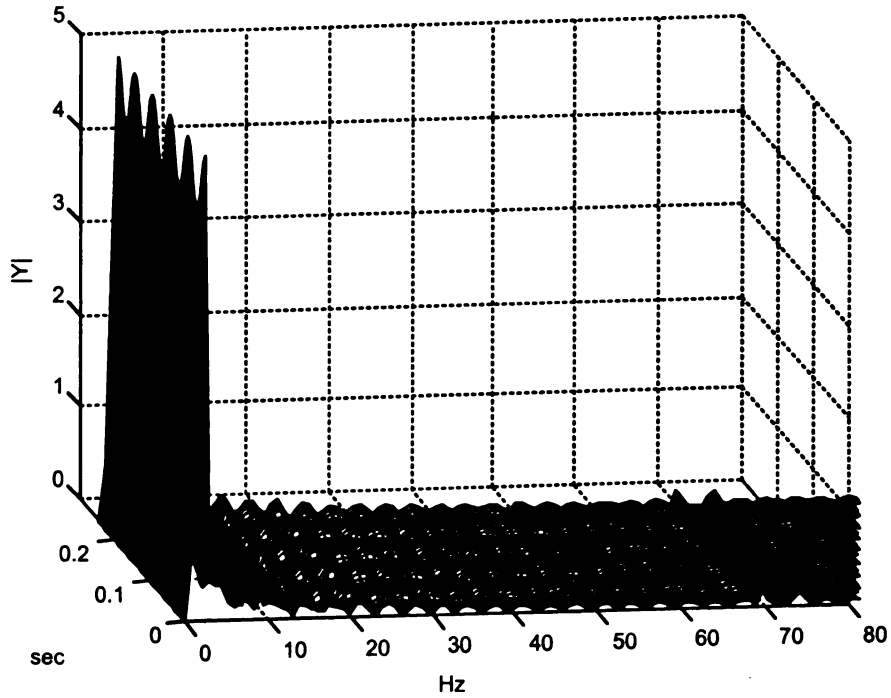
Figure 3.16: 3-D FFT of the 9-phase/4-pole configuration

3.2.4 Comparison Between the 3 configurations

Figure 3.17 is a comparison of the fundamental stator air-gap mmf of all three winding configurations.

The peak values of all three mmf are:

$$\max(MMF_{K=1} = 1.844Ni)_{3phase-12pole} \tag{3.2}$$

$$\max(MMF_{K=1} = 5.48Ni)_{3phase-4pole} \tag{3.3}$$

$$\max(MMF_{k=1} = 5.71Ni)_{9phase-4pole} \tag{3.4}$$

The highest value for stator air-gap mmf results from the 9-phase/4-pole configuration due to its low harmonic distortion [10]. The advantages of using nine phases instead of three phases are 1) balanced bemf, 2) lower harmonic distortion resulting in greater stator mmf. The 3phase-12pole stator mmf is approximately 3.09 times less than the 9phase-4pole configuration.

38
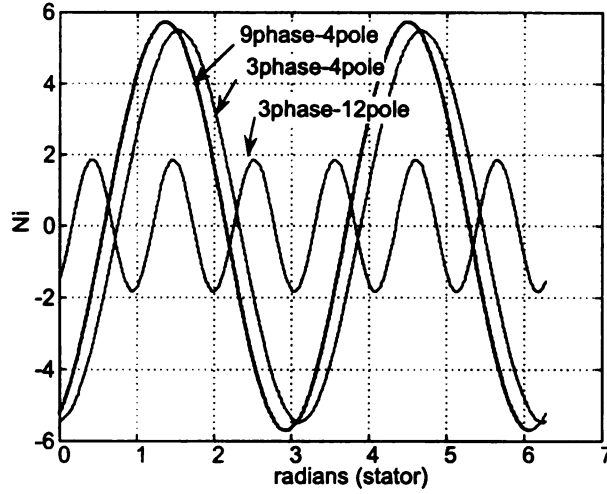
Figure 3.17: Comparison of the fundamental air-gap mmf

3.3 Steady State Model Development

In this section the motor parameters of the 3-phase/12-pole and 9-phase/4-pole configurations are determined. First, the parameters are determined experimentally. No-load and locked rotor tests are performed. Next, the parameters are calculated based on the dimensions of the stator and the rotor.

3.3.1 Equivalent Rotor Circuit of an Induction Motor

The voltage induced in the rotor bars of an induction motor depends on the relative speed between the stator and the rotor magnetic field.

$$\nu_{induced} = \left(\overline{v} \times \overline{B} \right) \cdot \ell \tag{3.5}$$

The relative velocity between the stator magnetic field and the rotor is $\overline{v}$. The stator magnetic field is $\overline{B}$ and ℓ is the length of the rotor bar.

The induced rotor voltage results in current, I_R, flowing in the rotor bars. Due to the reactance of the rotor, the current lags the peak induced voltage, as seen in figure 3.18.

From figure 3.18, the induced rotor current produces the rotor magnetic field $\overline{B_R}$. The sum of the rotor and stator magnetic field in the air-gap is the net magnetic field $\overline{B_{net}}$. The resulting

39
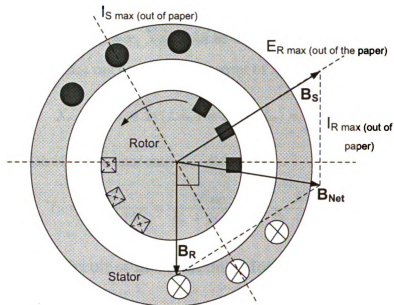
Figure 3.18: Stator and Rotor Magnetic Fields

torque is from the interaction between the stator and rotor magnetic fields.

$$\tau_{induced} = (k\overline{B_R} \times \overline{B_S}) \tag{3.6}$$

The greater the relative velocity, $\overline{v}$, the greater the induced voltage and current, and rotor magnetic field. The relative velocity is at maximum when the rotor is not turning and is at minimum when the rotor is spinning at the same velocity as the stator magnetic field. The difference between rotor speed, ω_R, and synchronous speed, ω_{sync}, is called the *slip speed*. Slip, s, is defined as:

$$s = \frac{\omega_{sync} - \omega_R}{\omega_{sync}} \times 100 \tag{3.7}$$

The locked-rotor voltage, E_{RO}, is the maximum possible induced voltage for a given applied stator voltage. When the slip is not one, the induced rotor voltage is determined as follows:

$$E_R = sE_{RO} \tag{3.8}$$

The frequency of the rotor voltage and current, f_r, is proportional to the stator voltage frequency, f_s, by slip.

$$f_r = sf_s \tag{3.9}$$

40

Therefore, at unity slip the rotor frequency is the same as the stator electrical frequency. At locked-rotor condition the reactance, X_{RO}, will be a function of stator frequency. For any other slip, the rotor reactance can be expressed in terms of X_{RO} by the slip:

$$X_r = \omega_r L_r = 2\pi(f_r L_r) = 2\pi s(f_s L_r) = sX_{RO} \tag{3.10}$$

With a rotor resistance of R_r the rotor current is defined as:

$$I_R = \frac{E_R}{R_r + jX_r} = \frac{sE_{RO}}{R_r + jsX_{RO}} = \frac{E_{RO}}{\frac{R_r}{s} + jX_{RO}} \tag{3.11}$$

3.3.2 Equivalent Circuit of an Induction Motor

In order to complete the per-phase equivalent circuit, the rotor impedances and current stator equivalent terms must be determined. Similar to a transformer's turn ratio, the effective turns ratio is used to reflect the rotor parameters to the stator equivalent circuit. Let α_{ff} be the effective turns ratio between the stator and rotor. Therefore the reflected rotor voltage, current, resistance and reactance are as follows:

$$I_2 = \frac{I_R}{\alpha_{ff}} \tag{3.12}$$

$$E_1 = \alpha_{ff} E_{RO} \tag{3.13}$$

$$R_2 = \alpha_{ff}^2 R_R \tag{3.14}$$

$$X_2 = \alpha_{ff}^2 X_{RO} \tag{3.15}$$

Figure 3.19 shows the per-phase equivalent circuit of an induction motor with rotor parameters referred to the stator side.

From figure 3.19 the magnetization current ,I_m, is the current required to produce the air-gap flux. The R_c terms represent core resistance from both stator and rotor. However, stator core losses are far greater than rotor losses. This is because the induction machine is operated close to synchronous speed, resulting in low relative motions between magnetic fields.

The magnetization reactance along with the other motor parameters can be estimated by performing several tests. These tests are the DC Test, the No-load Test and the Locked-Rotor
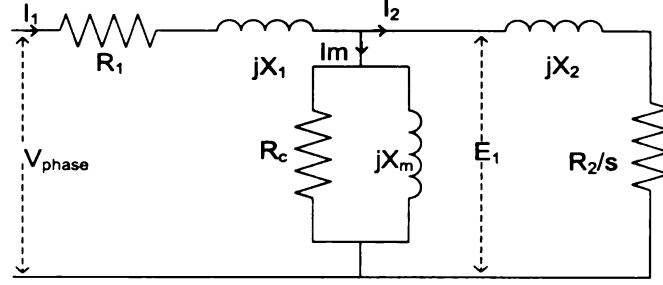
Figure 3.19: Per Phase Equivalent Model

Test. The DC Test measures the resistance of the stator winding. With applied DC voltage there is no induced voltage in the rotor and all reactances are zero. The only voltage drop is the copper resistance, R_1, of the stator winding.

The magnetizing reactance, X_m, is estimated from the the No-Load Test. The induction motor is operated very close to zero slip for the No-Load Test. For the actual experiment, a dynamometer was used to turn the motor at synchronous speed. Therefore, losses from windage and friction could be neglected. At zero slip R_2/s becomes infinitely large, resulting in the load current being zero. The input power is consumed in the core losses, R_c, and in maintaining the air-gap flux. The resulting equivalent circuit is shown in figure 3.20.
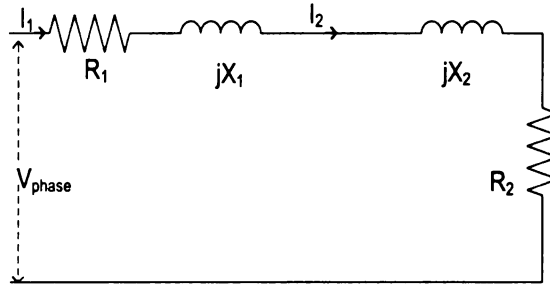
Figure 3.20: No-Load Equivalent Model

The magnetization current is very high in an induction machine compared to a transformer, due to the high reluctance of the air gap. Only a small amount of the total current passes through the R_c branch. Therefore $I_m \approx I_1$ and input impedance is

$$|Z_{NL}| = \frac{V_{phase}}{I_1} \approx \frac{V_{phase}}{I_m} = X_1 + X_m \tag{3.16}$$

42

For the locked-Rotor test the motor is energized (full-load current) with the rotor locked in place,s=1. Recall unity slip means that the relative motion between the stator magnetic field and rotor conductors is at maximum. Therefore, for a given stator voltage the maximum amount of voltage and current is induced in the rotor. Since there is no conversion from electric to mechanical power R_2/s reduces to R_2, rotor resistive losses. The rotor impedance, $jX_2 + R_2$, is very small compared to the magnetization reactance and core losses. Therefore, most of the input current passes through $jX_2 + R_2$ and the equivalent circuit of figure 3.19 reduces to the circuit of figure 3.21.
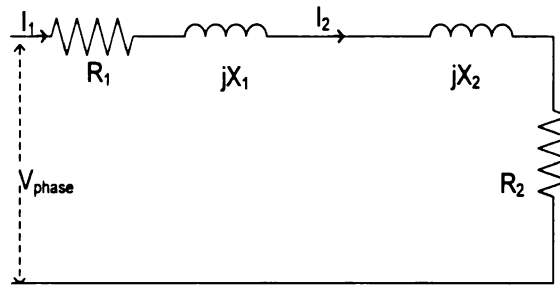
Figure 3.21: Locked-Rotor Equivalent Model

From figure 3.21, the total impedance of lock-rotor circuit is

$$|Z_{LR}| = \frac{V_{phase}}{I_1} = (R_1 + R_2) + j(X_1 + X_2) \qquad (3.17)$$

By measuring the phase voltage, the phase current and the power factor, $cos(\phi)$ the equivalent impedance can be determined. The resistance of the circuit is

$$|Z_{LR}|cos(\phi) = (R_1 + R_2) \qquad (3.18)$$

The stator resistance R_1 is determined from the DC Test. Therefore

$$R_2 = |Z_{LR}|cos(\phi) - R_1 \qquad (3.19)$$

The combined stator and rotor reactance is

$$|Z_{LR}|sin(\phi) = (X_1 + X_2) \qquad (3.20)$$

Distinguishing between the rotor and stator reactance is not straightforward. Typically, the values assigned to the rotor and stator reactance are based on design.

43

3.3.3 Equivalent Circuit Per-Phase Parameters

The DC, No-load and Lock-Rotor tests were conducted for both configurations; 4-pole/9-phase and 12-pole/3-phase.
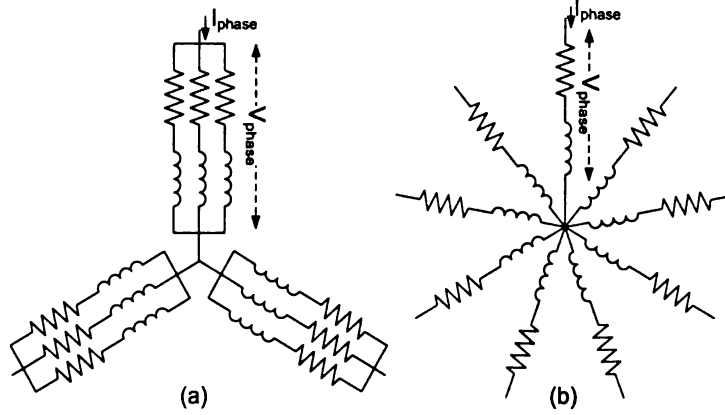
Figure 3.22: The phase voltage and current: (a) 12pole-3phase (b) ... 4pole-9phase

Figure 3.22 shows the phase voltage and current for both configurations. From the DC Test, stator resistances for the 4-pole/9-phase configuration is 0.2067Ω. For the 12-pole/3-phase configuration the per-phase stator resistance is 0.069Ω.

The dynamometer drove the motor to synchronous speed. The stator voltage was adjusted and recorded as was the phase current. Figure 3.23 is the resulting magnetization curve for the 4-pole/9-phase configuration.

Saturation appears to begin at 40 Vp_{rms} with a phase current of 2.6 amps. Due to the dynamometer driving the motor there should be no friction, windage or rotor losses. The only resistive lost will be from the stator windings, which is less than 1.5 watts and can be considered negligible. Thus, the impedance is mostly reactive.

$$|Z_{eq}| = \frac{40V_{rms}}{2.6A_{rms}} \approx \frac{V_{phase}}{I_m} = X_1 + X_m = 15.4\Omega \qquad (3.21)$$

Also plotted in figure 3.23 is the per-phase input power. These measurements were taken with the motor decoupled from the dynamometer in order to get an idea of mechanical losses. The real power at the knee of the magnetization curve is approximately 40 watts. This is due to friction, windage and rotor losses.
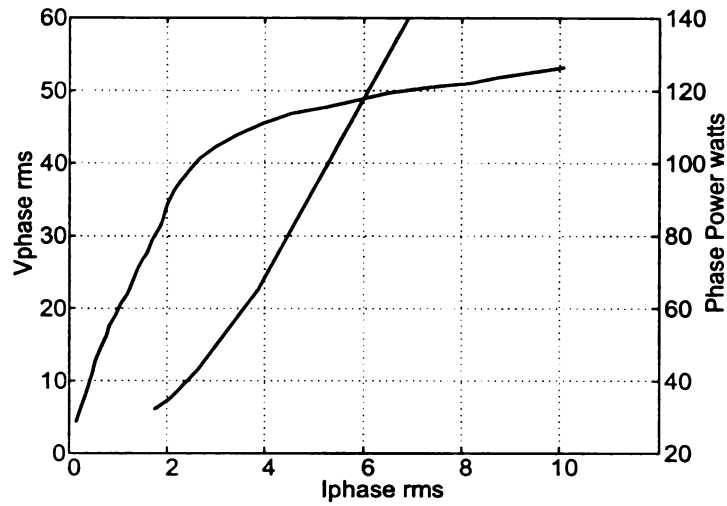
Figure 3.23: The Magnetization Curve for the 4pole-9phase Motor

Next the motor was reconfigured for 12-pole/3-phase operation and the No-Load Test was performed. Figure 3.24 shows the magnetization curve.
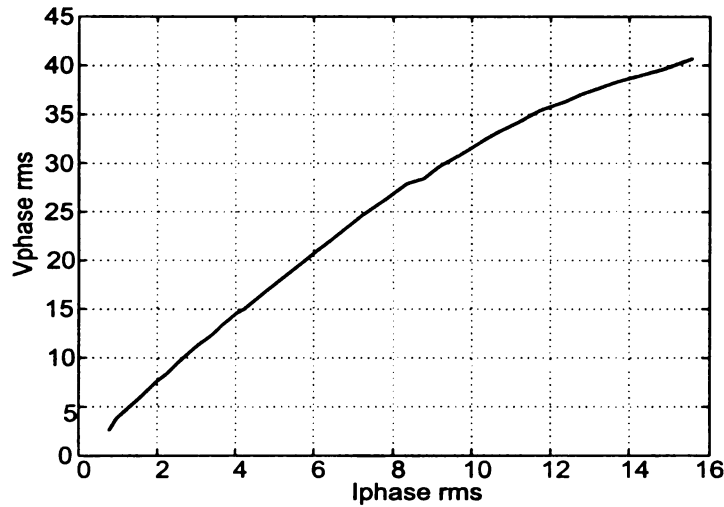
Figure 3.24: The Magnetization Curve for the 12pole-3phase Motor

Saturation appears to begin at 26.8 Vp_{rms} which corresponds to a phase current of 7.8 *amps*. The phase magnetization current for the 12-pole/3-phase configuration is approximately three times the magnetization current of the 4-pole/9-phase motor. Again, there should be no friction, windage or rotor losses due to the dynamometer. The only resistive lost will be from the stator windings which is less than 4.2 watts and can be considered negligible. The

45

Phase Power W	100	120	140	160	180	200
V_{phase}	12.40	13.45	14.22	14.80	15.27	15.80
I_{phase}	13.40	15.20	17.00	18.70	20.10	22.00
$|Z_{LR}|$	0.92	0.88	0.84	0.79	0.76	0.72
PF	0.60	0.59	0.58	0.58	0.59	0.57
$R_1 + R_2$	0.56	0.52	0.48	0.46	0.44	0.41
$(X_1 + X_2)(60/15Hz)$	3.01	2.96	2.86	2.73	2.58	2.46
$(L_1 + L_2)mH(60Hz)$	7.8	7.6	7.2	6.9	6.5	6.2
S_{power}	166.16	204.44	241.74	276.76	306.93	347.60
$S_{power}x9$	1495	1840	2176	2491	2762	3128

Table 3.1: Locked-Rotor Test 4-pole/9-phase

total reactive impedance is:

$$|Z_{eq}| = \frac{26.8V_{rms}}{7.8A_{rms}} \approx \frac{V_{phase}}{I_m} = X_1 + X_m = 3.4\Omega \tag{3.22}$$

The total reactance of the 12-pole/3-phase is 4.5 times less the total impedance of the 4pole-9phase configuration.

Next, the Locked-Rotor Test is performed on both motor configurations. For the Lock-Rotor Test the applied stator voltage frequency was $15Hz$. At unity slip, the rotor electrical frequency is the same as the stator electrical frequency. However at the normal operating point rotor speed is near synchronous speed, thus, the the rotor electrical frequency is very low compared the the stator electrical frequency. As a compromise, the applied stator voltage frequency is set to 25% of the normal operating frequency. For the 4-pole/9-phase motor configuration the following data was measured and calculated:

Since the stator copper resistance was determined from the DC Test, the load resistance R_2 can be calculated. To determined the stator and rotor reactance some assumptions have to be made. The motor was originally designed for high starting torques in order to start a conventional internal combustion engine. Also, the motor has relatively many rotor bars, 78. These characteristics are similar to the NEMA design class D induction motor. The rule of thumb for design class D motors is the leakage reactance is evenly split between the rotor and stator.

46

The last thing to determine is the Full-load current. For the Locked-Rotor test several full-load currents were used. The following data was measured and calculated.

Phase Power W	80	100	120	140	160	180
V_{phase}	7.18	7.70	8.67	9.37	9.90	10.40
I_{phase}	16.00	17.20	19.20	20.50	21.00	22.00
$|Z_{LR}|$	0.45	0.45	0.45	0.46	0.47	0.47
PF	0.70	0.75	0.72	0.73	0.77	0.79
$R_1 + R_2$	0.31	0.34	0.32	0.33	0.36	0.37
$X_1 + X_2(60/15Hz)$	1.29	1.17	1.25	1.25	1.20	1.17
$(L_1 + L_2)mH(@60Hz)$	3.4	3.1	3.3	3.3	3.2	3.1
$S_{power}x3$	344.64	397.32	499.39	576.25	623.70	686.40
$S_{power}x9$	1034	1192	1498	1729	1871	2059

Table 3.2: Locked-Rotor Test 12-pole/3-phase

Figure 3.25 shows the measured total power and real power from the Lock-Rotor test on the 12-pole/3-phase motor.
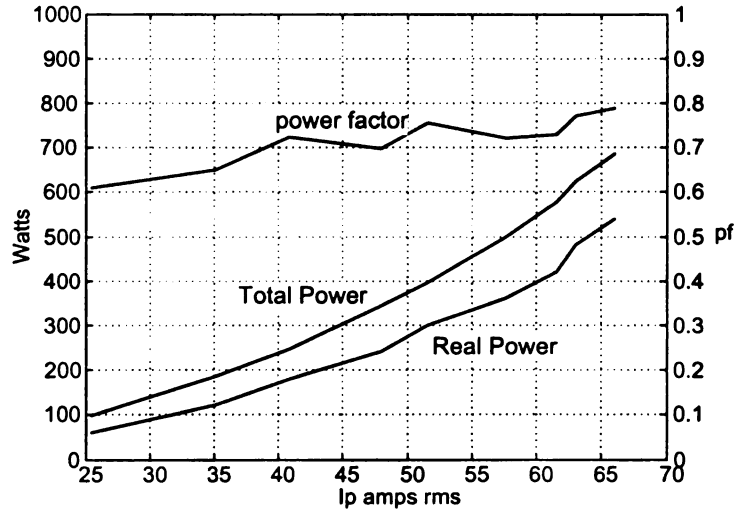
Figure 3.25: Total, Real Power and pf from Locked-Rotor 12pole-3phase

The Lock-Rotor parameters were chosen at approximately 1.2kW input power. The measured motor parameters for both the 4pole-9phase and 12pole-9phase configurations are tabulated below:

Parameters	R_1	R_2	X_m	X_1	X_2
$4pole - 9phase$	207m Ω	380m Ω	15.0Ω	375mΩ	375mΩ
$12pole - 3phase$	69m Ω	44m Ω	3.4Ω	195mΩ	195mΩ

Table 3.3: Measured Parameters

3.3.4 Calculated Parameters

In the previous section, the per-phase parameters were determined experimentally. Those values will be compared to the analytically derived parameter values in this section. The following values were determined; R_s, R_r, L_r, L_s and L_m.

For the induction motor, the following leakage reactances are analytically derived: rotor and stator slot reactance, stator end-turn reactance, rotor ring reactance, zig-zag reactance and belt reactance. (The rotor bars of the induction motor are unskewed.) Figure 3.26 shows the slot, rotor ring and end-turn flux leakage of the induction motor.
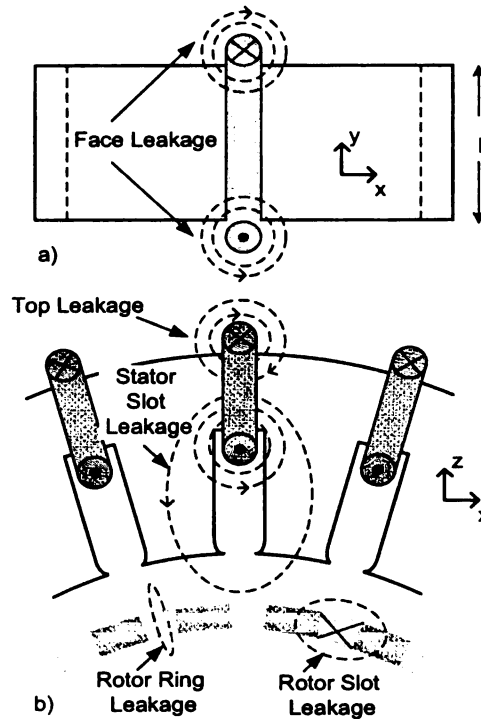
Figure 3.26: Slot and End-turn Flux Leakage

Stator slot flux leakage is that flux that does not link with the rotor. This flux only links

48

with conductors that produced it. Figure 3.27 show the dimensions a induction motor stator and rotor slots. The stator slot has a trapezoidal shape; however, to simplify integration we will assume that the stator slot is rectangular. Let C be the total number of conductors in the stator slot.
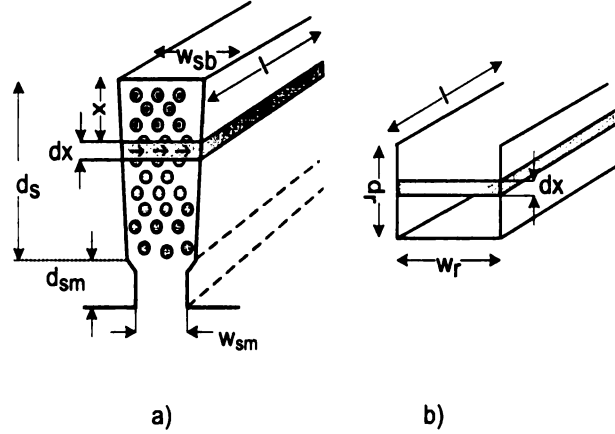
Figure 3.27: Slot Geometry a) stator slot b) rotor slot

From figure 3.27, the magnetic field intensity across the stator slot is:

$$\oint H \bullet dl = H w_{bs} = Ci \tag{3.23}$$

The magnetic density in the cross section of $dx \cdot l$ is

$$B = \mu_o H = \mu_o \frac{Ci}{w_{bs}} \tag{3.24}$$

The differential flux is

$$d\Phi = B(l)(dx) = \mu_o H(l)(dx) = \mu_o \frac{Ci}{w_{bs}}(l_{stack})(dx) \tag{3.25}$$

This differential flux is generated by $C(x/ds)$ number of conductors. The same conductors are linked by the differential flux. The differential inductance is

$$dL = \frac{C(x/ds)d\Phi}{i} \tag{3.26}$$

The inductance is

$$L_{stator slot} = \int_0^{ds} \mu_o l_{stack}(C\frac{x}{d_s})^2 \frac{dx}{w_{sb}} = \mu_o l_{stack} C^2 (\frac{d_s}{3w_{bs}}) \tag{3.27}$$

49

Including the mouth of the slot the stator slot inductance is

$$L_{stator slot} = \mu_o l_{stack} C^2 (\frac{d_s}{3w_{bs}} + \frac{d_{sm}}{w_{sm}})$$ (3.28)

The total stator slot inductance is determined by the total number of slots, N_{stator}, multiplied by the slot inductance of equation 3.28. Since the phase coils are in series for both the 12-pole/3-phase and 4-pole/9-phase configurations of the induction motor the per-phase inductance can be found by multiplying equation 3.28 by N_{stator}/m, where m is the number of phases.

$$L_{per-phase-stator-slot} = \frac{N_{stator}}{m} \mu_o l_{stack} C^2 (\frac{d_s}{3w_{bs}} + \frac{d_{sm}}{w_{sm}})$$ (3.29)

The rotor slot inductance was similarly derived, with $C = 1$ and N_{rotor} being the number of rotor slots.

$$L_{per-phase-rotor-slot} = \frac{N_{rotor}}{m} \mu_{al} l_{stack} \frac{d_r}{w_r}$$ (3.30)

Since the induction motor is cordially wound the the end-turn reactance has several components. From figure 3.26 the total end-turn reactance of the stator is:

$$X_{ET} = X_{top} + 2X_{face}$$ (3.31)

The top flux leakage, X_{top}, is generated by the opposite side of the conductors in the stator slots. Most of the flux path is through air as shown in figure 3.28. (However, not shown in figure 3.28 is the stator housing which is made of aluminum.) Unlike the conductors in the slots, the outer-stator conductors are contained in a defined space. Instead of taking the form of the stator slot, these unconstrained conductors form a half cylindrical bundle. The total flux leakage from these conductors can be divided into two components, leakage inside the conductor bundle and leakage outside the bundle

$$\Phi_{top} = \Phi_{insidebundle} + \Phi_{outside_bundle}$$ (3.32)

From Ampere's law the magnetic field inside the conductor bundle is:

$$\oint H \bullet dl = H\pi r = Ni = (C(\frac{r^2}{t^2}))i$$ (3.33)
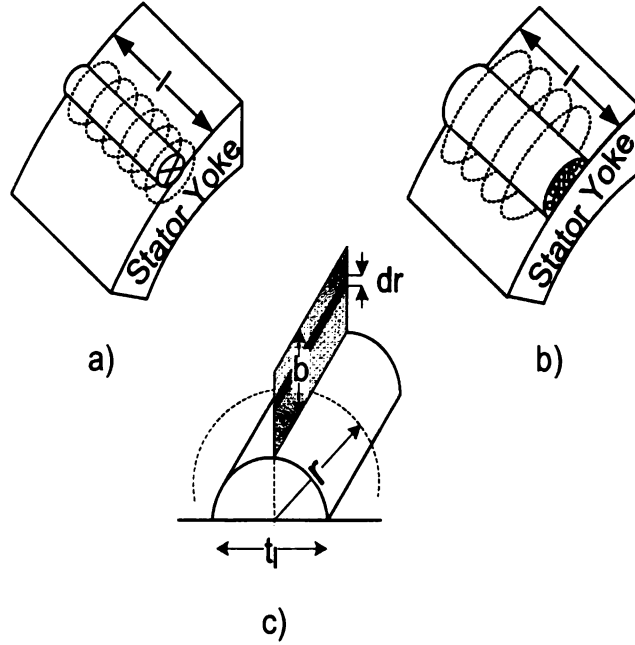
Figure 3.28: Stator Top Flux Leakage a) Single Conductor b) Conductor Bundle model c) Dimension of actual conductor bundle

The total number of conductors across the top is C and $C(r^2/t^2)$ is the proportional number of conductors below dr. The differential flux is

$$d\Phi = B(l)(dr) = \frac{\mu_o iCr}{\pi t^2}(l_{stack})(dr) \tag{3.34}$$

This differential flux is generated by $C(r^2/t^2)$ number of conductors. The same conductors are linked by the differential flux. The differential inductance is

$$dL = \frac{C(r^2/t^2)d\Phi}{i} \tag{3.35}$$

$$L_{inside-bundle} = \int_0^t \frac{l_{stack}\mu_o C^2 r^3}{\pi t^4}dr = \frac{l_{stack}\mu_o C^2}{4\pi} \tag{3.36}$$

The inductance outside the conductor bundle is

$$L_{outside-bundle} = \frac{l_{stack}\mu_o C^2}{\pi}\ln(\frac{x}{t}) \tag{3.37}$$

The term x is chosen to be the outer limit of the magnetic field. In this case, the x is the distance to the edge of the housing. The total stator top leakage inductance is

51

$$L_{top} = \frac{l\mu_o C^2}{4\pi} + \frac{l_{stack}\mu_o C^2}{\pi}\ln\left(\frac{x}{t}\right) = \frac{l_{stack}\mu_o C^2}{\pi}[0.25 + \ln\left(\frac{x}{t}\right)] \tag{3.38}$$

The face leakage can be derived similar to the top leakage. Again assume the conductors form a half cylindrical bundle. The length of the bundle simply is the distance from the bottom of the stator to the outer edge of the stator. The bundle will have an outer and inner flux. The total inductances for both face leakages is:

$$L_{face} = 2\frac{l_{yoke}\mu_o C^2}{4\pi} + \frac{l_{yoke}\mu_o C^2}{\pi}\ln\left(\frac{x}{t}\right) = \frac{l_{stack}\mu_o C^2}{\pi}[0.25 + \ln\left(\frac{x}{t}\right)] \tag{3.39}$$

The final end-turn leakage is the rotor ring leakage. Figure 3.29 show the outer conductor ring of the squirrel cage. The flux leakage path is orthogonal to the mutual flux of the stator and rotor. The leakage flux will link the iron of the stator and create eddy currents in the stator stacks. The result is radial force on the motor. This force can become significant at low slip when the rotor current is high.
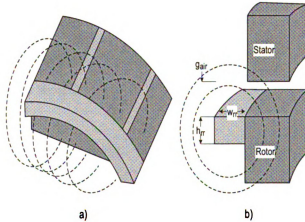
Figure 3.29: Rotor Ring a) Leakage Flux b) Dimension

For the derivation of the flux leakage, only the flux outside the ring will be considered. In order to simplify the calculations, the rectangular rotor ring is modeled as a cylindrical conductor. The magnetic field through the air is:

$$\oint H \bullet dl = H2\pi - 2w_{rr}Ci \tag{3.40}$$

The total flux, around the entire rotor, is:

$$Phi = \int_{wrr}^{x} BdA = \int_{wrr}^{x} B(2\pi R_{OD})dr = \int_{wrr}^{x} \frac{\mu o i 2\pi R_{OD}}{\pi r - 2w_{rr}}dr \qquad (3.41)$$

The total rotor ring inductance is:

$$L = \frac{N\Phi}{i} = 2\mu_o \pi R_{OD} \ln \frac{\pi r - 2w_{rr}}{w_{rr}} \qquad (3.42)$$

Air-gap Inductance

The air gap inductance of the induction motor is calculated assuming finite permeability in the stator and rotor. This is accomplished by dividing the the air gap inductance by the equivalent air gap length and a saturation factor term.

$$L_m = \frac{8(C_{pole}^2)A_g}{\pi P g_e(SF)} \qquad (3.43)$$

The saturation factor

$$SF = \frac{MMF_{air-gap} + MMF_{iron}}{MMF_{air-gap}} \qquad (3.44)$$

The total MMF_{iron} is the summation of the ampere-turns in the: stator yoke, stator teeth, rotor core, rotor teeth and air-gap. These five terms in series form the the magnetic circuit of the induction motor.

The first step in calculating saturation factor, SF, is to determine the flux density in all five components. The flux is calculated from the impressed phase voltages used in the previous section. The ampere-turns per length needed to induce the flux density in iron components is estimated from a-c magnetization curves provide by the steel industry. The estimated values of ampere-turns per meter are multiplied by the length of the iron components. The ampere-turns of each iron component is added together with the effective air-gap ampere-turns to get the total ampere-turns of the induction motor.

The effective air-gap is determined by multiplying the air-gap by an empirical approximation of the Carter coefficient.

$$K = \frac{\lambda(5g + w_{10})}{\lambda(5g + w_{10} - w_{10}^2)} \qquad (3.45)$$

Parameters	Measured	Calculated
L_m	39mH	23mH
$L_s + L_r$	2mH	1.2mH

Table 3.4: Measured versus Calculated Inductances for 4-pole/9-phase configuration

Parameters	Measured	Calculated
L_m	8.5mH	4.5mH
$L_s + L_r$	1mH	1.2mH

Table 3.5: Measured versus Calculated Inductances for 12-pole/3-phase configuration

The resulting air-gap inductance for the 3-phase/12-pole configuration is 4.5mH compared to the measured value of 8.5mH. For the 9-phase/4-pole configuration the calculated air-gap inductance is 23mH, compared to the measured value of 39mH.

CHAPTER 4

Coordinate Transformation

4.1 Introduction

In chapter 7 a novel scheme of controlling the pole-changing induction motor drive is introduced. This scheme is based on Rotor Flux Field Orientation Control (R-FOC). For conventional R-FOC, machine variables, i.e. current and voltages, are mapped between the symmetrical 3-phase coordinate system and the orthogonal rotor flux coordinate system using Park-Clark Transformation [13]. For electrically balanced systems the transforation between the symmetrical 3-phase and 2-phase system is unique. This transformation can be used when operating the induction machine as a 3-phase/12-pole motor. The objective of this chapter is to develop a coordinate transformation in order to implement R-FOC for 9-phase/4-pole operation.

Unlike, symmetrical 3-phase operation, there are an infinite number of coordinate transformations between an orthogonal system and a 9-phase symmetrical system. Therefore, a coordinate transformation is derived based on two requirements. The first requirement is that the commanded current realization in the nine stator windings, result in an equal distribution of phase current in all nine windings. This is to avoid saturation, minimize winding loses and equally distribute the thermal load.

The second requirement makes possible the pole-changing control scheme of chapter 7. The coordinate transformation has to decouple, from the nine stator windings, the measured

torque and flux producing currents,(i_{d12}, i_{q12}, i_{d4} and i_{q4}), of both the 3-phase/12-pole and 9-phase/4-pole motor when operated simultaneously. It will be shown that this can be accomplished measuring only four of the nine phase currents. This reduces the number of current sensors needed.

A brief review of the Park-Clark Coordinate transformation will be given. This is followed by a detailed development of the coordinate transformation between the 9-phase symmetrical system and the orthogonal system. Next the reduced coordinate transformation is introduced. Simulation results are presented which show the reduce coordinate transformation does determine the feedback currents (i_{d12}, i_{q12}, i_{d4} and i_{q4}) from only four measured phase currents.

4.2   3-Phase 12-Pole: Park-Clark Coordinate Transformation

The rotor flux reference frame currents i_{q12}^* and i_{d12}^* commands are realized in the stator stationary reference frame using classic Park-Clark transformation [19],[1].

$$i_{s12} = \chi_{12}\beta_{12}i'_{dqs12} \tag{4.1}$$

where

$$\chi_{12} = \begin{bmatrix} \mathbf{Q}_{12} & \mathbf{0}_{3x2} & \mathbf{0}_{3x2} \\ \mathbf{0}_{3x2} & \mathbf{Q}_{12} & \mathbf{0}_{3x2} \\ \mathbf{0}_{3x2} & \mathbf{0}_{3x2} & \mathbf{Q}_{12} \end{bmatrix} \tag{4.2}$$

and

$$\mathbf{Q}_{12} = \begin{bmatrix} \cos(\theta_{12}) & \sin(\theta_{12}) \\ \cos(\theta_{12} + \frac{-2\pi}{3}) & \sin(\theta_{12} + \frac{2\pi}{3}) \\ \cos(\theta_{12} + \frac{2\pi}{3}) & \sin(\theta_{12} + \frac{-2\pi}{3}) \end{bmatrix} \tag{4.3}$$

and

$$\beta_{12} = \begin{bmatrix} 1 & 0 \\ 0 & 1 \\ 1 & 0 \\ 0 & 1 \\ 1 & 0 \\ 0 & 1 \end{bmatrix} \quad i_{dqr12} = \begin{bmatrix} i_{dr12} & i_{qr12} \end{bmatrix} \tag{4.4}$$

The rotor flux angle θ_{12} is estimated from the measured quadrature and direct currents $\{i_{q12}, i_{d12}\}$. These currents are estimated from the phase currents by the inverse Park-Clark coordinate transformation.

4.3   9-Phase 4-Pole: Coordinate Transformation

Unlike the 3-phase coordinate transform in the previous section, there is no unique transformation for realizing the commanded rotor flux reference frame currents i_{q4}^* and i_{d4}^* in the 9-phase winding reference frame. R-FOC requires the coordinate transformation to be invertible in order to map variables between the stationary and rotor flux reference frames. The rest of this section is dedicated to developing an invertible coordinate transformation. Several of the desired results of such a transformation are the minimization of winding loses and the equalization of current density over the stator. Ensuring that no winding carries more current than any other is important for several reasons. Greater current in one winding will result in greater localized thermal loading. Unbalanced thermal distribution will result in unbalanced winding resistance, R-FOC is sensitive to winding resistance. Another reason for equalized current distribution is the avoidance of flux saturation.

The development of the 9-phase coordinate transformation begins with the commanded torque and flux currents currents i_{q4}^* and i_{d4}^*, which are in the rotor flux-linkage reference frame. An optional intermediate step before being mapped into the 9-phase symmetrical reference frame, is the mapping of the commanded currents into the imaginary-real reference of the stator. However, since the transformation between to orthogonal coordinate systems is unique this step can be skipped. The coordinate transformation developed here will directly map the commanded currents in the rotor reference frame directly into the 9-phase symmetrical reference frame.
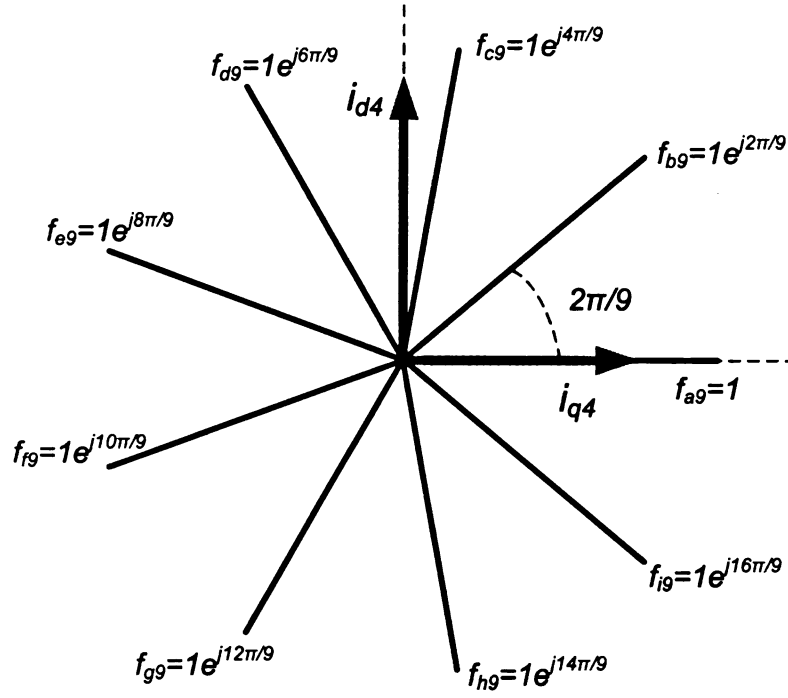
Figure 4.1: 9-phase symmetrical components

4.4 Development of Coordinate Transformation

Figure 4.1 shows the nine axes symmetrical reference frame and the orthogonal rotor reference frame with the commanded currents i_{d4}^* and i_{q4}^*. The nine axes symmetrical reference frame can be thought of as the sum of three symmetrical three-axes reference frames oriented 40 degrees with respect to each other. The commanded currents, can be divided into components and realized in the three reference frames. The components of the commanded currents are:

$$i(t)_{ds4} = i(t)_{ds4adg} + i(t)_{ds4beh} + i(t)_{ds4cfi} \tag{4.5}$$

$$i(t)_{qs4} = i(t)_{qs4adg} + i(t)_{qs4beh} + i(t)_{qs4cfi} \tag{4.6}$$

Figure 4.2 shows the six current components in the respective reference frame. Each of these commanded current components are then realized by the following transformations:

$$\begin{bmatrix} i_{s1} \\ i_{s4} \\ i_{s7} \end{bmatrix} = \mathbf{Q}_{4a} \begin{bmatrix} i_{ds4adg} \\ i_{qs4adg} \end{bmatrix} \quad \begin{bmatrix} i_{s2} \\ i_{s5} \\ i_{s8} \end{bmatrix} = \mathbf{Q}_{4b} \begin{bmatrix} i_{ds4beh} \\ i_{qs4beh} \end{bmatrix} \tag{4.7}$$

58
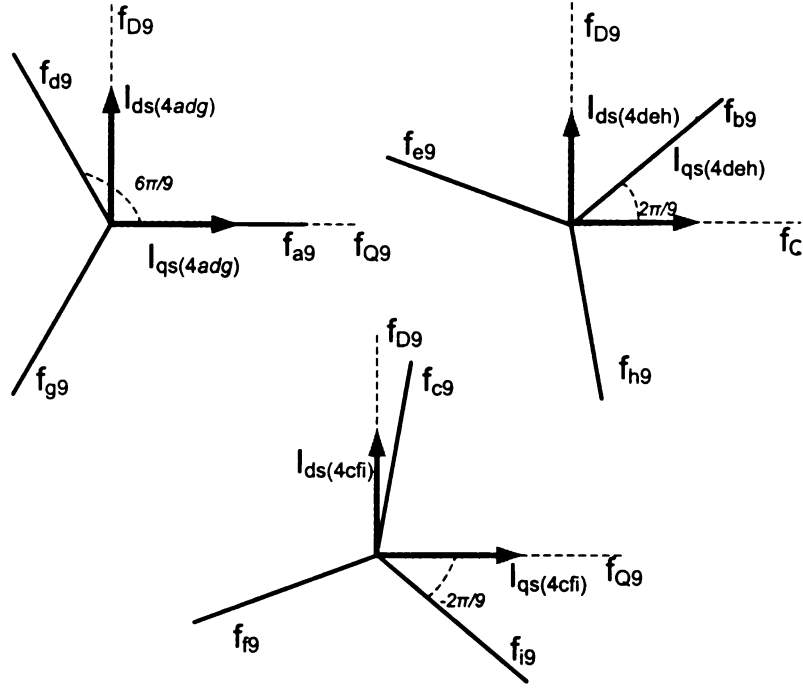
Figure 4.2: Three 3-phase axes reference frames with stationary currents

$$
\begin{bmatrix} i_{s9} \\ i_{s6} \\ i_{s3} \end{bmatrix} = \mathbf{Q}_{4c} \begin{bmatrix} i_{ds4ifc} \\ i_{qs4ifc} \end{bmatrix} \tag{4.8}
$$

where

$$
\mathbf{Q}_{4a} = \begin{bmatrix} \cos(\theta_4) & \sin(\theta_4) \\ \cos(\theta_4 + \frac{-2\pi}{3}) & \sin(\theta_4 + \frac{2\pi}{3}) \\ \cos(\theta_4 + \frac{2\pi}{3}) & \sin(\theta_4 + \frac{-2\pi}{3}) \end{bmatrix} \tag{4.9}
$$

$$
\mathbf{Q}_{4b} = \begin{bmatrix} \cos(\frac{\theta_4 - 2\pi}{9}) & \sin(\theta_4 - \frac{2\pi}{9}) \\ \cos(\theta_4 + \frac{-2\pi}{3} - \frac{2\pi}{9}) & \sin(\theta_4 - \frac{2\pi}{3} - \frac{2\pi}{9}) \\ \cos(\theta_4 + \frac{2\pi}{3} - \frac{2\pi}{9}) & \sin(\theta_4 + \frac{2\pi}{3} - \frac{2\pi}{9}) \end{bmatrix} \tag{4.10}
$$

$$
\mathbf{Q}_{4c} = \begin{bmatrix} \cos(\theta_4 + \frac{2\pi}{9}) & \sin(\theta_4 + \frac{2\pi}{9}) \\ \cos(\theta_4 + \frac{-2\pi}{3} + \frac{2\pi}{9}) & \sin(\theta_4 - \frac{2\pi}{3} + \frac{2\pi}{9}) \\ \cos(\theta_4 + \frac{2\pi}{3} + \frac{2\pi}{9}) & \sin(\theta_4 + \frac{2\pi}{3} + \frac{2\pi}{9}) \end{bmatrix} \tag{4.11}
$$

The overall transformation from the two commanded stationary, orthogonal currents $\{i_{d4}, i_{q4}\}$ into the nine axes reference frame is:

$$
i_{s4} = \chi_4 i_{dq4component} \tag{4.12}
$$

59

where

$$\chi = \begin{bmatrix} \mathbf{Q}_{4a} & \mathbf{0}_{3x2} & \mathbf{0}_{3x2} \\ \mathbf{0}_{3x2} & \mathbf{Q}_{4b} & \mathbf{0}_{3x2} \\ \mathbf{0}_{3x2} & \mathbf{0}_{3x2} & \mathbf{Q}_{4c} \end{bmatrix} \quad i_{dqs4} = \begin{bmatrix} i_{ds4adg} \\ i_{qs4adg} \\ i_{ds4beh} \\ i_{qs4beh} \\ i_{ds4ifc} \\ i_{qs4ifc} \end{bmatrix} \tag{4.13}$$

In equations (4.5) and (4.6) the currents $\{i_{ds4}, i_{qs4}\}$ were divided into components that were not necessarily equal. However a equal stator current distribution can be achieved if the components are divided equally.

$$i_{ds4} = \frac{1}{3}i_{ds4adg} = \frac{1}{3}i_{ds4beh} = \frac{1}{3}i_{ds4cfi} \tag{4.14}$$

$$i_{qs4} = \frac{1}{3}i_{qs4adg} = \frac{1}{3}i_{qs4beh} = \frac{1}{3}i_{qs4cfi} \tag{4.15}$$

Thus, $\{i_{dqs4}\}$ can be realized using only $\{i_{ds4adg}, i_{qs4adg}\}$. The nine phase realization of equation (4.12) becomes

$$i_{s4} = \chi_4 \beta_4 \left[i_{ds4adg} i_{qs4adg}\right]' \tag{4.16}$$

Where β_4 is

$$\beta_4 = \frac{1}{3} \begin{bmatrix} 1 & 0 \\ 0 & 1 \\ 1 & 0 \\ 0 & 1 \\ 1 & 0 \\ 0 & 1 \end{bmatrix} \tag{4.17}$$

Equal current distribution of the commanded currents results in least amount of stator winding loses.

4.5   Pole-Changing Transition 4-pole and 12-pole Operation

While operating in either 12-pole or 4-pole configuration, only the respective quadrature and direct currents are needed for R-FOC. However, during the pole-changing transition, both sets of currents, $\{i_{dqs4}\}$ and $\{i_{dqs12}\}$, must be realized and extracted from the stator windings.

4.5.1 Simultaneous Realization of i_{dqs4} and i_{dqs12}

The commanded currents of the both the 12-pole and 4-pole motors are simultaneously realized by summing (4.1) and (4.16)

$$i_S = i_{s12} + i_{s4} = \chi_{12}\beta_{12}i'_{dqs12} + \chi_4\beta_4\left[i_{ds4adg}i_{qs4adg}\right]' \tag{4.18}$$

where i_s are the nine stator winding currents.

4.5.2 Simultaneous Extraction of i_{dqs4} and i_{dqs12}

The extraction of $\{i_{dqs4}\}$ and $\{i_{dqs12}\}$ from the measured stator windings is not as straightforward as the stator realization of those currents. Expanding the left side of equation (4.18):

$$\begin{aligned}
i_{S1} &= i_{s12a} + i_{s4a} & i_{S4} &= i_{s12a} + i_{s4d} & i_{S7} &= i_{s12a} + i_{s4g} \\
i_{S2} &= i_{s12a} + i_{s4b} & i_{S5} &= i_{s12b} + i_{s4e} & i_{S8} &= i_{s12b} + i_{s4h} \\
i_{S3} &= i_{s12a} + i_{s4c} & i_{S6} &= i_{s12c} + i_{s4f} & i_{S9} &= i_{s12c} + i_{s4i}
\end{aligned} \tag{4.19}$$

the nine stator windings are dependent on twelve motor currents. These results in equation (4.18) being non-invertible. However, $\{i_{dqs4}\}$ and $\{i_{dqs12}\}$ can still be obtained from the stator currents by rearranging equation (4.18).

From equation (4.19) define i_s as

$$i_S = [\zeta][i_{combined}] \tag{4.20}$$

where $i_{combined}$ is the realized stator currents of both the 4pole-9phase and 12pole-3phase motors

$$i_{combined} = [\{i_{s4a}, i_{s4b}, ...s4i\}, \{i_{s12a}, i_{s12b}, i_{s12c}\}]' \tag{4.21}$$

and with [I] being the identity matrix

$$\zeta = \begin{bmatrix} & \mathbf{I}_{3x3} \\ \mathbf{I}_{9x9} & \mathbf{I}_{3x3} \\ & \mathbf{I}_{3x3} \end{bmatrix} \tag{4.22}$$

Therefore the stationary nine axes realization of commanded stator currents for both machines operating simultaneously is:

$$i_S = \chi_{combined}\beta_{combined}\left[i_{ds4}i_{qs4}i_{ds12}i_{qs12}\right]' \tag{4.23}$$

61

where

$$\chi_{combined} = \begin{bmatrix} \mathbf{Q}_{4a} & \mathbf{0}_{3x2} & \mathbf{0}_{3x2} & \mathbf{0}_{3x2} \\ \mathbf{0}_{3x2} & \mathbf{Q}_{4b} & \mathbf{0}_{3x2} & \mathbf{0}_{3x2} \\ \mathbf{0}_{3x2} & \mathbf{0}_{3x2} & \mathbf{Q}_{4c} & \mathbf{0}_{3x2} \\ \mathbf{0}_{3x2} & \mathbf{0}_{3x2} & \mathbf{0}_{3x2} & \mathbf{Q}_{12} \end{bmatrix} \tag{4.24}$$

and

$$\beta_{combined} = \begin{bmatrix} \beta_4 & \mathbf{0}_{6x2} \\ \mathbf{0}_{2x2} & \mathbf{I}_{2x2} \end{bmatrix} \tag{4.25}$$

Let

$$T = \chi_{combined}\beta_{combined} \tag{4.26}$$

The combined machine transformation matrix **T** is a 9x4 matrix.

$$T = \begin{bmatrix} 1.000 & 0 & 1.000 & 0 \\ 0.7660 & -0.6428 & -0.50 & -0.8660 \\ -0.9397 & 0.3420 & -0.50 & 0.8660 \\ -0.50 & -0.8660 & 1.0 & 0 \\ -0.9397 & -0.3420 & -0.50 & -0.866 \\ 0.1736 & -0.9848 & -0.50 & 0.8660 \\ -0.50 & 0.8660 & 1.0 & 0 \\ 0.1736 & 0.9848 & -0.50 & -0.8660 \\ 0.7660 & 0.6428 & -0.50 & -0.8660 \end{bmatrix} \tag{4.27}$$

The transformation matrix **T** has a rank of 4. This means that only four measured stator currents are needed to extract $\{i_{dqs4}\}$ and $\{i_{dqs12}\}$. Equation (4.28) shows the possible transformations, each transformation consisting of four rows of [**T**]

$$\begin{bmatrix} i_{ds4} \\ i_{qs4} \\ i_{ds12} \\ i_{qs12} \end{bmatrix} = \begin{bmatrix} T(1,:) \\ T(4,:) \\ T(2,:) \\ T(5,:) \end{bmatrix}^{-1} \begin{bmatrix} i_{S1} \\ i_{S4} \\ i_{S2} \\ i_{S5} \end{bmatrix} = \begin{bmatrix} T(1,:) \\ T(7,:) \\ T(2,:) \\ T(8,:) \end{bmatrix}^{-1} \begin{bmatrix} i_{S1} \\ i_{S7} \\ i_{S2} \\ i_{S8} \end{bmatrix} \tag{4.28}$$

$$= \begin{bmatrix} T(9,:) \\ T(3,:) \\ T(2,:) \\ T(5,:) \end{bmatrix}^{-1} \begin{bmatrix} i_{S9} \\ i_{S3} \\ i_{S2} \\ i_{S5} \end{bmatrix}$$

From 4.28 three new coordinate transformations can be defined as:

$$T1 = \begin{bmatrix} T(1,:) \\ T(4,:) \\ T(2,:) \\ T(5,:) \end{bmatrix}^{-1} \quad T2 = \begin{bmatrix} T(1,:) \\ T(7,:) \\ T(2,:) \\ T(8,:) \end{bmatrix}^{-1} \quad T3 = \begin{bmatrix} T(9,:) \\ T(3,:) \\ T(2,:) \\ T(5,:) \end{bmatrix}^{-1} \tag{4.29}$$

4.5.3 Example of Extraction of i_{dqs4} and i_{dqs12} from Four Stator Windings
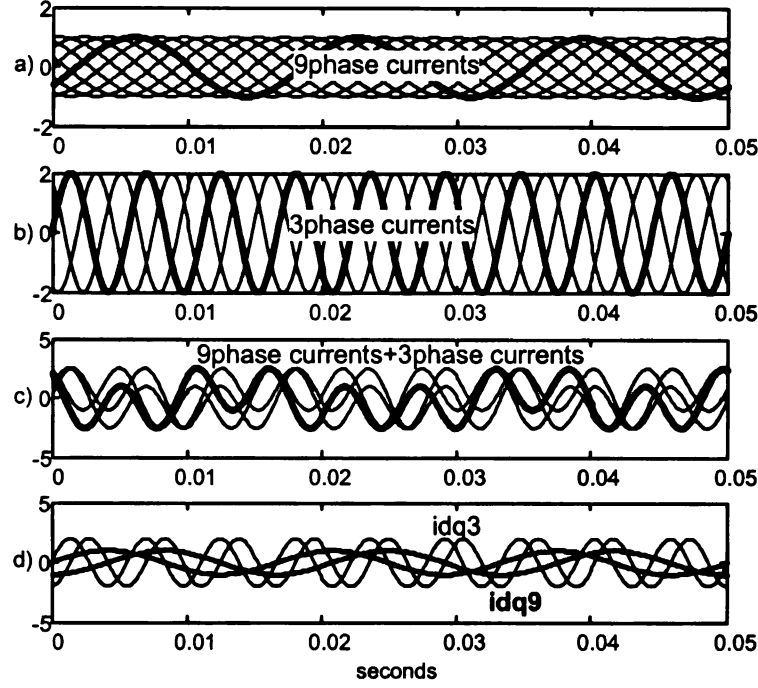
Figure 4.3: Example of decoupling idq3 and idq9 from 4 stator windings

The stator current contribution from the 4pole motor is shown in plot (a) of figure 4.3. These four currents are $\{i_{s4a}, i_{s4d}, i_{s4b}, i_{s4e}\}$ from equation (4.19). The stator current contribution from the 12-pole motor is shown in plot (b) of figure 4.3. The three currents are $\{i_{s12a}, i_{s12b}, i_{s12c}\}$ from equation (4.19). The currents of the 12-pole configuration have a frequency three times that of the currents of the 4-pole currents and twice the amplitude. Plot (c) shows the actual stator winding currents $\{i_{S1}, i_{S4}, i_{S2}, i_{S5}\}$ from (4.19), the current sum of the two independent motors. Using the transformation matrix of (4.28), the actual stator currents are decoupled into $\{i_{dqs4}\}$, and $\{i_{dqs12}\}$ as shown in plot (d).

4.6 Conclusions

In this chapter, a coordinate transformation for the pole-changing scheme of chapter 7 was developed. Based on the requirements of minimizing core losses and saturation avoidance, the

transformation mapped currents between the 9-phase symmetrical system, set up by the 9 stator windings, and orthogonal rotor flux reference frame. It was shown that this transformation can be reduced to a 4x4 transformation thus eliminating the need for four current sensors.

CHAPTER 5

Modeling and Simulations

5.1 Introduction

With the goal of controlling the experimental induction machine during pole-changing, a novel induction motor model was developed to analyze the current, flux and torque transient behaviors during pole-changing. The model is different from conventional induction motor models because the inductances are calculated from the actual stator windings, which are non-sinusoidally distributed.

Using this model, several different pole-changing scenarios are studied. For each case, no controller is employed. The first scenario is an instantaneous change in motor pole/phase configuration during steady state operation. The current and torque transients are evaluated.

Next, the change in configuration occurs during motor acceleration. The 3-phase/12-pole is accelerating from start, before asynchronous speed is reached the applied voltages are instantaneously changed to 9-phase/4-pole motor operation. The results are compared with the first scenario, transient result.

Finally, the produced electromagnetic torque and resulting phase currents are studied when input voltages consist of a combination of 3-phase/12-pole and 9-phase/4-pole motor steady state voltages. The air-gap flux distribution resulting from the different voltage combination ratios are shown using a finite element model of the machine.

5.2 Novel Induction Motor Model

Classical AC machine theory, i.e. generalized reference frame theory [13],[25], is not readily applicable to modeling this experimental machine for continuous operation pole-changing. In order to produce torque and current responses to pole-changing, the machine is modeled using fundamental magnetic theory.

Starting with the Fourier series expansion of the winding distribution, from chapter 3, the resulting air-gap flux density is derived. Integrating the flux density over the stator results in the flux-linkage. Both the mutual and self inductances of the machine are calculated.

5.2.1 Classical AC Theory: Generalized Reference Frame

In conventional models of asynchronous and synchronous machines the pole number, P, is an explicit factor in the electromagnetic torque equation. Equation (5.1) gives the the electromagnetic torque equation of a 3-phase, conventionally wound induction machine in the stator reference frame.

$$T_e = \left(\frac{P}{2}\right) (\mathbf{i}_{abcs})^T \left(\frac{\delta}{\delta \theta_r} [\mathbf{L}_{sr}]\right) \mathbf{i}_{abcr} \qquad (5.1)$$

Therefore, the pole number of the machine can only be changed by changing P. The challenge in modeling the experimental induction machine is simulating its pole-changing. The motor model for the proposed drive system ,the pole number should be a function of the applied voltages, not an explicit factor. This can be accomplished by deriving the self and mutual inductances, $\mathbf{L}_{sr}$ of (5.1), from the actual stator winding distribution.

In the actual machine the winding distribution allows for the formation of two different coil groupings, depending upon the applied voltages. As shown in chapter 3, one coil grouping arrangement results in four poles and the other results in the machine having twelve poles.

5.2.2   Inductance Calculation

Conventionally, when calculating inductances it is assumed that the stator windings are wound sinusoidally. Figure 5.1 shows the stator winding *as* for both an ideally wound 4-pole and 12-pole machine. The terms N_{s4} and N_{s12} are slot conductor densities. The winding function,
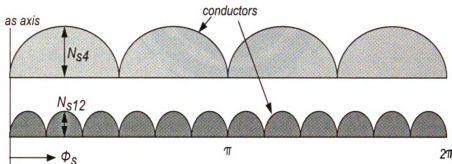
Figure 5.1: Stator Winding Conductor Density for a 4-pole and 12-pole Induction Motor.

n_{as}, for the ideally wound 4-pole machine is

$$
\begin{aligned}
n_{as} &= N_{s4}\sin(\phi_{as}) && 0 \le \phi_{as} \le \tfrac{\pi}{2} && \pi \le \phi_{as} \le \tfrac{2\pi}{3} \\
n_{as} &= -N_{s4}\sin(\phi_{as}) && \tfrac{\pi}{2} \le \phi_{as} \le \pi && \tfrac{2\pi}{3} \le \phi_{as} \le 2\pi
\end{aligned}
\tag{5.2}
$$

It has been shown [13] that a 2P-pole machine can be modeled as an equivalent 2-pole machine with a winding function of

$$
\begin{aligned}
n_{as} &= N_{s2}\sin(\phi_{as}) && 0 \le \phi_{as} \le \pi \\
n_{as} &= -N_{s2}\sin(\phi_{as}) && \pi \le \phi_{as} \le 2\pi
\end{aligned}
\tag{5.3}
$$

A 4-pole machine produces double the amount of torque and half the amount mechanical speed relative to electrical speed of a 2-pole machine for the same turns and current. This conventional model works for modeling the experimental induction machine in either the 4-pole or 12-pole configuration, but does not adequately model the motor in the transition between the two configurations. In order to understand the stator currents and the torque during the pole-changing transition, a model was developed that accounted for the non-ideal stator winding distributions. Figure 5.2 shows how one of the nine stator windings is distributed.

Each stator winding has 4 coil groups that are spaced 90 degrees around the stator, figure 5.3. Each of the coils spans 10 degrees. This conductor distribution allows the coils from
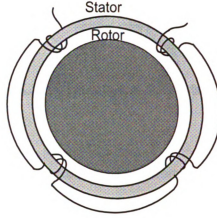
Figure 5.2: Location of one of the nine stator windings

adjacent windings to form larger phase belts; thus, making it possible to have different number of poles.
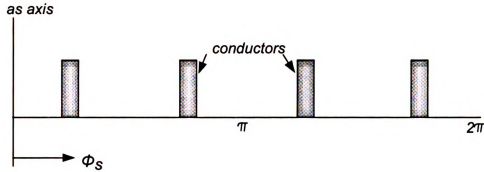
Figure 5.3: Conductor Density of one of the nine stator windings.

The Fourier series approximation of this winding distribution of figure 5.3 is given as

$$n_{as} = N_p \left[\frac{4}{\pi} \cos(\frac{4\pi}{9}) \sin(\phi_{as}) +] \frac{1}{3} \cos(\frac{12\pi}{9}) \sin(3\phi_{as}) \right.$$
$$\left. + \frac{1}{5} \cos(\frac{20\pi}{9}) \sin(5\phi_{as})... \right] \qquad (5.4)$$

where N_p is the maximum conductor density.

Figure 5.4 shows the conductor distribution using the first three terms of the Fourier series.

Using the distribution function of 5.4 and applying Ampere's Law, the mmf of winding *as*
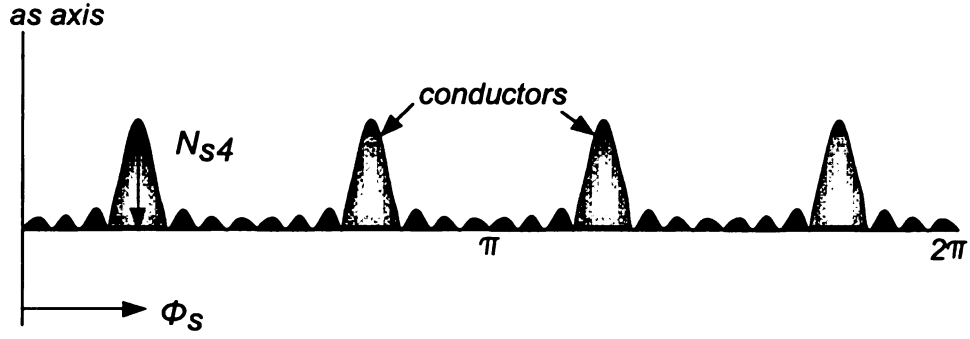
Figure 5.4: Conductor density waveform resulting from the first four terms of the Fourier series.

is

$$MMF_{as} = N_p i_{as} \int_0^\pi \left[\frac{4}{\pi} \cos(\frac{4\pi}{9}) \sin(\phi_{as}) + \frac{1}{3} \cos(\frac{12\pi}{9}) \sin(3\phi_{as}) \right. \tag{5.5}$$
$$\left. + \frac{1}{5} \cos(\frac{20\pi}{9}) \sin(5\phi_{as}) \right] d_{\phi s}$$

where i_{as} is the applied current. From the mmf, the flux density in the air-gap can be determined from

$$B_r(\phi_s) = \mu_o \frac{MMF_{as}(\phi_s)}{g} \tag{5.6}$$

where g is twice the air-gap length in the radial direction and μ_o is the permeability of air. The flux linkage of a single turn is:

$$\Phi(\phi_s) = \int_{\phi s}^{\phi s + \pi} B_r(\phi_s) r l d\phi_s \tag{5.7}$$

$$\Phi(\phi_s) = \frac{\mu_o}{g} \int_{\phi s}^{\phi s + \pi} MMF_{as}(\phi_s)(\phi_s) r l d\phi_s \tag{5.8}$$

$$\Phi(\phi_s) = \frac{\mu_o N_p i_{as}}{g} \int_{\phi s}^{\phi s + \pi} \int_0^\pi \frac{4}{\pi} \cos(\frac{4\pi}{9}) \sin(\phi_{as}) + \frac{1}{3} \cos(\frac{12\pi}{9}) \sin(3\phi_{as}) \tag{5.9}$$
$$+ \frac{1}{5} \cos(\frac{20\pi}{9}) \sin(5\phi_{as}) \ldots d\phi_s r l d\phi_s$$

69

The total flux linkage is

$$\lambda_{as} = L_{ls}i_{as} + \frac{\mu_o N_p^2 i_{as}}{g} \int \left[\frac{4}{\pi} \cos(\frac{4\pi}{9}) \sin(\phi_{as}) + \frac{1}{3} \cos(\frac{12\pi}{9}) \sin(3\phi_{as}) \right. \tag{5.10}$$

$$+ \frac{1}{5} \cos(\frac{20\pi}{9}) \sin(5\phi_{as})... \left] \int_{\phi_s}^{\phi_s + \pi} \int_0^\pi \frac{4}{\pi} \cos(\frac{4\pi}{9}) \sin(\phi_{as}) + \frac{1}{3} \cos(\frac{12\pi}{9}) \sin(3\phi_{as}) \right.$$

$$+ \frac{1}{5} \cos(\frac{20\pi}{9}) \sin(5\phi_{as})...d_{\phi s}rld\phi_s$$

Dividing by the current i_{as}, the the self inductance of winding a is

$$L_{asas} = L_{ls} + \left(\frac{N_s^2}{2} \right) \pi\mu_o rl\alpha_1 \tag{5.11}$$

From these calculations, the mutual inductance between stator winding a and rotor winding a is

$$L_{asar} = -0.133 \left[\cos(\theta_r) \right]^5 + 0.072 \left[\cos(\theta_r) \right]^3 + 0.117 \cos(\theta_r) + 0.120 \left[\cos(\theta_r) \right]^7 \tag{5.12}$$

The mutual inductance between stator winding b and rotor winding a is

$$L_{bsar} = -.042 \sin(\theta_r) + 0.127 \cos(\theta_r) - 0.032 \left[\cos(\theta_r) \right]^3 \tag{5.13}$$

$$+ 0.147 \left[\cos(\theta_r) \right]^5 - 0.092 \left[\cos(\theta_r) \right]^7 + 0.021 \sin(\theta_r) \left[\cos(\theta_r) \right]^4$$

$$- 0.027 \sin(\theta_r) \left[\cos(\theta_r) \right]^2 - 0.077 \sin(\theta_r) \left[\cos(\theta_r) \right]^6$$

The entire 9x9 matrix of the mutual inductance between rotor and stator windings is

$$L_{sr} = \begin{bmatrix} L_{asar} & L_{asbr} & L_{ascr} & L_{asdr} & L_{aser} & L_{asfr} & L_{asgr} & L_{ashr} & L_{asir} \\ L_{bsar} & L_{bsbr} & L_{bscr} & L_{bsdr} & L_{bser} & L_{bsfr} & L_{bsgr} & L_{bshr} & L_{bsir} \\ L_{csar} & L_{csbr} & L_{cscr} & L_{csdr} & L_{cser} & L_{csfr} & L_{csgr} & L_{cshr} & L_{csir} \\ L_{dsar} & L_{dsbr} & L_{dscr} & L_{dsdr} & L_{dser} & L_{dsfr} & L_{dsgr} & L_{dshr} & L_{dsir} \\ L_{esar} & L_{esbr} & L_{escr} & L_{esdr} & L_{eser} & L_{esfr} & L_{esgr} & L_{eshr} & L_{esir} \\ L_{fsar} & L_{fsbr} & L_{fscr} & L_{fsdr} & L_{fser} & L_{fsfr} & L_{fsgr} & L_{fshr} & L_{fsir} \\ L_{gsar} & L_{gsbr} & L_{gscr} & L_{gsdr} & L_{gser} & L_{gsfr} & L_{gsgr} & L_{gshr} & L_{gsir} \\ L_{hsar} & L_{hsbr} & L_{hscr} & L_{hsdr} & L_{hser} & L_{hsfr} & L_{hsgr} & L_{hshr} & L_{hsir} \\ L_{isar} & L_{isbr} & L_{iscr} & L_{isdr} & L_{iser} & L_{isfr} & L_{isgr} & L_{ishr} & L_{isir} \end{bmatrix} \tag{5.14}$$

5.2.3 Machine Model in Stator Reference Frame

The machine modeled in the stator reference frame is:

$$\begin{bmatrix} V_{abcdefghis} \\ V_{abcdefghir} \end{bmatrix} = \begin{bmatrix} r_s + pL_s & pL_{sr} \\ p(L_{sr})^T & r_r + pL_r \end{bmatrix} \begin{bmatrix} I_{abcdefghis} \\ I_{abcdefghir} \end{bmatrix} \tag{5.15}$$

$$T_e = \left(\mathbf{i}_{abcdefghis}\right)^T \left(\frac{\delta}{\delta\theta_r}([\mathbf{L}_{sr}])\right) \mathbf{i}_{abcdefghir} \tag{5.16}$$

where $\mathbf{L}_{sr}, \mathbf{L}_r, \mathbf{L}_s$ are the 9x9 inductance matrices described in the previous section. As mentioned previously, the inductance matrices are derived from only half of the windings because of rotor symmetry. The result is either a 2 or 6-pole motor instead of a 4 or 12-pole motor.

Rearranging equation 5.15 and setting $\mathbf{V}_{abcdefghir} = 0$

$$\mathbf{C}_s \left[\mathbf{V}_{abcdefghis} - \mathbf{r}_s\mathbf{I}_{abcdefghis} + \frac{d\mathbf{L}_{sr}}{dt}\mathbf{L}_r^{-1}\frac{d\mathbf{L}_{sr}}{dt}\mathbf{I}_{abcdefghir}\right] = \frac{d\mathbf{I}_{abcdefghis}}{dt} \tag{5.17}$$

$$\mathbf{C}_r \left[-\frac{d\mathbf{L}_{sr}^T}{dt}\mathbf{L}_s^{-1}\mathbf{V}_{abcdefghis} - \mathbf{r}_s\mathbf{I}_{abcdefghir} + \frac{d\mathbf{L}_{sr}^T}{dt}\mathbf{L}_s^{-1}\mathbf{r}_r\mathbf{I}_{abcdefghis}\right] = \frac{d\mathbf{I}_{abcdefghir}}{dt} \tag{5.18}$$

$$[T_e - T_{load}]\left(\frac{1}{J}\right) = \frac{d\omega_r}{dt} \tag{5.19}$$

$$\omega_r = \frac{d\theta_r}{dt} \tag{5.20}$$

where J is the rotor inertia and:

$$\mathbf{C}_s = \left[\mathbf{L}_s - \frac{d\mathbf{L}_{sr}}{dt}\mathbf{L}_r^{-1}\frac{d\mathbf{L}_{sr}}{dt}\right]^{-1} \tag{5.21}$$

$$\mathbf{C}_r = \left[\mathbf{L}_r - \frac{d\mathbf{L}_{sr}^T}{dt}\mathbf{L}_s^{-1}\frac{d\mathbf{L}_{sr}}{dt}\right]^{-1} \tag{5.22}$$

The term $d\mathbf{L}_{sr}/dt$ is the derivative of the mutual inductance.

5.3 Simulation Results

Equations (5.17) and (5.20) were implemented into a Matlab s-function for simulation. Three types of simulations were conducted. The first set of simulations validated the novel machine model, in addition, to producing current and torque transients resulting from pole-changing during steady state operation.

5.3.1 Simulation Simulink Model

Figure 5.5 shows the Simulink model of the experimental induction machine. (Again, the 12-pole and 4-pole motors are modeled as a 6-pole motor and a 2-pole motor.) Two different sets
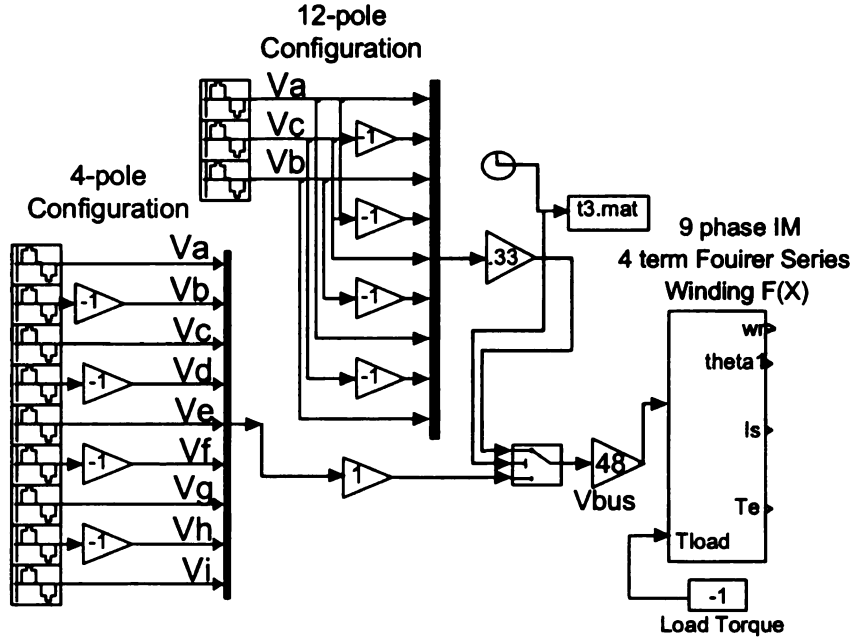
Figure 5.5: Experimental Induction Motor Model: Two Sets of Applied Voltages

of applied voltages were applied to the model. The set of nine voltages that result in a 6-pole motor are:

$$
\begin{array}{lll}
v_a(t) = \sin\left(2\pi t\right) & v_b(t) = \sin\left(2\pi t + \frac{2\pi}{3}\right) & v_c(t) = \sin\left(2\pi t + \frac{4\pi}{3}\right) \\
v_a(t) = \sin\left(2\pi t\right) & v_b(t) = \sin\left(2\pi t + \frac{2\pi}{3}\right) & v_c(t) = \sin\left(2\pi t + \frac{4\pi}{3}\right) \\
v_a(t) = \sin\left(2\pi t\right) & v_b(t) = \sin\left(2\pi t + \frac{2\pi}{3}\right) & v_c(t) = \sin\left(2\pi t + \frac{4\pi}{3}\right)
\end{array}
\tag{5.23}
$$

The nine currents that result in a 2-pole motor are:

$$
\begin{array}{lll}
v_a(t) = \sin\left(2\pi t\right) & v_b(t) = \sin\left(2\pi t + \frac{2\pi}{9}\right) & v_c(t) = \sin\left(2\pi t + \frac{4\pi}{9}\right) \\
v_d(t) = \sin\left(2\pi t + \frac{6\pi}{9}\right) & v_e(t) = \sin\left(2\pi t + \frac{8\pi}{9}\right) & v_f(t) = \sin\left(2\pi t + \frac{10\pi}{9}\right) \\
v_g(t) = \sin\left(2\pi t \frac{12\pi}{9}\right) & v_h(t) = \sin\left(2\pi t + \frac{14\pi}{3}\right) & v_i(t) = \sin\left(2\pi t + \frac{16\pi}{9}\right)
\end{array}
\tag{5.24}
$$

5.3.2 Model Validation of Pole-changing Machine

Applying the voltage sets of (5.23) or (5.24) to the motor model results in the motor accelerating freely. Figures 5.6.a and 5.6.b show the resulting speed and developed electromagnetic

(a) Speed of the 6-pole and 2-pole motor

(b) Electromagnetic Torque of the 6-pole and 2-pole motor
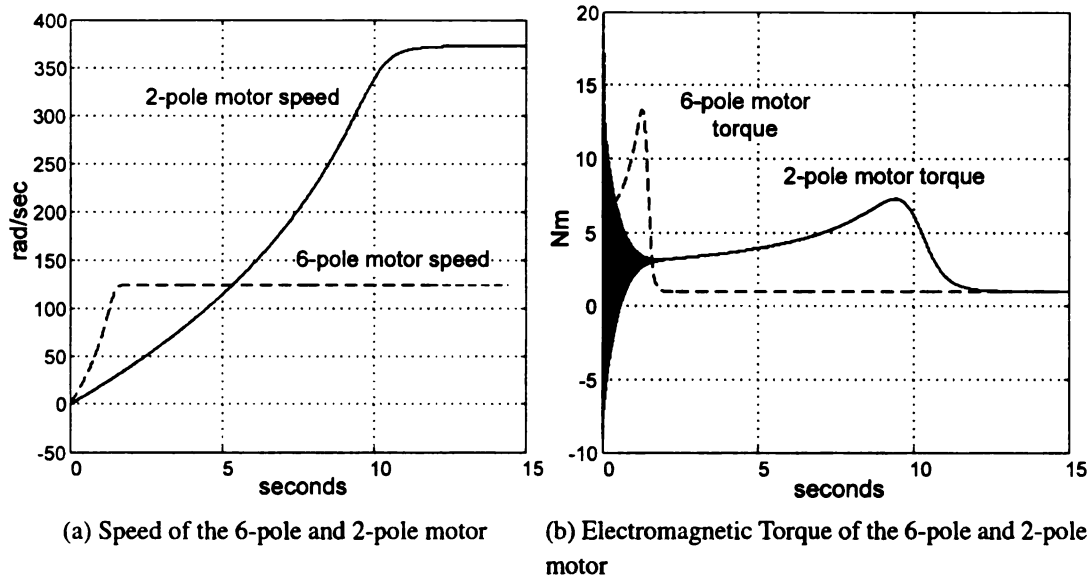
Figure 5.6: Comparison of Speed and Torque During Free Acceleration

torque from both the 2-pole configured motor and the 6-pole motor. A static load of $1Nm$ was applied.

The maximum speed obtained for the 2-pole machine is $372 rad/s$ and $123 rad/s$ for the 6-pole motor. The resulting speed and produced torque shows that the pole-number is changed when the voltages are changed, validating the concept of modeling inductances based the actual physical winding distribution in order to determine a motor pole number.
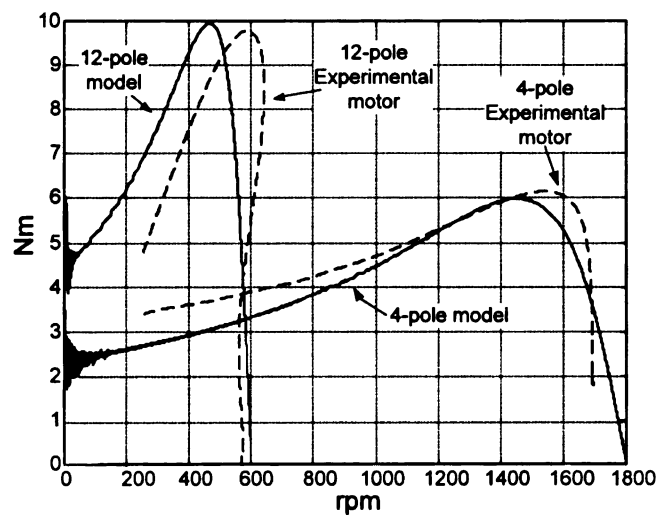
Figure 5.7: Open-loop, Speed-torque characteristics: Comparison of Experimental and Simulation Results.

The model response was also compared to actual machine response. In figure 5.7, the speed torque curves from actual operation of the 12-pole and 4-pole motors are compared with the model results. For this case, the resulting speed and torque of the 6-pole and 2-pole motor models were scaled by three in order to be compared with the actual motor results. (In chapter 6 the setup used to obtain the experimental results is described in detail.)

5.3.3   Instantaneous Pole-changing During Steady State Operation

Having developed a way to model pole-changing, the next step is to observe the effects of instantaneously changing the pole configuration. Figures 5.8.a and 5.8.b show the change in speed and torque when the applied voltages are instantaneously rearranged from one pole configuration to another. In this case the voltages are switched from the 6-pole configuration to the 2-pole configuration 3 seconds after the 6-pole motor reached steady state.

Figure 5.8.c shows the nine phase currents of the machine before and after the pole change. The resulting current transient lasts approximately $100ms$ and has a peak current twice that of the steady state current. These currents result in a large torque transient. The peak torque of this transient is larger in negative direction, approximately four times the starting torque of the 2-pole motor in figure 5.6.b. The effect of this adverse torque is a dip in speed immediately after the pole-change. The magnitude of the speed dip increases with increasing load until the 2-pole motor is unable to produce enough torque.

5.3.4   Instantaneous Pole-changing During Acceleration

In the second simulation scenario, the poles are changed while the 6-pole motor is accelerating. Figure 5.9.a compares the speed response of the conventional 2-pole motor to the speed response of the pole-changing motor, which switches from a 6-pole motor to a 2-pole motor when speed reaches $118rad/s$.

For the pole-changing motor, steady state is reached approximate 4 seconds sooner than the 2-pole motor. This shows that the continuously operated, 6/2 pole-changing induction machine has better response and range, than either the 2-pole or 4-pole motor.

(a) Speed

(b) Electromagnetic Torque
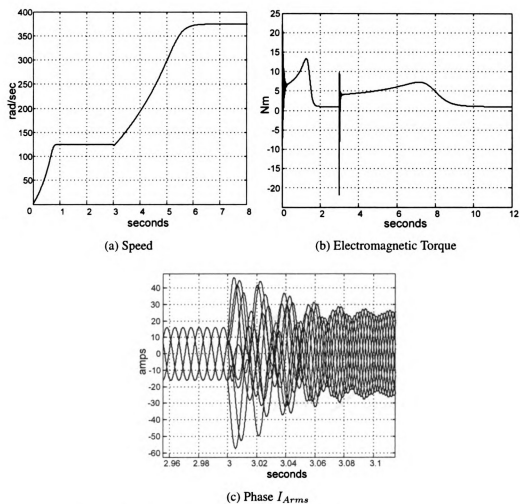

(c) Phase I_{Arms}

Figure 5.8: Pole-Changing from 6-pole to 2-pole at t=3seconds

(a) Speed

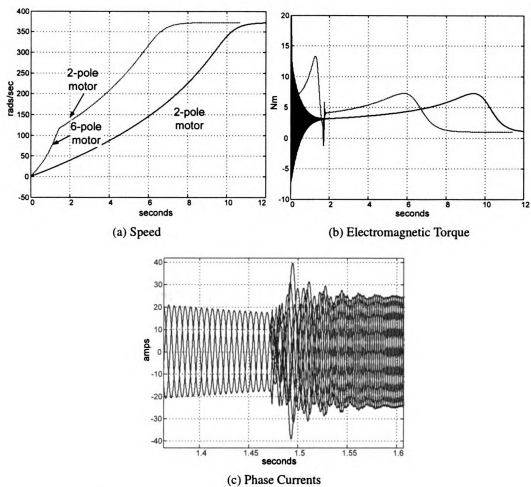(b) Electromagnetic Torque

(c) Phase Currents

Figure 5.9: Pole-Changing from 6-pole to 2-pole when speed reaches 118 radians per second

Figure 5.9.b shows the torque produced in both cases. The torque transient at the instant of pole-changing is less severe than that of the torque transient in figure 5.8.b. The peak current during the pole-changing transient is approximately half the peak current in figure 5.9.c when the poles are switched after the 6-pole motor reaches steady state. In the case of the pole-change during steady state the total flux level is at a minimum. When the 9-phase voltages are applied, the maximum flux is not instantaneously achieved. Its rate of increases is a function of motor parameters. Since the motor is loaded and the air-gap flux has not reached maximum, not enough torque is initially produced to prevent deceleration. In the case of motor changing poles prior to reaching steady state, the flux has not decreased to steady state level. When the 9-phase voltages are applied, there is enough flux to produce torque preventing the speed to dip. These results suggest that the key to smooth pole-changing is adjusting the flux prior to pole-changing. In chapter 7 this idea is expanded to simultaneously and independently controlling the air-gap flux of both pole configurations prior to, during, and after pole-changing.

5.3.5 Gradual Pole-changing

In the previous two sections, the instantaneous change in voltage results in large dV/dT currents in the windings. This suggests a gradual change in voltage to bring about a change in poles. In order to obtain an understanding of the effects of a gradual transition from one pole-configuration to the other, simulations were performed, where both the 9-phase voltage set, (5.24), and 3-phase voltage set (5.23) are simultaneously applied to the motor model. Three separate voltage combinations are applied to the motor model: 1)80% of the voltages from the 3-phase set plus 20% of the 9-phase voltage set. 2) 20% 9-phase and 80% 3-phase voltages and 3)50% 3-phase voltages and 50% 9-phase voltages. Again no speed or torque control is implement.

Figures 5.10.a shows the speed response of motor for each of the three combinations of applied voltages. When the combination of 20% of 9-phase voltage and 80% 3-phase voltage are applied, the motor operates as a 6-pole but produces less torque than the motor with 100%

77

(a) Speed

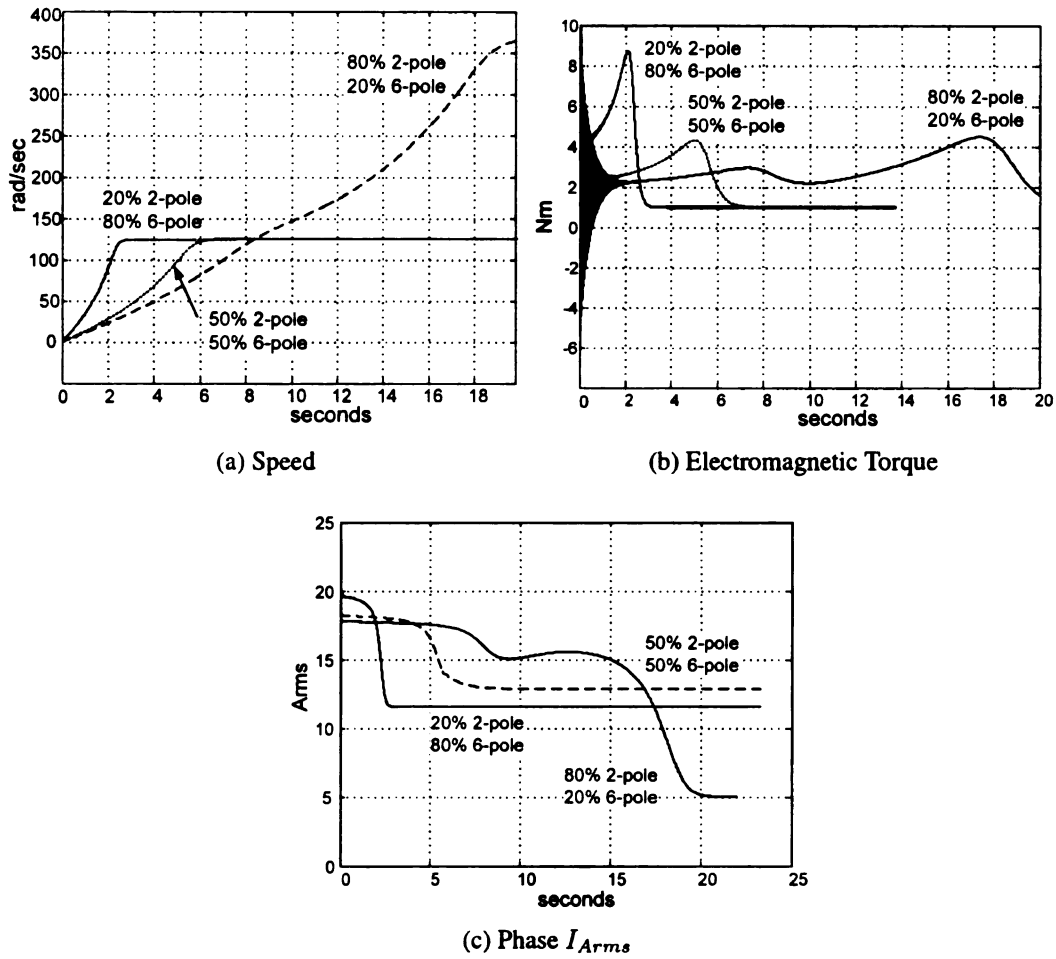(b) Electromagnetic Torque

(c) Phase I_{Arms}

Figure 5.10: Comparison of Speed, Torque and Current for different voltage combinations

applied 3-phase voltage set. Likewise, for the combination of 50%9-phase and 50% 3-phase applied voltages, the motor responds as sluggish 6-pole motor. However, when the combination of 80% 9-phase and 20% 3-phase applied voltages, motor reaches 2-pole asynchronous speed, but much slower that if the applied voltages were 100% as in figure 5.6.b. Figure 5.10.b shows the corresponding produced torque. Figure 5.10.c shows the corresponding phase a rms current. In the two cases were the motor only reached a steady state speed of $122rad/s$ the the rms phase current was greater than the phase current of the motor with 100% 3-phase voltages. Therefore, the motor efficiency is reduced.

In order to better understand the air-gap flux distribution in this case, FEA was performed on the machine, using a commercial package, Flux2D. Figure 5.11 shows the magnetizing flux for the 3phase-12pole configuration.

This model was build using Flux-2D. The purpose of this model was to analyze the air-gap flux distribution during the pole-changing transition.

As shown in figure 5.11.c, when the applied voltages are a combination of 80% 9-phase and 20% 3-phase voltages, twelve pole are established, 4 dominant poles and 8 minor poles. The 4 dominant poles result in the motor responding as a 4-pole motor and reaching the steady state speed of $372rad/s$, but less efficient than a 4-pole motor. As the percentage of 9-phase voltage decreases and the percentage of 3-phase voltage increases, the 4 dominant poles' flux path becomes smaller and smaller to a point were the twelve poles dominant and the motor responds 12-pole motor. This transitions occurs at approximately at the combination of 75% 9-phase and 25% 3-phase voltages. Experimental results confirmed this.

The significance of figure 5.11.c is that two fields can be established in the air-gap and torque can be produced.

5.4   Conclusions

Deriving the self and mutual inductances from the actual physical stator winding distribution enables the simulation the pole-changing capability of the actual machine. The number of poles is implicitly incorporated in the induction machine electrical equations through the in-
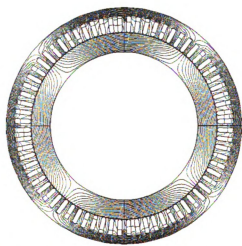
(a) Flux paths: 4-pole motor with 9-phase voltages applied
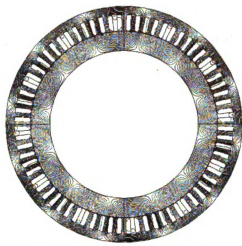
(b) Flux paths: 12-pole motor with 3-phase voltages applied

(c) Magnetizing flux pattern for 80% 9-phase voltage and 20% 3-phase voltage.

Figure 5.11: Flux Distribution: Flux 2D

ductances. However, approximating the winding distribution using Fourier series results in a more complex and computational intensive model, compared to the conventional modeling techniques where the winding distribution is sine function.

Instantaneous pole-changing results in large torque transients and undesired speed decreases. It was noticed that the current and torque transients were less severe if the pole-changing occurred prior to reaching steady states operation. This suggest that the key to obtaining a smooth pole-changing is adjusting the air-gap flux levels prior to pole changing. In addition it is shown that two air-gap fluxes can simultaneously exist.

CHAPTER 6

Experimental Setup: Hardware and Software
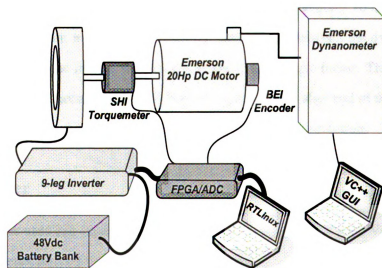
6.1 Introduction

Figure 6.1: Overall Experimental Setup

The laboratory setup consisted of standard equipment and specially developed hardware for this effort.
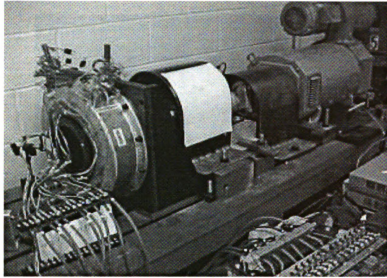
Figure 6.2: Overall Experimental Setup

6.2 Hardware Setup

Figures 6.1 and 6.2 show the major components of the experimental setup. The four-quadrant Emerson Industrial 20HP Dynamometer was used to load the machine. To interface with and control the dynamometer, a Visual C++ GUI was developed. Between the dynamometer and the induction motor is the in-line SHI MCRT model 9-02T torque meter. This meter is rated at 22 Nm and has an of accuracy +/- 0.02 Nm. Mounted on the other end of the dynamometer motor shaft is the BEI incremental encoder with 2048 pules per revolution.

6.2.1 Inverter

The 9-leg inverter used can supply a maximum of 25 Arms per phase at 60 Vdc. It consists of three 3-leg Powerex IGBT Modules and 9 current sensors.

6.2.2 FPGA/ADC Interface

Figure 6.4 is a functionality block diagram of the FPGA/ADC Interface. It was designed on a Xilinx x4008 FPGA using the Xilinx Foundation Series 2.1i. The design uses 192 Configurable Logic Blocks (CLB) with 98% utilization of gates. A 15MHz crystal oscillator supplies

Figure 6.3: 9-leg Inverter

the clock signal. The FPGA/ADC Interface has several functions, which are:

1. Generating 18 PWM pulses based on Symmetrical SVPWM, with dead-time;

2. Calculating the position, speed and direction of the motor from the encoder's quadrature signals;

3. Controlling three 14-bit ADCs, which sample and convert the nine phase currents (or eight currents and one torque signal);

4. Controlling the EPP parallel port communications with the PC; and

5. Generating external interrupt signal for the control program located on the PC.

Using the 9-phase SVPWM algorithm developed in chapter 2, the FPGA/ADC Interface produces 12-bit resolution PWM signals. In addition, a preset dead-time is implemented in the signals. Located off the FPGA, but powered and controlled by it, the ADC board is used for measuring the nine winding currents. Three Maxim high-speed, multichannel, 14-bit data-acquisition ICs, measure the nine Hall effect current probes. The three ADCs convert three samples simultaneously in $3\mu s$; the total conversion time of all nine samples is under $11\mu s$. The ADC board interfaces with the FPGA via a 12-bit data bus (only 12 bits of resolution are
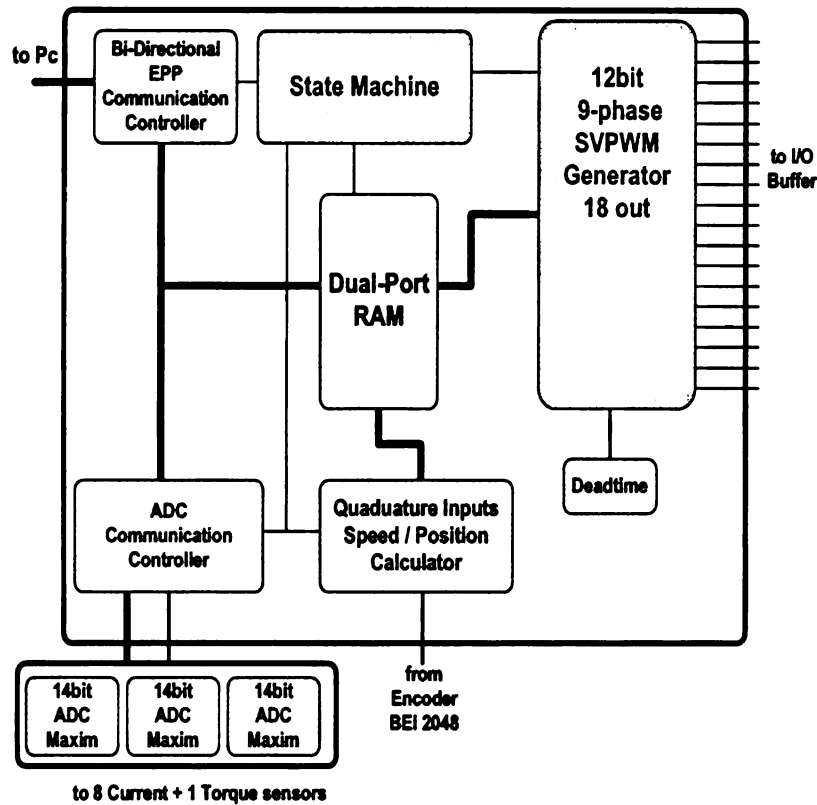
Figure 6.4: FPGA/ADC PWM Functionality Block Diagram

used, due to I/0 constraint of the FPGA) and a 4-bit control bus. The currents are sampled and converted at the PWM switching frequency.

The switching frequency is updated every interrupt from the PC. For this work the switching frequency was a constant 6.5KHz. (This was reduced from 10KHz due to the length of the control program, and the required number of sample conversions.) The FPGA/ADC Interface initiates the control interrupt. (This task was originally assigned to the PC; however, the RTLinux thread could not produce a consistent interval.) The FPGA/ADC Interface sends an interrupt signal to the PC parallel port (IRQ 7) to initiate the control program. The PC used for this work is the 2500MHz Intel Pentium 4 Processor.

6.3 Software

For this work, data was acquired and analyzed, using Matlab, on the control processor. As previously mentioned, the operating system of the PC is a RTLinux patched kernel [3]. It is a "deterministic," real-time operating system [4]. A major advantage of using RTLinux is that the control code can be ported easily to another PC. Another advantage of using RTLinux is the use of a multi-functional complex processor, which greatly aids in the development process. Data acquisition is more convenient, because data does not have to be moved to another platform for analysis.

The actual control program is written in C++ and implemented as an RTLinux thread. Figure 6.5 shows the overall organization of the control program thread and its interactions. The thread is set to the highest priority, an advantage of RTLinux.

Two separate threads are developed: the control routine and the sensor calibration routine. The sensor calibration routine is initiated upon startup. The gain and offsets of current sensors are normalized and nulled. Upon completion, the control thread is enabled and enters a wait state until an external IRQ interrupt. While in the wait state, lower priority applications, i.e. user threads such as data acquisition and the GUI, can operate.

Data is be passed from the real-time thread to the user thread via FIFOs (first-in-first-out). Much of the experimental data for this work was collected using this technique. In addition, data can be passed from user applications to the real-time thread, i.e. speed or torque commands from the GUI.

The interrupt cycle begins with the FPGA/ADC Interface initiating the ADC sample-hold and the conversion of the phase currents. Once the conversion is complete, the interrupt signal is sent to the control thread. However, due to the high latency of IRQ interrupt, the interrupt signal is sent after the second AD conversion. The control thread then requests the transfer of current data (12 11-bit words) from the FPGA/ADC Interface. The FPGA/ADC Interface negotiates the communications with the PC, using Microsoft's Enhanced Parallel Port Protocol, EPP mode.

Once the current, speed and position data are uploaded to the PC the current measurements
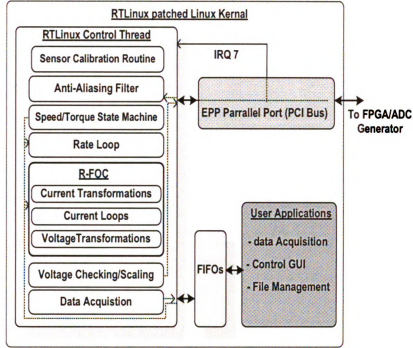
86

Figure 6.5: Software Organization

are passed through anti-aliasing filters.

After current and speed data are transferred, the control program begins. A PI compensator, with anti-windup, is used for the speed loop. The resulting torque command is passed to the R-FOC routine. This routine is discussed in the next chapter. The commanded voltages are scaled and checked against the DC bus, (6.1).

$$\sqrt{(Vq_{total})^2 + (Vd_{total})^2} \leq \frac{Vdc}{\sqrt{3}} \qquad (6.1)$$

The commanded voltages are transferred to the FPGA/ADC Interface for PWM calculation and output.

6.4 Power

The power flow of the experimental setup is shown in figure 6.6. The dynamometer is fed with 3-phase 460Vrms voltage from an isolation transformer, which is connected to the building's high voltage transformer. Power for the 9-leg inverter is supplied by a 48 Vdc battery pack.
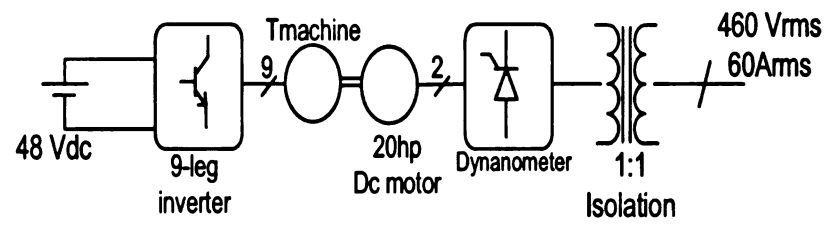
87

Figure 6.6: Experimental Setup Power Diagram

CHAPTER 7

Control of the Pole-Changing Motor

7.1 Introduction

In this chapter a novel control scheme for a pole-changing induction machine is introduced. During the pole-changing transition the machine is controlled as two separate motors, a 4-pole and a 12-pole. During the transition, the total produced torque and flux are a sum of the torque and flux produced by the 4-pole and 12-pole motors. A dual rotor flux oriented control (R-FOC) scheme is introduced [11]. Using the coordinate transformation developed in chapter 4, both sets of commanded currents are realized on the nine stator windings.

First, R-FOC is reviewed. Using conventional R-FOC for each configuration, speed-torque curves, speed response, and torque response are presented. Using the coordinate transformation of chapter 4, a dual R-FOC scheme is developed and presented. Results showing that the two motors can operate simultaneously and produce torque are presented.

As was revealed in chapter 5, the key to a smooth pole transition is adjusting the flux. For the novel pole-changing scheme both motor flux and torque levels are adjusted during the transition. Results showing the flux and torque of both motors during pole-changing are presented.

Finally, an overall torque management strategy is proposed, along with simulated results.

7.2 Review of Rotor Flux Oriented Control (R-FOC) of Induction Motors

The induction machine equations from chapter 5 are presented here for convenience.

$$
\begin{bmatrix} \mathbf{V}_{abcdefghis} \\ \mathbf{V}_{abcdefghir} \end{bmatrix} = \begin{bmatrix} \mathbf{r}_s + p\mathbf{L}_s & p\mathbf{L}_{sr} \\ p(\mathbf{L}_{sr})^T & \mathbf{r}_r + p\mathbf{L}_r \end{bmatrix} \begin{bmatrix} \mathbf{I}_{abcdefghis} \\ \mathbf{I}_{abcdefghir} \end{bmatrix}
\tag{7.1}
$$

$$
T_e = (\mathbf{i}_{abcdefghis})^T \left(\frac{d}{d\theta_r}([\mathbf{L}_{sr}]) \right) \mathbf{i}_{abcdefghir}
\tag{7.2}
$$

As shown in [14] and [25], transforming the induction machine equations into the rotor flux-linkage, Ψ_{rr}, reference frame, fast torque control can be achievable. The three relevant reference frames, stationary (or stator), rotor and rotor flux-linkage, are shown in figure 7.1,[25]. The rotor flux-linkage space vector is the sum of the transformed stator and rotor currents
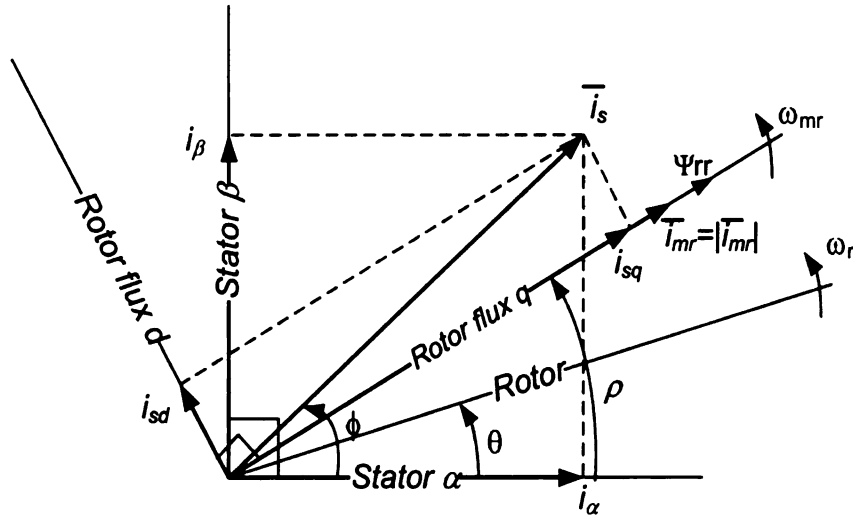
Figure 7.1: Stator, Rotor and Flux currents

$$
\overline{\Psi}_{rr} = L_r \overline{i}_{rr} + L_m \overline{i}_{sr}
\tag{7.3}
$$

where L_r is the rotor self inductance and L_m is the magnetizing inductance. From the rotor flux-linkage space vector, the magnetizing current space vector is defined as:

$$
\overline{i}_{mr} = \frac{\overline{\Psi}_{rr}}{L_m}
\tag{7.4}
$$

From figure 7.1 the magnetizing current is collinear with the quadrature component of the stator current space vector in the rotor flux reference frame. The relationship between these two vectors is found from performing a coordinate transformation on the rotor voltage equation of (7.1) into the rotor flux reference frame.

$$\overline{u_r} = R_r \overline{i}_{rr} + \frac{d\overline{\Psi}_{rr}}{dt} + j(\omega_{mr} - \omega_r)\overline{\Psi}_{rr} \tag{7.5}$$

With the rotor voltage set to zero, the transformed equation is split into orthogonal parts. The imaginary part is:

$$T_r \frac{d\overline{i}_{mr}}{dt} + \overline{i}_{mr} = i_{sq} \tag{7.6}$$

with

$$T_r = L_r / R_r \tag{7.7}$$

From the real part of the transformed rotor voltage equation

$$\omega_{mr} = \omega_r + \frac{i_{sd}}{T_r |\overline{i}_{mr}|} \tag{7.8}$$

From equation (7.6), the magnetizing current can be controlled by the stator current. The desire to control magnetizing current is due to the following

$$T_e = \left(\frac{3P}{2}\right) \frac{L_m^2}{L_r} |\overline{i}_{mr}| i_{sd} \tag{7.9}$$

From equation (7.9) the electromagnetic torque is determined by the magnetizing current and the direct component of the stator current in the rotor flux reference frame. Similar to controlling a DC machine, one of the variables is held constant, field flux, and the other is adjusted, the armature current, to control the torque. In the case of an induction machine, the magnetizing current is held constant because of its relatively slow time constant, T_r and i_d is adjusted to achieve the desired torque.

7.2.1 Current Loops

Equations (7.6) and (7.8) result from coordinate transformation on the rotor voltage equation into the rotor flux reference frame. Performing the same transformation on the stator voltages

91

results in:

$$\sigma T_s \frac{d\bar{i}_{sr}}{dt} + \bar{i}_{sr} = \frac{\bar{u}_{sr}}{R_s} - j\omega_{mr}\sigma T_s \bar{i}_{sr} - (1-\sigma)T_s\left(j\omega_{mr}|\bar{i}_{mr}| + \frac{d|\bar{i}_{mr}|}{dt}\right) \qquad (7.10)$$

where the stator time constant is $T_s = L_s/R_s$ and the total leakage factor is $\sigma = 1 - L_m^2/(L_r L_s)$. The two components of the stator current space vector in the rotor flux reference frame are i_d and i_q:

$$\bar{i}_{sr} = i_d + ji_q = i_s e^{-j\rho} \qquad (7.11)$$

Replacing the stator current space vector in (7.11) with i_d and i_q, and separating the equation into real and imaginary parts yields:

$$\sigma T_s \frac{di_d}{dt} + i_d = \frac{u_d}{R_s} + \omega_{mr}\sigma T_s i_q - (1-\sigma)T_s\frac{d|i_{mr}|}{dt} \qquad (7.12)$$

$$\sigma T_s \frac{di_q}{dt} + i_q = \frac{u_q}{R_s} - \omega_{mr}\sigma T_s i_d - (1-\sigma)T_s|i_{mr}|\omega_{mr} \qquad (7.13)$$

Ignoring the coupling terms on the right side of the stator voltages of (7.12) and (7.13), the relationships between the current and the voltage become:

$$\sigma T_s \frac{di_d}{dt} + i_d = \frac{u_d}{R_s} \qquad (7.14)$$

$$\sigma T_s \frac{di_q}{dt} + i_q = \frac{u_q}{R_s} \qquad (7.15)$$

A current loop model is shown in figure 7.2. Pole-zero cancelation between the first-order
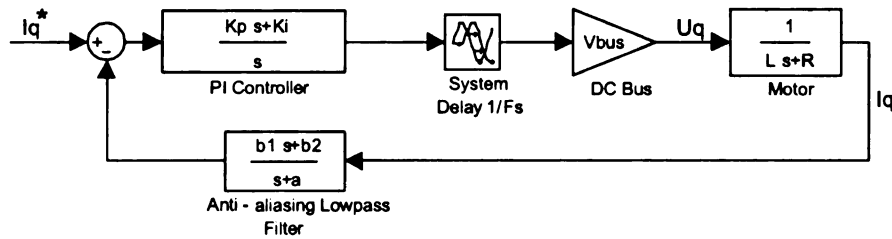

Figure 7.2: Simple Current Control Loop.

models of the motor and the PI controller was used to determine the gains of the controller. The goal was unity gain for the current control loops for both of the motor configurations. The bandwidth chosen for both current loops was 150Hz and the switching frequency was 5.6kHz.

As shown by Kazmierkowski, [17], the terms containing the magnetizing current of (7.11) can be neglected because of the relatively large time constant and high switching frequency of the inverter. Due to fast switching, the inverter acts as current source, impressing AC currents onto the motor stator windings [14]. The two coupling voltage speed terms from equation (7.11) are:

$$u_{sdx} = \omega_{mr}\sigma T_s i_q$$
$$u_{sqx} = -\omega_{mr}\sigma T_s i_d$$

(7.16)

These can be treated as feed-forward terms and added to the output of the PI controller. Figure 7.3 shows the two current controllers and the decoupling network. As shown in figure 7.3, an
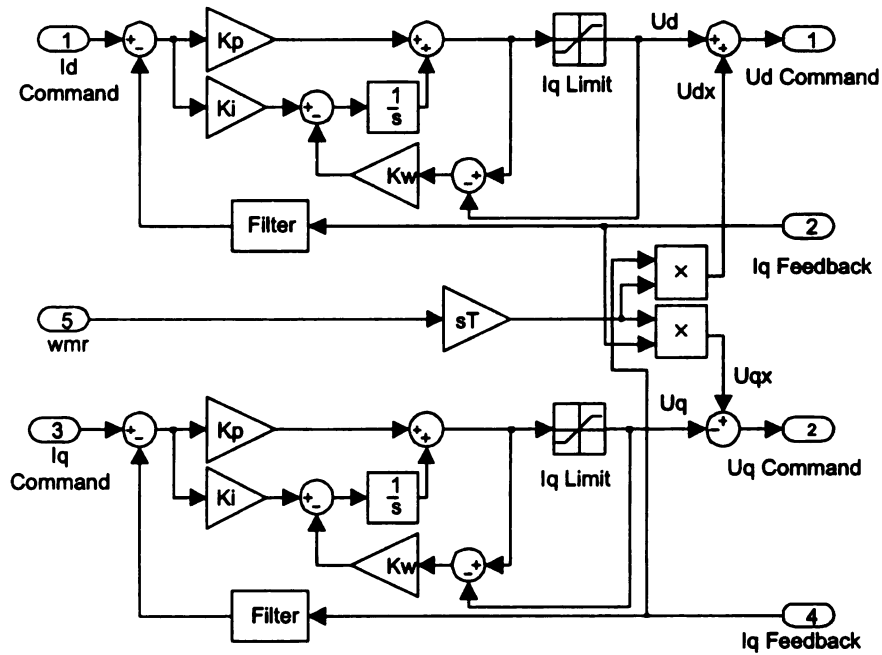

Figure 7.3: Iq Current Control Loop with Anti-windup.

anti-windup term was added to the PI controller. Figure 7.4 shows the flux model.

For the 4-pole motor, the SVPWM scheme introduced in chapter 2 is used. The motor parameters from Table 3.5 were used for tuning the current control loops and the slip estimator. Using the setup described in chapter 6, experiments were conducted. In the following section the results are presented.
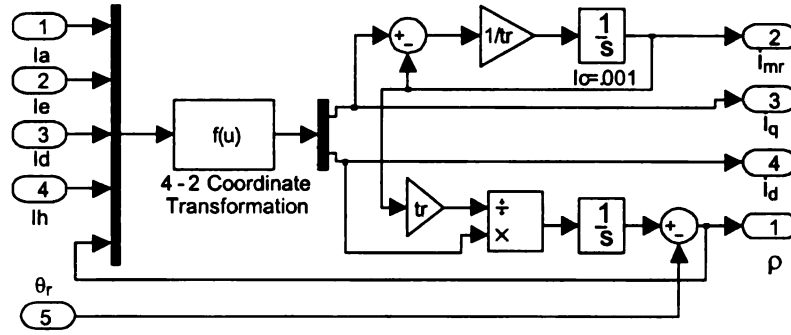
Figure 7.4: Magnetizing current i_{mr} and Rotor Flux angle ρ Model

## 7.2.2 Performance Results of the 12-pole and 4-pole Motor

In this section, the experimental motor was operated in both the 4-pole and 12-pole motor configurations. The dynamometer was operated in speed regulation mode with a set point of 500 rpm. Figures 7.5.a and b show the response of the 12-pole motor to an i_d command. This command was a dc biased square wave. In figure 7.5.a the commanded and resulting currents are plotted. The current i_q is commanded at 5 A.

The plot of i_q shows the the effect of some current coupling. This was due to saturation. Figure 7.5.b compares i_d feedback with the measured torque. Similar to 12-pole testing, the 4-pole motor was loaded by the dynamometer operating at 500 rpm in speed regulation. Figures 7.5.c and d show the resulting i_d and i_q and measured shaft torque. The flux producing current command for the 4-pole motor, i_q, was 3.5 A. From figure 7.5.c, no coupling effects were noticed. Figure 7.6 shows the results of testing the bandwidth of the current controller for the 4-pole configuration. A swept sine input was applied to the i_d current loop. The loop was designed for a bandwidth of 150Hz. However, only 75Hz bandwidth was obtained. This can be explained by the large inertia load of the dynamometer motor. The speed controller used for both motor configurations was a PI controller with anti-windup. Figures 7.7.a and b show the speed response of both motors to a step command. Figures 7.7.c and d show the speed torque curves for each configuration. The curves were obtained by operating the motors in velocity mode and the dynamometer in torque mode.
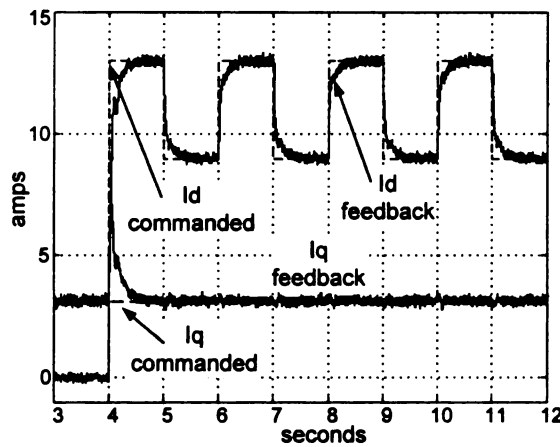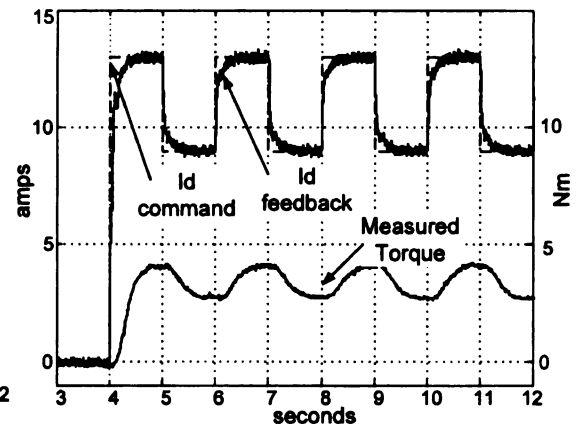
The results of the experiments show:
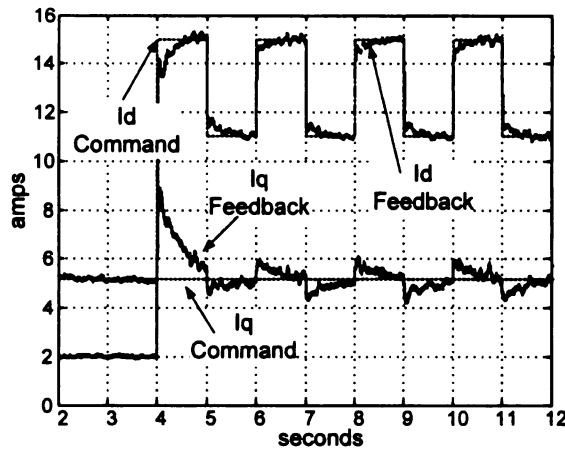
(a) iq12,id12 Feedback
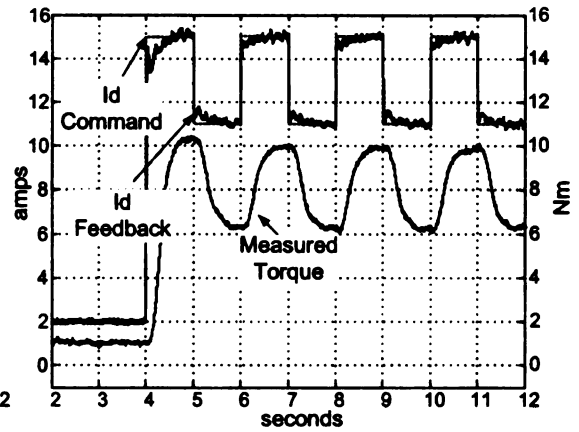
(b) id12 Commanded (solid),id12 Feedback (dashed), Measured Torque)

(c) iq4,id4 Feedback

(d) iq4 Commanded (solid),iq4 Feedback (dashed), Measured Torque)

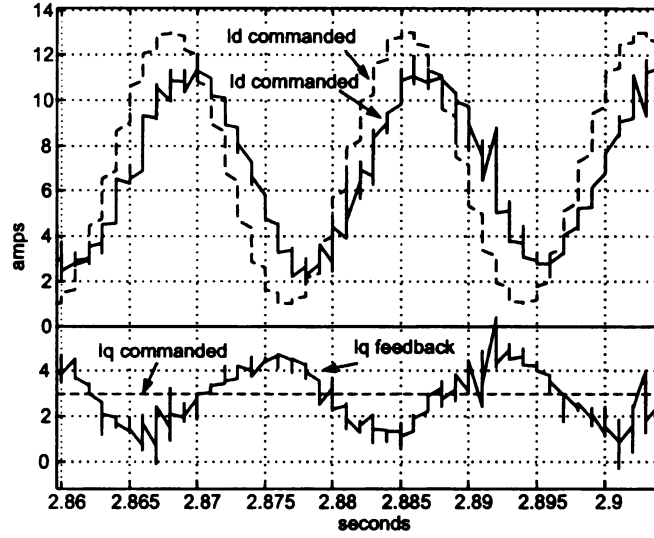Figure 7.5: 12-pole and 4-pole id Control

95

Figure 7.6: Id frequency response (between 60-70Hz

1. The experimental pole-changing motor can operate either as a 4-pole motor or a 12-pole motor;

2. The produced speed-torque characteristics of both motors; and

3. Both motors can be controlled with field oriented control.

The third result is the most important, as it leads to the simultaneous control of both motors with all four current components, i_{d4}, i_{q4}, i_{d12} and i_{q12}, separately controlled.

7.2.3   Experimental Results of 4-2 Coordinate Transformation

In order to proceed to the objective of independently controlling both motors simultaneously, the coordinate transformation proposed in chapter 4 is verified. One of the results of coordinate transformation (4.27) is that only four of the nine phase currents are needed to calculate $i_{s\alpha\beta4}$ and $i_{s\alpha\beta12}$ from which i_{d12}, i_{q12}, i_{d4} and i_{q4} are estimated. Using different combinations of four phase currents, the three coordinate transformations of (4.29), $T1$, $T2$ and $T3$, each result in the same estimated current sets, $i_{s\alpha\beta4}$ and $i_{s\alpha\beta12}$. The following experiments show that averaging the resulting currents from each transformation results in more accurate estimations.
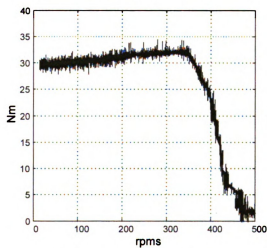
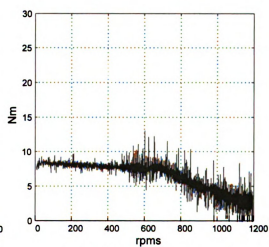Figure 7.8.a shows the estimated currents i_{d4} and i_{q4} from the $T1$ transformation. Figure
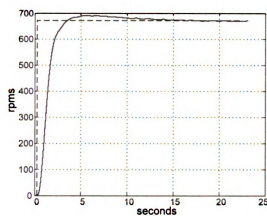
(a) 12-pole Speed Response
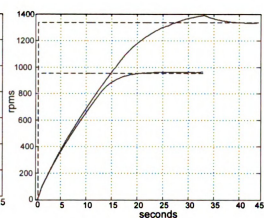
(b) 4-pole Speed Response

(c) 12-pole Speed-Torque Curve

(d) 4-pole Speed-Torque Curve

Figure 7.7: Motor performance: Speed Response

(a) T1: 4 of the 9 phase currents

(b) $(T2 + T3)/2$: 6 of the 9 phase currents

(c) $(T1 + T3)/2$: 6 of the 9 phase currents

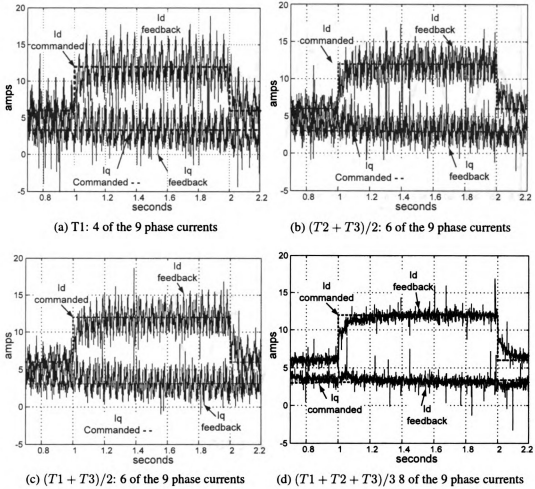(d) $(T1 + T2 + T3)/3$ 8 of the 9 phase currents

Figure 7.8: 4-2 Coordinate Transformation

7.8.b shows the estimated currents i_{d4} and i_{q4} resulting from the averaging of the calculated currents $i_{s\alpha\beta T2}$ and $i_{s\alpha\beta T3}$ from $T2$ and $T3$ respectively. Figure 7.8.c shows the estimated currents resulting from the averaging of the calculated currents $i_{s\alpha\beta T1}$ and $i_{s\alpha\beta T3}$ from $T1$ and $T3$ respectively. Finally, figure 7.8.d shows the estimated currents i_{d4} and i_{q4} resulting from the averaging of the calculated currents $i_{s\alpha\beta T1}$, $i_{s\alpha\beta T2}$ and $i_{s\alpha\beta T3}$ from $T1$, $T2$ and $T3$ respectively.

The noise is a result of measured phase current offsets. Averaging the outputs of the transformations filters the noise. The following figures show the calculated $i_{\alpha 4}$ and $i_{\beta 4}$ currents for the $T1$, $(T1 + T2)/2$ and $(T1 + T2 + T3)/2$.

Figure 7.9.a shows the stator currents $i_{s\alpha}$ for: $T1$, the average of $T1$ and $T2$ and the average

(a) $is\alpha$ for during i_d step command

(b) Closer view of $is\alpha$

(c) Closer view of $is\beta$
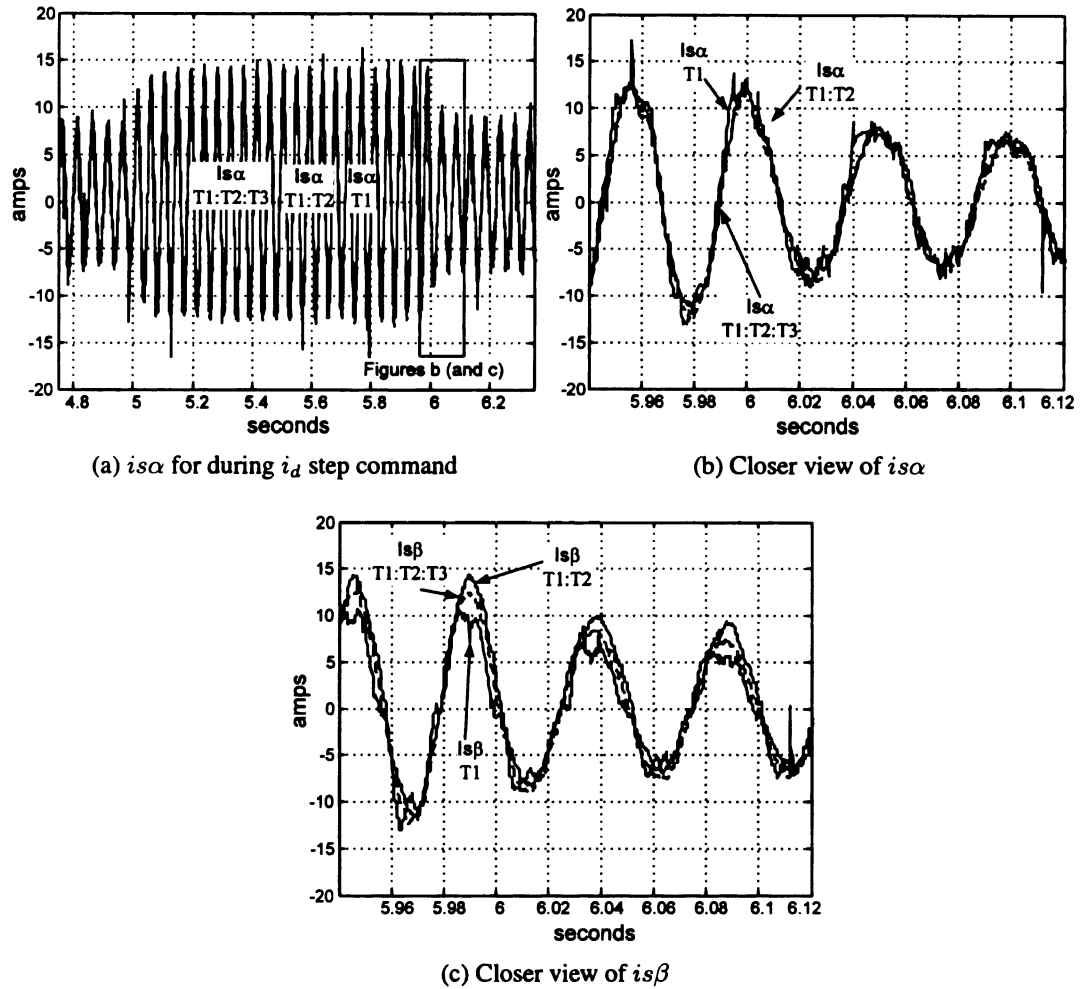
Figure 7.9: Reduced Coordinate Transformation: Orthogonal Stator Current Component $i_{s\beta}$ and $i_{s\alpha}$

of $T1$, $T2$ and $T3$, during the torque step command of the previous figures. Figures 7.9.b and c show a close up view of the currents during the torque transient. All three stator current components are in phase, showing that all three coordinate transformations of 4.29 calculate the same $i_{s\alpha4}$ and $i_{s\beta4}$ currents.

7.3 Simultaneous Operation of 12/4-pole Motor

The results of chapter 5 revealed large torque and current spikes resulting from the instantaneous switching between pole configurations. There, it also was shown that the motor can operate with a combination of 12-pole and 4-pole applied voltages. Therefore, it should be
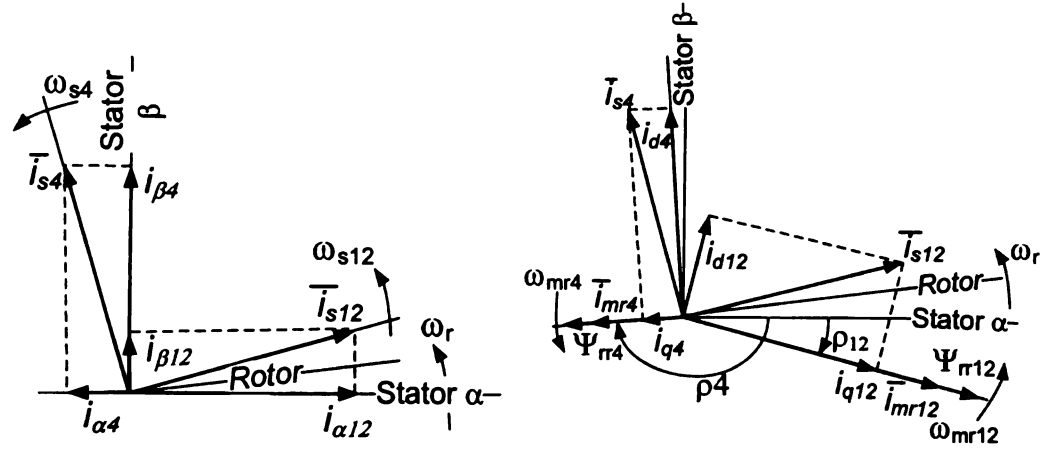
(a) 4-pole Stator Flux and 12-pole Stator Flux (b) 4-pole and 12-pole Rotor Flux Reference Frame moving independently

Figure 7.10: Dual 12-pole and 4-pole Reference Frames

possible to have a gradual change in pole configuration, avoiding these large current transients while still operating. A scheme was devised, [8], to simultaneously operate the experimental motor torque as the superposition of torques from the 4-pole and the 12-pole motor.

7.3.1 Dual FOC

In order to independently control each motor, the two sets of torque and field producing currents, i_{dq12}, for the 12-pole motor and i_{dq4}, for the 4-pole motor, have to be independent. For conventional rotor flux orientation the orthogonality of the stator current components i_α and i_β is preserved when these currents are transferred into the rotor flux reference frame. It was shown in chapter 4 that the coordinate transformations (4.29) produce two independent sets of orthogonal currents from a 9-phase symmetrical system. These two orthogonal currents can be mapped into their respective rotor flux reference frames.

Figure 7.10 show the two space vector currents $\bar{i}_{s4}$ and $\bar{i}_{s12}$ rotating over the same stator windings. These two independent resultant current space vectors can be produced by the 9-leg inverter. The total stator current of the motor is

$$\bar{i}_{StatorTotal} = \bar{i}_{s4} + \bar{i}_{s12} \tag{7.17}$$

Applying the coordinate transformation (4.28) results in two orthogonal currents sets $i_{s\alpha\beta4}$

100

and $i_{s\alpha\beta12}$ rotating with respect to each other at a rate of $\omega_{s4} - \omega_{s12}$. Figure 7.10.b shows the two current sets $i_{s\alpha\beta4}$ and $i_{s\alpha\beta12}$ mapped into their respective rotor flux-linkage reference frames, Ψ_{rr12} and Ψ_{rr4}, and rotating with respect to each other at $\omega_{mr4} - \omega_{mr12}$. The two independent stator currents of (7.17) establish two independent rotor fluxes, shown in (7.18) in their respective reference frames.

$$
\begin{aligned}
\overline{\Psi}_{rr12} &= L_{r12}\overline{i}_{rr12} + L_{m12}\overline{i}_{sr12} \\
\overline{\Psi}_{rr4} &= L_{r4}\overline{i}_{rr4} + L_{m4}\overline{i}_{sr4}
\end{aligned}
\tag{7.18}
$$

Following equations (7.4)-(7.8):

$$
\overline{i}_{mr12} = \frac{\overline{\Psi}_{rr12}}{L_{m12}}
\tag{7.19}
$$

$$
\overline{i}_{mr4} = \frac{\overline{\Psi}_{rr4}}{L_{m4}}
\tag{7.20}
$$

$$
T_{r12}\frac{d\overline{i}_{mr12}}{dt} + \overline{i}_{mr12} = i_{sq12}
\tag{7.21}
$$

$$
T_{r4}\frac{d\overline{i}_{mr4}}{dt} + \overline{i}_{mr4} = i_{sq4}
\tag{7.22}
$$

with

$$
T_{r4} = L_{r4}/R_{r4}
\tag{7.23}
$$

$$
T_{r12} = L_{r12}/R_{r12}
\tag{7.24}
$$

$$
\omega_{mr12} = \omega_{r12} + \frac{i_{sd12}}{T_{r12}|\overline{i}_{mr12}|}
\tag{7.25}
$$

$$
\omega_{mr4} = \omega_{r4} + \frac{i_{sd4}}{T_{r4}|\overline{i}_{mr4}|}
\tag{7.26}
$$

From equation (7.9) the torque for a conventional motor is the product of two components, $i_{mr} = (\Psi_{rr}L_r)$ and i_d in the same reference frame, the rotor flux reference frame. The torque is invariant to the change in reference frames, i.e. the torque calculated in the rotor flux reference is the same torque in the stationary reference frame and the rotor reference frame. In the case of controlling two motors there are two reference frames, where torque is produced, defined

by $\overline{\Psi}_{rr12}$ and $\overline{\Psi}_{rr12}$ respectively. The torques, Te_{12} and Te_4, can be calculated in each of their respective reference frames and summed.

$$T_{total} = 9\frac{L_{m12}^2}{L_{r12}}|\bar{i}_{imr12}|i_{d12} + 3\frac{L_{m4}^2}{L_{r4}}|\bar{i}_{imr4}i_{d4}| \qquad (7.27)$$

In the following section are the results of several experiments where the total shaft torque is shown to be the sum of both motor torques. In order to conduct these experiments, the control scheme of figure 7.11 was used.
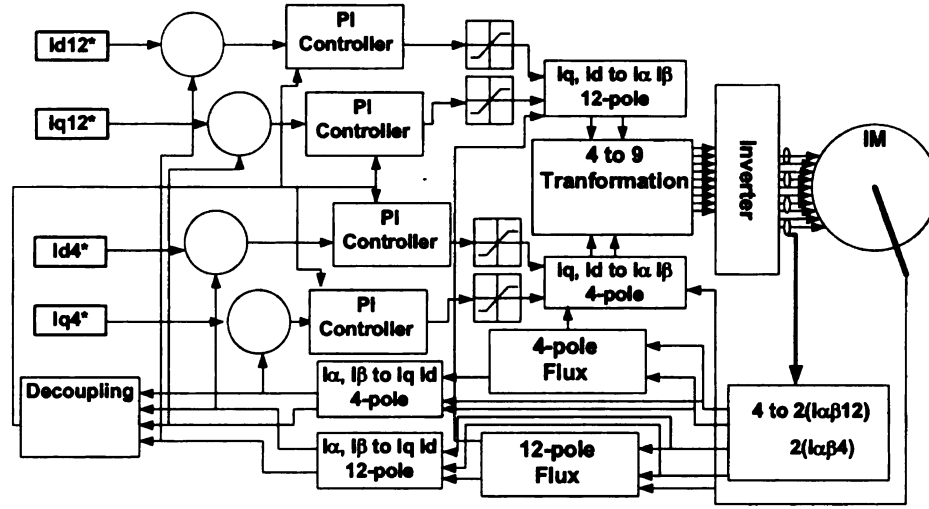

Figure 7.11: Dual machine control scheme.

7.3.2 Experimental Results: Controlling idq_4 and idq_{12}

This sections shows the results of controlling the 12-pole and 4-pole motors simultaneously and independently. Operating in speed mode at 600 rpm, the dynamometer acted as the motor load. The shaft torque was measured between the dynamometer and motor. As shown in figure 7.11, the current commands for the 12-pole motor are i_{d12} and i_{q12}, and for the 4-pole motor the commands are For the first experiment the flux producing currents of both motors, i_{q12} and i_{q4}, were held constant as was i_{d12}. A DC biased square wave was the i_{d4} command. As shown in figure 7.12, the dual motor control scheme effectively decouples i_{d4} and i_{dq12}. The resulting torque is the sum of the constant torque from the 12-pole motor and varying torque of the 4-pole motor. i_{d4} and i_{q4}.
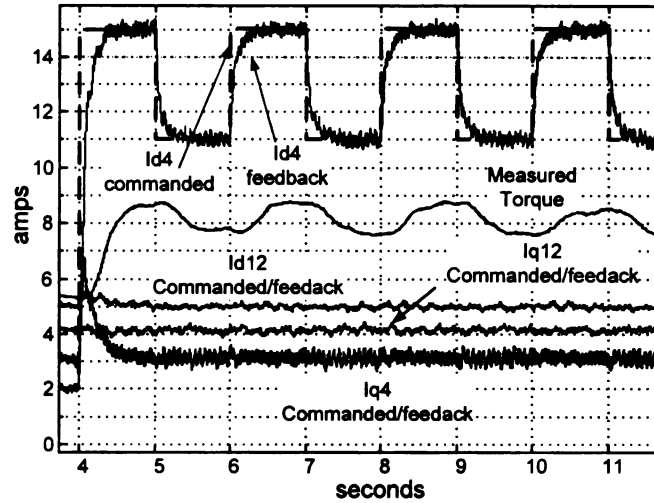
Figure 7.12: Torque, i_{d4}, step command

For the next experiment, the torque commanded for both motors was a DC biased square wave. The square waves were 180 degrees out of phase and scaled appropriately in order to produce a total constant torque. Both flux levels were held constant, as shown in figures 7.13.a and b. Figure 7.13.b shows i_{q4} and i_{q12} feedback. The resulting shaft torque stayed relatively constant.

For the final experiment, all four currents, i_{dq4} and i_{dq12}, were varied7.13.c.From the start to t_0, only the 12-pole motor is commanded to produce torque. Between t_0 and t_1, the 4-pole motor commands, i_{d4} with i_{q4} still set to zero. As expected there is no change in torque. Likewise, when the 4-pole commands i_{q4} with i_{d4} commanded back to zero, no additional torque is produced. However, when both i_{d4} and i_{q4} are nonzero as well as i_{d12} and i_{d12} the torque increases during t_2 to t_3.

As shown in the previous experiments, both 12-pole motor torque and 4-pole motor torque can be commanded simultaneously with the resultant torque being the summation. Therefore, during pole-changing, both motors can produce torque at the same time, making a gradual pole-changing transition possible.
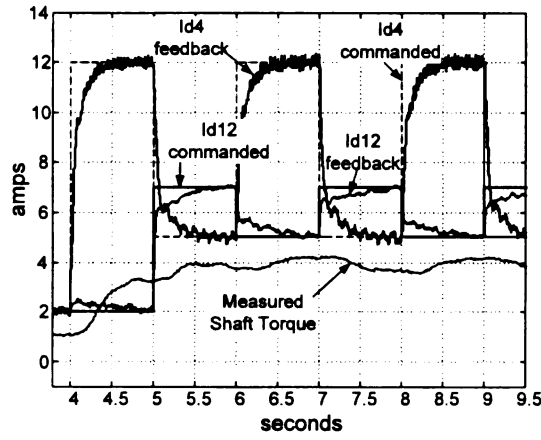
(a) 4 and 12-pole torque commands and measured shaft torque
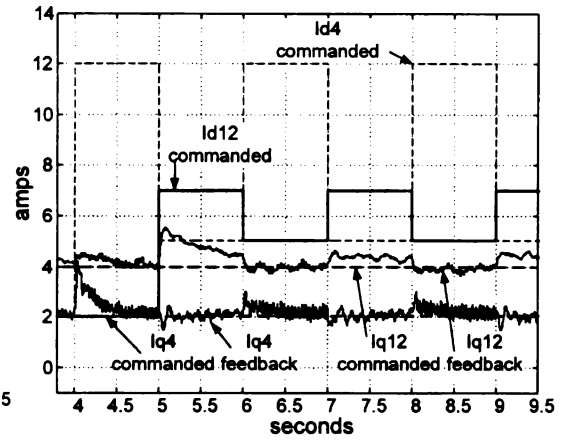
(b) The estimated and commanded flux of both motors
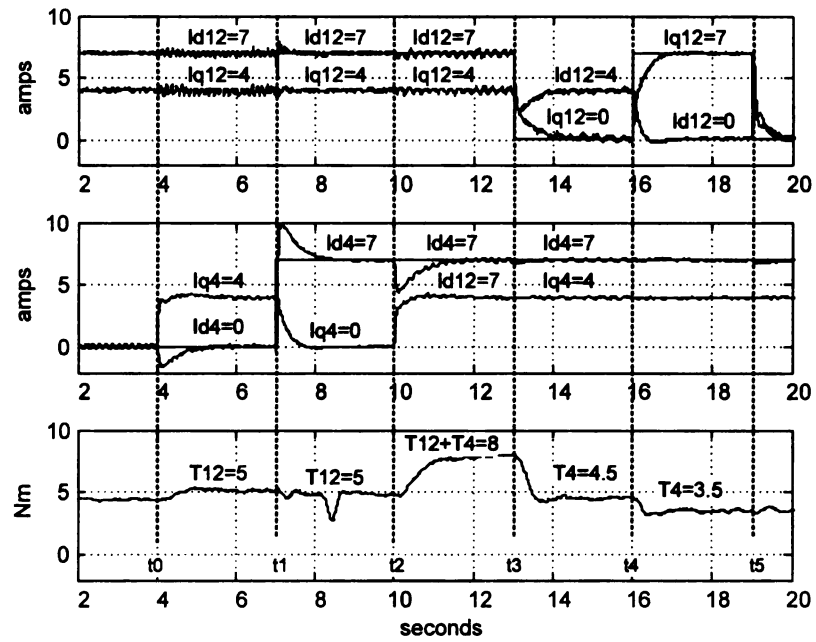
(c) Idq12 vs Idq4

Figure 7.13: 4-pole and 12-pole alternating torque commands

Figure 7.14: Pole-changing control scheme

7.4 Pole-Changing Transition: Flux Control

It previously has been shown that pole-changing during motoring operation results in large current and torque transients. For propulsion applications, large torque transients result in speed oscillations, while current 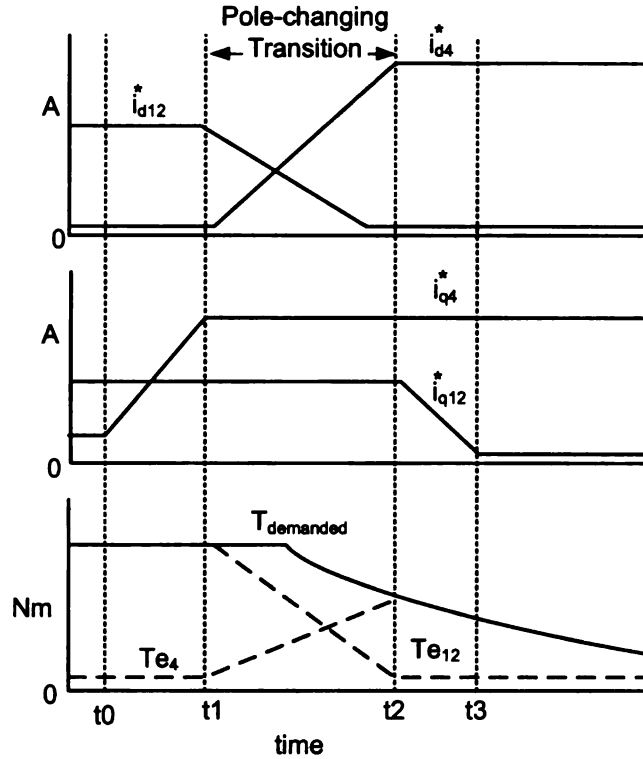transients result in saturation and excess thermal loading. In order to avoid such transients a novel control scheme for an induction machine drive system was developed [8]. The induction machine's flux and torque levels are controlled and adjusted in a manner to guarantee smooth torque production during pole-changing. In order to control the flux and torque level during pole-changing, the control scheme of simultaneous operation of the 12-pole and 4-pole motors is used.

While in the current pole configuration, the flux of the desired pole configuration is established. Next, the produced torque of the current pole configuration is decreased while the torque of the desired pole configuration is increased. The sum of both torques meets the demanded torque. Once the demanded torque is met solely by the new pole configuration, the

old pole configuration flux is decreased. Figure 7.14 demonstrates the transitioning from a 12-pole configuration to a 4-pole motor configuration.

First, the 4-pole flux is established. During this period, t_0-t_1, the 4-pole motor does not produce torque, while the 12-pole motor continues to meet the demanded torque. Once the 4-pole rotor flux has been established, after τ_4 seconds, i_{d4} is increased and i_{d12} is decreased. During this period, t_1-t_2, both motors are producing torque to meet the demand. Once the 4-pole motor is the sole torque producer, the 12-pole flux can be decreased.

The rate at which the fluxes are adjusted depends on several things, the rotor flux time constants of both machines τ_4 and τ_{12} and the total saturation level. During simultaneous torque production, the risk of saturation increases due to the presence of two flux fields. Both fluxes have to be adjusted to prevent saturation and to maintain useable torque.

An example of the pole-changing scheme is shown in figure 7.15. The figure shows the transition period of approximately $1s$.
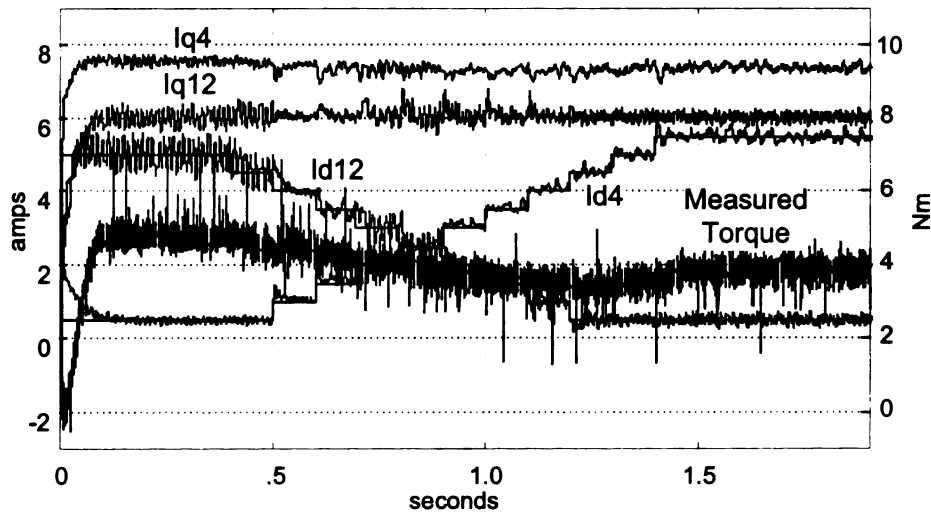

Figure 7.15: Gradually adjusting i_{d4} and i_{d12}

7.5 Possible Implementation Strategy for Novel Pole-changing Control in a Vehicle

The experimental induction motor drive system has four operating states, the 12-pole high torque state and the 4-pole high speed state and two additional states resulting from field weakening. The four operating states are shown in terms of torque and speed capability in figure 7.16.
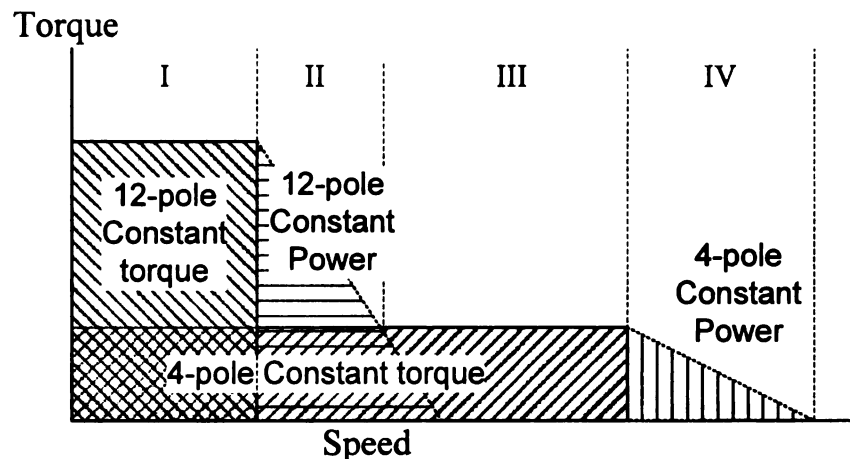

Figure 7.16: Constant torque and power regions

Determining which operational state depends on the torque and speed demands. For a vehicle, the first state of operation is the 12-pole motor for high starting torque. This is followed by the 12-pole constant power state, to continue acceleration. For cruising, the next state is the 4-pole constant torque state. For higher speeds, the next state is the 4-pole constant power state.

This control strategy can be viewed as a state machine. The transition diagram shown in figure 7.17.

Both speed and torque are required to determine which configuration meets the application's demands.

For the following simulation, the transition diagram without field weakening was used. Figure 7.18 compares the response of three closed-loop, speed control schemes. In the first
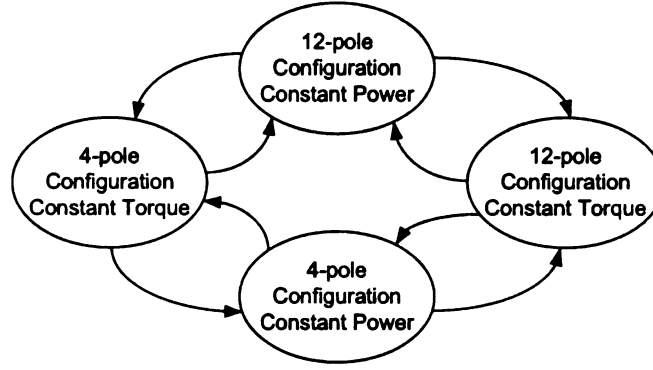
Figure 7.17: Control States with field weakening

case, the pole-changing induction drive is operated entirely in the 9-phase/4-pole configuration. Given a speed command of $100rad/s$ the machine took approximately 6 seconds to reach 95% of the desired speed. In the second case, when the speed reached $70rad/s$ the torque command i_{d12} was instantaneously switched to zero while i_{d4} was commanded to 100%. In this case, it took 4.5 seconds for the machine to reach 95% of desired speed. In addition, at $70rad/s$ the speed did not increase for 0.5 seconds. In the third simulation, the pole-changing scheme is used. In this case, the machine took approximately 3 seconds to reach 95% of desired speed.

Figure 7.19 shows the torque response for all three simulation cases. Comparing the torque responses of figure 7.19b and 7.19c, the torque produced was less erratic when the pole-changing scheme was employed.
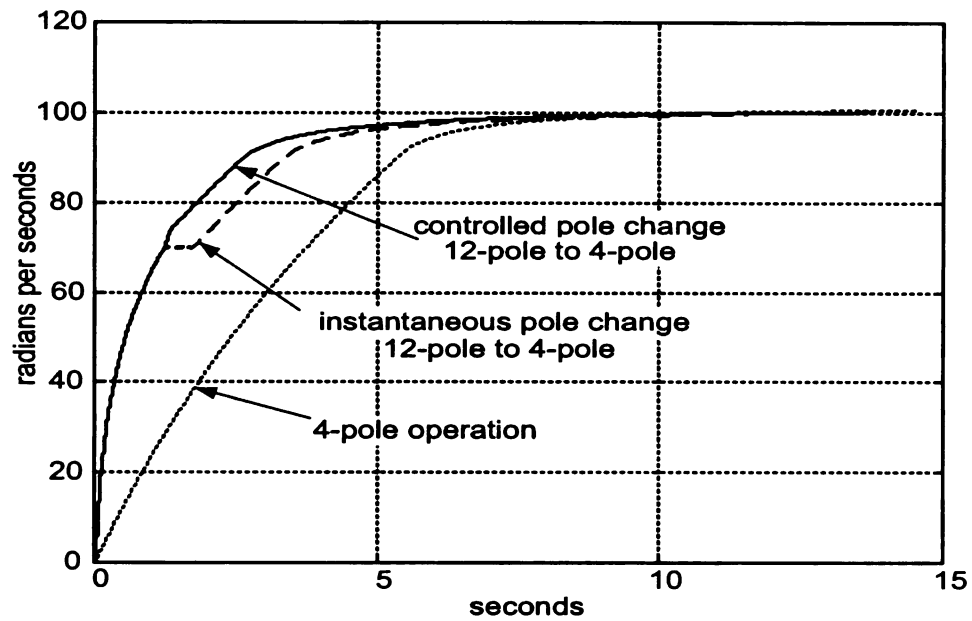
Figure 7.18: Speed comparison (simulation): 4pole operation, instantaneous pole change, controlled pole change.
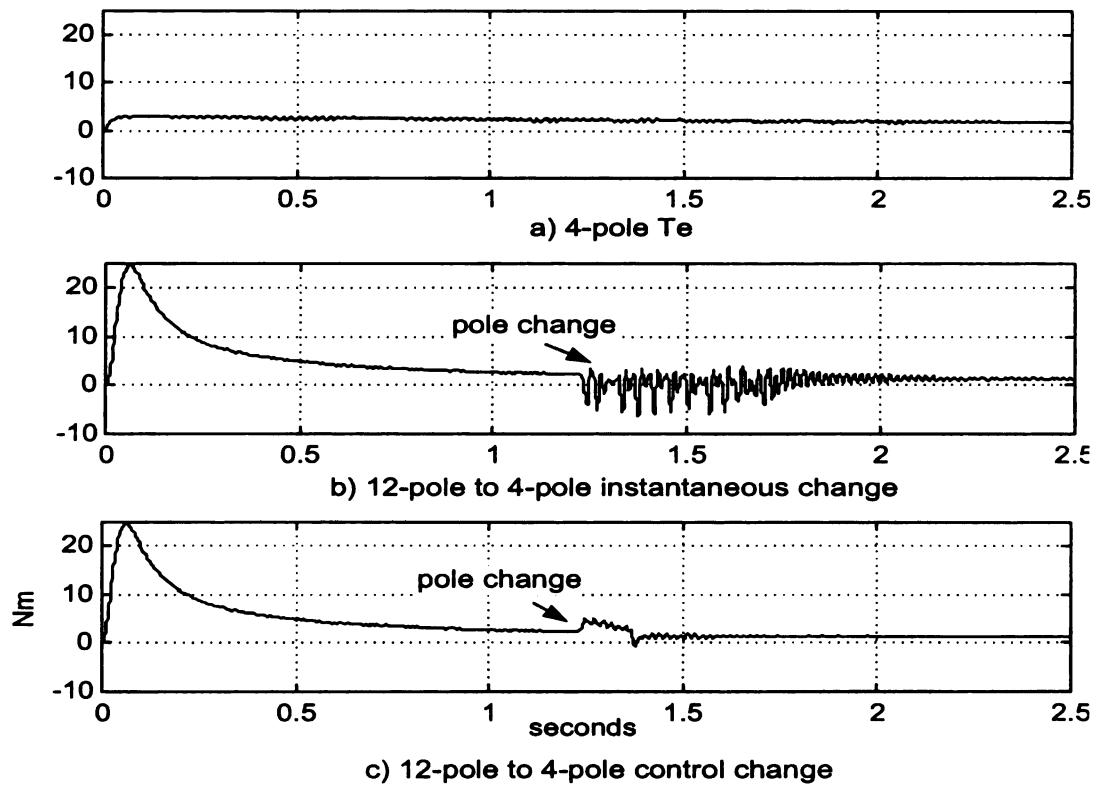

a) 4-pole Te

b) 12-pole to 4-pole instantaneous change

c) 12-pole to 4-pole control change

Figure 7.19: Torque Comparison (simulation): a) 4pole operation b) instantaneous pole change 12 to 4 c) controlled pole change

CHAPTER 8

Conclusions

The presented work is an extension of previous work on the integral starter/alternator. The toroidally wound, induction machine was designed as the starter/alternator for 42 Volt vehicles. As part of the starter/alternator effort, the induction machine and 9-leg inverter were designed and constructed. In addition, previous analysis included: calculation of steady state parameters for both the 3-phase/12-pole and 3-phase/4-pole configurations, development of vector control of both configurations and thermal analysis of the machine.

Discontinuous operation, zero torque production, is a consequence of pole-changing between starter and alternator operations. As part of the work presented, a control scheme was developed which results in continuous operation and smooth torque production during the pole-changing transition. Therefore, a novel induction drive system with speed/torque capabilities greater than equivalent sized conventional systems was presented, with the intention of being utilized in applications such as hybrid vehicle propulsion.

8.1 Accomplishments

As a consequence of the development of the pole-changing control scheme, the following items were accomplished in this work:

1. A PWM scheme for 9-phase operation was developed and implemented. As a result, of this work a generalized scheme for n-phase SVPWM was developed [12]. In addition,

a novel implementation method of that scheme was patented [7]. Several other 9-phase switching schemes, resulting in lower switching losses, also were developed.

2. Detailed analysis of the stator windings and the resulting magnetomotive force for 9-phase and 3-phase operation was conducted. Based on this analysis the motor parameters were derived. As a result of this work, a method was developed and patented for improvement in torque "smoothness" from a conventional induction machine [10].

3. A unique coordinate transformation from a 9-phase symmetrical system to an orthogonal system was developed. The inverse transformation also was developed based on the constraints which minimized core and winding losses [8].

4. A model of the pole-changing motor was developed directly from fundamental electromagnetics. This model was used to simulate the machine during pole-changing and to validate the control scheme.

5. An experimental setup was prepared. Hardware and software specifically developed for this work included:

   (a) RTLinux real-time motor control development system;

   (b) FPGA/AD 9-phase Motor Controller Interface card; and

   (c) Dynamometer Graphical User Interface.

6. A novel pole-changing control scheme, based on independently controlling two motors sharing the same stator windings, was developed [11].

7. A proposed method for implementing the novel pole-changing control scheme in a drive system for vehicle propulsion was presented.

8.2 Future Work

The work presented can be continued in several possible ways:

1. Implementation of the pole-changing drive:

   (a) The pole-changing drive can be implemented in a vehicle in order to evaluate responsiveness.

   (b) The drive can be evaluated for efficiency improvements, in applications currently using a conventional motor with field weakening.

2. Evaluating the possibility of different pole ratios should be undertaken. Additional work has shown it may be possible to construct a machine with three pole configurations.

3. Using FEA, a more efficient machine can be designed. Due to space constraints the starter/alternator was wound toroidally. Machine efficiency may be improved with different winding patterns.

BIBLIOGRAPHY

[1] R. Bojoi, M. Lazzari, F. Profumo, and A. Tenconi. Digital Field-Oriented Control for Dual Three-Phase Induction Motor Drives. *IEEE Transactions on Industry Applications*, 39(3):752–760, May-June 2003.

[2] D.W. Chung, J.S. King, and S.K. Sul. Unified Voltage Modulation Technique for Real-Time Three-Phase Power Conversion. *IEEE Transactions on Industry Applications*, 34(2):374–380, March/April 1997.

[3] D. Divakaran. RTLinux HOWTO. *http://tldp.org/HOWTO/RTLinux-HOWTO.html*, 2002.

[4] C. Dougan and M. Sherer. RTLinux POSIX API for IO Real-time FIFOs and Shared Memory. *http://www/fsmlabs.com*.

[5] K. Ehlers, H. Hartmann, and E. Meissner. 42V An indication for Changing Requirements on the Vehicle Electrical System. *Journal of Power Sources*, 95(1-2):43–57, March 2001.

[6] J. Holtz, P. Lammert, and W. Lotzkat. High-Speed Drive System with Ultrasonic MOS-FET PWM Inverter and Single-Chip Microprocessor. *IEEE Transactions on Industry Applications*, 23(6):1010–1015, November/December 1987.

[7] J.W. Kelly, M.W. Degner, and P.T. Momcllovich. Method and Apparatus for Pulse Width Modulation. United States Patent 6424113, July 2002.

[8] J.W. Kelly and E.G. Strangas. Torque Control during Pole-Changing Transition of a 3:1 Pole Induction Machine. *International Conference on Electrical Machines and Systems 2007, Korea*, October 2007.

[9] J.W. Kelly, E.G. Strangas, and J.M. Miller. Multi-Phase Space Vector Pulse Width Modulation. *International Electrical Machine and Drives Conference, IEMDC 2001.*, pages 147–155, June 2001.

[10] J.W. Kelly, E.G Strangas, and J.M. Miller. System to Improve the Torque Smoothness of an Electric Machine. United States Patent 6411005, Febuary 2002.

[11] J.W. Kelly, E.G. Strangas, and J.M. Miller. Control of a Continuously Operated Pole-Changing Induction Machine. *IEEE International Electric Machines and Drives Conference*, 1:211–217, June 2003.

[12] J.W. Kelly, E.G. Strangas, and J.M. Miller. Multi-Phase Space Vector Pulse Width Modulation. *IEEE Transactions on Energy Conversion*, 18(2):259–264, June 2003.

[13] P.C Krause, O. Wasynczuk, and S.D. Sudhoff. *Analysis of Electric Machinary*. McGraw-Hill Book, 1986.

[14] W. Leonhard. *Control of Electrical Drives, 3rd Edition*. Springer, 2001.

[15] J.M. Miller and V. Ostovic. Ford PNGV Toroidal Induction/Alternator. United States Patent 5977679, November 1999.

[16] J.M. Miller, V.R. Stefanovic, V. Ostovic, and J.W. Kelly. Design Considerations for an Automotive Integratedstarter-Generator with Pole-Phase Modulation. *Industry Applications Conference, Thirty-Sixth IAS Annual Meeting*, 4(30):2366 – 2373, September/October 2001.

[17] M.Kazmierkowski, R.Krishnan, and F. Blaabjerg. *Control in Power Electronics*. Academic Press, 2002.

[18] M. Osama and T.A. Lipo. Modeling and Analysis of a Wide-Speed-Range Induction Motor Drive Based on Electronic Pole Changing. *IEEE Transactions on Industry Applications*, 33(5):1177–1184, September/October 1997.

[19] R.H. Parks. Two-Reaction Theory of Synchronous Machines - Generalized Method of Analysis-part I. *AIEE*, 48:716–727, 1929.

[20] S.C. Peak and A.B. Plunkett. Transistorized PWM Inverter-Induction Motor Drive System. *NASA STI/Recon Technical Report A*, 83:11488–+, Oct 1982.

[21] G.H. Rawcliffe and B.V. Jayawant. Development of a New 3:1 Pole-Changing Motor. *Proc. IEEE*, 103(a):306, 1956.

[22] M.G Say. *Alternating Current Machines*. Halsted Pr; 5 Sub edition, February 1984.

[23] V.R. Stefanovic and J.M. Miller. Toridally Wound Indcution Motor-Generator with Selectable Number of Poles and Vector Control. United States Patent 20020093200, July 2002.

[24] V.R. Stefanovic and J.M. Miller. Induction Generator Control with Minimal Sensor Requirements. United States Patent 6707279, April 2004.

[25] P. Vas. *Sensorless Vector and Direct Torque Control*. Oxford Science Publications, 1998.